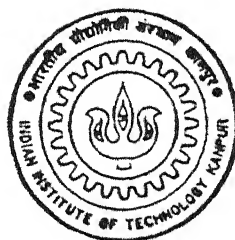


TWO-MAGNON RAMAN SCATTERING STUDIES IN ANTIFERROMAGNETS

by
SAURABH BASU



TH
PHY/1998/P
B299t

DEPARTMENT OF PHYSICS

Indian Institute of Technology, Kanpur

SEPTEMBER, 1998

TWO-MAGNON RAMAN SCATTERING STUDIES IN ANTIFERROMAGNETS

A Thesis Submitted

in Partial Fulfillment of the Requirements

for the Degree of

Doctor of Philosophy

by N.

SAURABH BASU

to the

DEPARTMENT OF PHYSICS

INDIAN INSTITUTE OF TECHNOLOGY KANPUR

SEPTEMBER, 1998

128588



A128588

CERTIFICATE

22/1/84

It is certified that the work contained in this thesis entitled “Two-magnon Raman Scattering studies in Antiferromagnets”, by Saurabh^N_A Basu, has been carried out under my supervision and that this work has not been submitted elsewhere for any degree.



Dr. Avinash Singh
Associate Professor
Department of Physics
Indian Institute of Technology
Kanpur

September 1997

To my Parents

Whose Love and Caring

has made this Mission Possible

SYNOPSIS

During recent times effort has been made to understand the pairing mechanism in high- T_c superconductors. Some theorists believe that an effective electron-electron attractive interaction mediated by spin fluctuation is the possible source of pairing mechanism[1]. Two-magnon Raman scattering is a very useful tool to probe the low-energy excitations in magnetic solids and hence can provide information regarding the nature of pairing correlations.

In the sixties extensive studies have been carried out to understand inelastic light scattering phenomenon in antiferromagnets such as RbMnF_3 , MnF_2 , K_2NiF_4 etc.[2,3] and a good theoretical understanding exists for these systems with spin $S \geq 1$, within the interacting magnon theory for the Quantum Heisenberg antiferromagnets (QHAF). Even though the two-magnon Raman scattering has been studied extensively within the QHAF, there have been so far only limited attempts to systematically study this within the Hubbard model. In spite of the recent success by Shastry and Shraiman[4] in obtaining the Fleury-Loudon (FL) Hamiltonian by performing a strong coupling expansion in powers of t/U , t and U being the hopping term and the on-site Coulomb potential, so far no systematic expansion (a formally weak coupling one) has been carried out which can continuously interpolate between the small- U and large- U limits.

Recently the study of two-magnon Raman scattering gained interest since the experiments performed on La_2CuO_4 [5] (a spin- $\frac{1}{2}$ Heisenberg antiferromagnetic system in two dimensions) reveal a two-magnon Raman scattering linewidth much too broad to be explained within the classical theory. Moreover scattering intensities are observed in geometries, which in the classical approximation, should yield no scattering. The third issue, which seemed puzzling was that the two-magnon spectral weight persists all the way upto $6J$ whereas one would expect the spectrum should have a cut-off at $4J$ because this is the maximum possible

energy that the non-interacting magnons can have.

Some of the discrepancies between the theory and the experiments mentioned above have been clarified to a certain extent by Singh *et al.*[5] by incorporating quantum spin fluctuation which is inherent to low-spin ($S = 1/2$) and low-dimensional ($2D$) systems. Recently it was emphasized by Nori *et al.*[6] that it is necessary to invoke additional processes where they took into account magnon-phonon interaction which can contribute to both the two-magnon Raman linewidth and the finite intensity in the classically forbidden channel. They supported their arguments by computing the Raman cross-section using a $S = 1/2$ Heisenberg model with random static exchange integrals on finite size lattices using Exact Diagonalization (ED) and Quantum Monte Carlo (QMC) techniques. We have pointed out that these calculations do not sufficiently explain the explicit effects of the disorder upon the high energy magnon modes with energy $\sim 2J$ which are mainly responsible for the Raman scattering.

Very recently Chubukov *et al.*[7] have studied extensively the two-magnon scattering process in the resonant regime where the incident photon frequency is of the same order as the band gap in cuprates (both are ~ 3 eV). They found a strong divergence of the Raman vertex close to resonance which was useful in explaining the experiments done on $\text{Sr}_2\text{CuO}_2\text{Cl}_2$ and $\text{YBa}_2\text{Cu}_3\text{O}_{6+x}$ [8].

Apart from the exchange disorder which presumably is arising out of zero-point lattice fluctuations, there are many other correlated electron systems which are intrinsically disordered. The interplay of disorder and spin-fluctuation effects in disordered antiferromagnets have been of intense interest in recent times[9]. In view of that we carry out a comprehensive study on two-magnon Raman scattering in disordered antiferromagnets which yields a detailed information about the spin fluctuation spectrum in presence of on-site disorder.

In **chapter 1** we introduce the topic and provide the necessary background. It contains an overview of the theoretical and experimental status of the field.

In Chapter 2 we develop a systematic diagrammatic scheme to study two-magnon Raman scattering in the Hubbard model. There the fermionic structure of the magnon interaction vertex is studied at order $1/\mathcal{N}$ where \mathcal{N} denotes the orbital degeneracy. The full two-magnon propagator is then evaluated by including the interaction between the magnons at the ladder sum level. The scattering intensity is then obtained from the imaginary part of the propagator. Finally the calculations are extended to the intermediate coupling regime in order to make connections with the experiments done on cuprate insulators. An attempt has been made to incorporate zero temperature magnon damping which yields a better agreement with the experiments performed on La_2CuO_4 .

In Chapter 3 we study the effect of hopping disorder in a Hubbard Antiferromagnet using both perturbation theory and exact eigenstate method. Here the lattice distortions arising out of quantum and thermal fluctuations are considered within adiabatic approximation (or Born-Oppenheimer approximation) which neglects the fluctuation of the phonon field. It is shown that while the low-energy long wavelength modes are only weakly affected, the high energy modes are strongly renormalised because of a cooperative effect arising from local correlations in hopping disorder. We also discuss the implication of this highly asymmetric magnon energy renormalization for two-magnon Raman scattering in cuprate antiferromagnets.

Chapter 4 deals with obtaining the Raman scattering intensity numerically in presence of hopping disorder. A consistent scheme of mode assignments is used which essentially establishes a one-to-one correspondence between the pure and disordered system and we believe it to be valid in the weak disorder limit. It is shown that even for a substantially weak disorder, several features like the asymmetry with respect to the two-magnon peak, linewidth to peak position ratio and the spectral weight persisting all the way upto $6J$ agree well with the experimental data.

In Chapter 5 we have calculated the Raman scattering intensity in an antiferromagnet

in presence of random on-site energies. It was found[9] that the magnon modes are damped due to scattering of magnons by disorder. This damping was calculated by considering the vertex corrections and shown to be proportional to the fourth power of the disorder strength. We obtain the magnon damping in a self-consistent manner and use this to calculate the Raman lineshape for various disorder strengths.

In Chapter 6 we develop a real-space formalism to study the two-magnon propagator which allows the calculation of the Raman intensity for disordered systems involving hopping disorder, potential disorder, impurities, vacancies etc.

Bibliography

- [1] D.J. Scalapino, Phys. Rep. **250**, 329 (1995)
- [2] P.A. Fleury and R. Loudon, Phys. Rev., **166**, 514, (1968)
- [3] J.B. Parkinson, J. Phys. C (Solid State Phys.), **2**, 2003 (1969)
- [4] B.S. Shastry and B.I. Shraiman, Phys. Rev. Lett., **65**, 1068 (1990), Int. J. Mod. Phys. B, **5** (1991)
- [5] R.R.P. Singh, P.A. Fleury, K.B. Lyons and P.E. Sulewski, Phys. Rev. Lett. **62**, 2736 (1989)
- [6] F. Nori, R. Merlin, S. Haas, A.W. Sandvik and E. Dagotto, Phys. Rev. Lett., **75**, 553 (1995)
- [7] A.V. Chubukov and D.M. Frenkel, Phys. Rev. B **52**, 9760 (1995), D.K. Morr and A.V. Chubukov, Report number cond-mat/9705051
- [8] G. Blumberg, P. Abbamonte and M.V. Klein, SPIE proceedings **2696**, 205 (1996)
- [9] A. Singh, M. Ulmke and D. Vollhardt, Report number cond-mat/9803094

Acknowledgment

Five years and two months. That was how long back I started my PhD. This period has flashed by in a wink - it was such a short period. The period was small but my experiences and my associations were big. Pleasant, but sometimes unpleasant, exhilarating, but sometimes depressing, joyful, but sometimes sad – experiences of all hues. But as I sit and write, right now, I remember only the pleasant and the exhilarating and the joyful experiences and the many people linked with it.

First, I take the opportunity to express gratitude to my *Guru* Dr. Avinash Singh. He not only introduced me to the subject, but also guided me thru' the entire journey dextrously. In particular, his way of thinking has impressed and motivated me a lot. I also thank Drs. Vijay Singh and Satyendra Kumar for helping me out as the evaluation committee members and V. Subhramanyam for acting as my program coordinator for one year. A very special mention goes to Drs. A.K. Mazumdar, Abhijit Mookerjee and Pankaj Jain for enlightening me occasionally with some lively academic discussions. Dr. Mahendra Verma and Dr. Pankaj Jain did a great job in setting up the departmental computational facilities which has proved to be of tremendous benefit especially during the time of writing the thesis. Interesting discussions with Dr. Gautam Sengupta in the computer lab. at the wee hours of the night has certainly made it easier to work. The discussions with the Condensed Matter experimental group were often quite fruitful - Dr. R.C. Budhani, Dr. C.V. Tomy and Dr. A.K. Mazumdar were always enthusiastic to discuss the issues which I approached them with. A mention of thanks is also due to Dr. A.K. Mazumdar and Dr. R.K. Thareja, the two HOD's during my stay here.

Tea-sessions clubbed with interesting discussions with Dr. Y.R. Waghmare were always enjoyable. The name of the person responsible for all these cups of tea should not go unmentioned - it was Brij Lal. The office staff, especially Panda-ji and Srivastava-ji were very cooperative.

The graduate seminar which was held quite regularly thru'out my stay had a good amount of impact upon me. I felt that it promotes a lively and informal interaction between the students. Being a part of 'Physics Society' and organizing its various activities was fun. The excursions, the welcome and the farewell functions , the cricket matches all provided good entertainment.

I guess thanking the friends is a daunting task since they form an integral part of both the academic, not-so-academic and non-academic life in the IIT. A few names to mention are Prashanta, Alok, Vivek, Bijoy, Jim, Aalok, Gautam, Prasenjit, Rajan and Sudhanshu. But one name that really stands out from the crowd is my *soul-mate* Gaurav. He has made tremendous impact upon me in every aspect of life. He helped me to regain and retain composure during the most difficult time of my Ph.D. I learnt from him a good deal of almost everything that I know -- that includes Hindi, GK, Trekking, Mountaneering, Basketball and of course Physics. His constant encouragement is one gift I want to cherish for life.

Finally, I thank my family for supporting me all these years and motivating me to become what I am today. My parents' blessings have provided foundations upon which I can progress. I also thank my wife, Sanghamitra for being a source of both encouragement and distraction at the same time. The phone-conversations with her often worked as a panacea for all the problems plaguing my PhD at various times.

List Of Publications

- *Gap states, local moments and magnetic dynamics in a Mott- Hubbard Antiferromagnet doped with static impurities*, Phys. Rev. B **50**, 10381(1994) with P.Sen and A.Singh
- *Gap states in a doped Mott Hubbard insulator* , Pramana journal of physics. **44**, L77(1995) with P.Sen and A.Singh
- *Self consistent study of the impurity doped Mott-Hubbard insulator*, Phys. Rev. B **53**, 6406 (1996), with A.Singh
- *Two Magnon Raman scattering in a Mott-Hubbard Antiferromagnet*, Phys. Rev. B **54**, 6356 (1996). with A.Singh
- *Hopping disorder. magnon energy renormalization and two-magnon Raman scattering in an Antiferromagnet*, (Phys. Rev. B, 12338 1997), with A.Singh
- *Hopping-disorder-induced effects upon two-magnon Raman scattering in an Antiferromagnet*, Cond-Mat/9809251.

Contents

Synopsis	i
Acknowledgments	vi
List of Publications	viii
List of Symbols	3
1 Introduction	5
1.1 General Discussion	5
1.2 Two-magnon Raman Scattering from Pure Antiferromagnets	5
1.3 Two-magnon Raman Scattering from Impurity Doped Antiferromagnets . . .	9
1.3.1 Non-magnetic impurity	9
1.3.2 Magnetic Impurity	10
1.4 Experiments done on Copper-Oxide based materials	12
1.5 Recent Theoretical Developments	18
1.6 Brief Outline of the Thesis	29
2 Two-Magnon Raman Scattering for a Pure Antiferromagnet	35
2.1 Introduction	35
2.2 Two-magnon Propagator in the large- U limit	37
2.3 Extension of the calculation to Intermediate- U regime	48
2.4 Zero-temperature magnon damping	50

3	Hopping Disorder and Asymmetric Magnon-Energy Renormalization in an Antiferromagnet	60
3.1	Introduction	60
3.2	Perturbative Analysis	63
3.3	Numerical analysis	69
4	Hopping-disorder-induced effects upon Raman Scattering spectrum in an Antiferromagnet	76
4.1	Introduction	76
4.2	Configuration averaging of the two-magnon propagator	78
4.3	Mode Assignments	83
4.4	Calculation of the two-magnon Raman intensity	86
5	Raman spectra in presence On-Site Disorder in Antiferromagnets	98
5.1	Introduction	98
5.2	On-site disorder	99
5.3	Magnon Damping	103
6	The Real-Space Formalism	110
6.1	Introduction	110
6.2	The two-magnon propagator in Real Space	111
6.3	Numerical approach	115

List of Figures

1.1	Two-magnon Raman lineshape for Rb_2MnF_4 without magnon-magnon interaction (curve A) and with magnon-magnon interaction (curve B). (From Ref. [13])	7
1.2	Two-magnon Raman spectra for La_2CuO_4 in the (a) B_{1g} and (b) A_{1g} and B_{2g} scattering geometry. In (a) the peak frequency $\omega_p (= 3170\text{cm}^{-1})$, is found to be slightly smaller than the first moment or the 'central frequency' ρ_1 . The second cumulant M_2 measures the width of the peak. In (b) σ, σ' are unit vectors connecting to the nearest neighbour (NN) and diagonal nearest neighbour (NNN) in a lattice. (From Ref. [34])	15
1.3	Two-magnon Raman scattering intensity shown for $\text{YBa}_2\text{Cu}_3\text{O}_6$ as a function of transferred photon frequency. (From Ref. [44])	16
1.4	Two-magnon Raman spectra of $\text{YBa}_2\text{Cu}_3\text{O}_{6+x}$ for three values of x : (a) 0.0; (b) ~ 0.7 ; (c) ~ 0.9 . Incident wavelength is 4880\AA . (From Ref. [37])	17
1.5	Diagrammatic representation of the Direct (top) and exchange (below) terms appearing in the resonant Matrix element $M_R^{\alpha\beta}$ (see the discussion in the text)	21
1.6	Commonly used scattering geometries.	22

1.7	Diagrams which are important for the resonant processes. All the three denominators in the diagram (a) can vanish simultaneously, which is known as 'Triple Resonance'. Additional relevant diagram (which is less dominant than (a)) is shown in (b). Here the fermions belonging to a valence (conduction) band is represented by a dashed (solid) line. The emitted magnons are denoted by the solid wavy lines whereas the dashed wavy lines are the incoming and outgoing photons. (From Ref. [44])	24
1.8	Normalized Raman cross-section $I(\omega)/I_{max}$ is shown as a function of scattered photon frequency ω (in units of J). The plot in solid line shown in (a) corresponds to the spectra obtained by Exact Diagonalization with $N = 16$ and the dashed one is obtained from Quantum Monte Carlo studies for $N = 144$ for $\sigma = 0.0$ in the B_{1g} symmetry. The plots shown in (b) and (c) corresponds to the scattering intensity in B_{1g} and A_{1g} symmetry corresponding to $\sigma = 0.3J, 0.4J, 0.5J$. (From Ref. [54])	26
1.9	B_{1g} Raman spectrum for $J = 1$ in a 4×4 lattice, obtained from Exact Diagonalization studies. (a) Pure Heisenberg model; (b) static vacancy in the Heisenberg, (c) dynamical hole in the $t - J_z$; (d) dynamical hole in $t - J$ model. (From Ref. [57])	28
2.1	Fermionic structure of the diagrams contributing to the magnon interaction vertex at the order $1/N$ level and in the strong coupling limit. The interacting magnons are on A and B sublattice sites. The interaction vertices lie within the four wavy lines representing the Hubbard interaction. The hatched areas represent magnon propagators.	45
2.2	Calculated two-magnon Raman scattering intensity in the B_{1g} symmetry in the large- U limit (dashed) and intermediate- U limit (solid).	50
2.3	Calculated two-magnon Raman scattering intensity in the B_{1g} symmetry with a magnon damping of $\Gamma/J = 0.15$, and few points from the observed Raman scattering in La_2CuO_4 [taken from ref. 8].	52

3.1	Diagrams contributing at the (a) first-order level in δt (dashed lines) and (b) second-order level to the diagonal matrix element $[\delta\chi^0]_{ii}$ and the nearest-neighbor matrix element $[\delta\chi^0]_{ij}$	64
3.2	The amplitude for the highest magnon-mode (below) and the magnetization profile (top) obtained from numerically is shown for a 10×10 lattice for $U/t = 10$ in presence of disorder ($\sigma = 0.1$).	67
3.3	The configuration-averaged magnon density of states obtained numerically for a 10×10 hopping disordered system with $\sigma = 0.1$ and 0.3 , in the strong-correlation limit ($U/t = 10$).	68
4.1	Interaction between two magnons is shown where the bold lines represent the two magnons propagating from neighbouring sites \mathbf{r} and $\mathbf{r} + \delta$ to \mathbf{r}' and $\mathbf{r}' + \delta'$. The wavy lines denotes the interaction between the magnons at sites \mathbf{r}_1 and $\mathbf{r}_1 + \mu$ where μ connects to the nearest neighbouring sites. The creation and destruction of magnons at these points are shown by S^+ and S^- where the subscripts B_{1g} and A_{1g} correspond to different scattering geometries defined in the text.	79
4.2	The region in the Brillouin Zone (BZ) is shown where the dots denote the mode numbers n_x and n_y chosen so as to assign labels to the mode energies calculated. A few of the mode numbers are indicated. The first two quadrants are required for assigning numbers to all the modes.	84
4.3	The two-magnon scattering intensity is plotted as a function of transferred photon frequency ω (in units of J) for the hopping disordered case with a gaussian disorder of width $\sigma = 0.1$	88
4.4	The two-magnon Raman lineshape is shown for more moderate values of disorder, viz. $\sigma = 0.01$ and 0.03 . The pure case ($\sigma = 0.0$) is included for comparison	90

4.5	The two-magnon Raman lineshape is shown for the strong coupling case ($U/t = 100$) in order to compare with the results of Reference [1]. The values taken for disorder are $\sigma = 0.01, 0.03$ and 0.1	91
4.6	The spin raising and lowering operators are shown for the $G_0(\Omega)$	93
5.1	The first (a - d) and second order (e - l) diagrams shown for calculating zeroth-order particle-hole propagator $[\chi_0]$	101
5.2	The magnon damping (in units of t) is shown as a function of q_x and q_y . It can be seen that the damping is maximum for $(q_x, q_y) \sim (\pi, \pi)$ which corresponds to magnon energy close to upper band edge ($=2J$).	107
5.3	The Raman lineshape is shown $\sigma = 0.01$ and 0.03 . The pure case ($\sigma = 0.0$) is also included for comparison.	107

List of Tables

2.1	Contributions to the magnon interaction vertex of diagrams shown in Fig. 2.1 (a)-(h), for various signs of the pair of fermion propagators which are off-diagonal in sublattice basis. The fermion-propagator signs refer to the advanced/retarded nature of the fermionic propagators.	46
3.1	Variation of the configuration-averaged maximum magnon energy $\overline{\omega_m}$ with hopping disorder strength σ . Also shown are the configuration-averaged increase in magnon energy $\overline{\omega_m} - \omega_m^0$ for the highest magnon mode relative to the pure-case energy ω_m^0 , and comparison with the configuration-averaged maximum self-energy correction $\overline{\Sigma_m}$ evaluated from Eq. (3.9).	71
4.1	The mode energies are obtained using the expression relevant to the intermediate- U regime ($U/t = 10$ or $\Delta/t = 5$) for a 10×10 system where $n_{x/y} = (\frac{L}{2\pi})q_{x/y}$ are the mode numbers specified in the leftmost column. Also we have shown the energies calculated numerically using the exact eigenstate method for comparison. The symmetry factors for both B_{1g} and A_{1g} scattering geometries are obtained using the mode numbers.	85
4.2	Here the assignment of the mode numbers n_x and n_y is shown for the mode energies calculated numerically for both pure and disordered systems ($\sigma = 0.1$) of system size 10×10 and for $U/t = 10$	86

4.3 Experimental values for the peak frequency, first, second and third moments of the B_{1g} scattering profile in La_2CuO_4 corresponding to the laser excitation wavelength of 4880 \AA . The experimental lineshape is shown in Fig. (1.2). Also the values calculated using equations (4.27) and (4.28) are given. 96

List of Symbols

U, t, Δ	: Coulomb term, hopping integral and gap parameter in the Hubbard model.
$[\chi^{-+}]$: Particle-Hole Propagator at the RPA level
$[\chi^0]$: Zeroth-order Particle-Hole Propagator
$[\delta\chi^0]$: Disorder-induced correction to the Zeroth-order Particle-Hole Propagator
V_{int}	: Interaction between the magnons.
ω_q	: Spin-wave energy for the mode q .
Ω_Q	: Spin-wave energy for the mode Q . : (Only used in Chapter 2)
$[G^0(\omega)]$: Zeroth-order Two-Magnon Propagator.
$[G^0(\Omega)]$: Zeroth-order Two-Magnon Propagator (Only used in Chapter 2).
$[G(\omega)]$: Full Two-Magnon Propagator.
$[G(\Omega)]$: Full Two-Magnon Propagator (Only used in Chapter 2).
$\hat{\delta}$: units vector connecting in $\pm\hat{x}/\pm\hat{y}$ direction.
$I(\omega)$: Two-Magnon Raman intensity as a function of ω . : (in arbitrary units)
$I(\Omega)$: Two-Magnon Raman intensity as a function of Ω . : (in arbitrary units) (Only used in Chapter 2)
ϕ_q	: Symmetry factor.
ϕ_Q	: Symmetry factor (Only used in Chapter 2).
\mathbf{S}	: Spin vector.
$S^{-/+}$: Spin Raising/Lowering operator.

$N(\omega)$: Magnon Density of States (DOS) as a function : of ω (in arbitrary units).
$N(\Omega)$: Magnon Density of States (DOS) as a function : of Ω (in arbitrary units) (Only used in Chapter 2) .
$E_{inc/sc}$: Incident/Scattered Electric Field vector : of the Photon.
ω_i, ω_f	: Incident and scattered photon frequencies.
σ	: Width of the Gaussian distribution for the hopping disorder.
W	: Width of the Rectangular distribution for the on-site disorder.
J	: Exchange term in the Heisenberg model.
J_z	: In-plane exchange term (also denoted by $J_{ }$
J_{\perp}	: Inter-planar exchange term (also denoted by J_{\perp} .
Γ	: Magnon damping.
Σ	: Magnon self-energy.
$\lambda_n, \phi_n(\mathbf{r})$: n -th (from the top) eigenvalue and eigenvector of the $[\chi^0]$ matrix.
D	: Dimensionality.
B	: Bandwidth.
L	: System size.

Chapter 1

Introduction

1.1 General Discussion

Experimental observation of the inelastic light scattering in liquids and solids has a long history dated since 1928 due to Raman[1, 2] which won him the Nobel prize in Physics. He observed that when the incident light of frequency ω_i interacts with the system, then the scattered light has a frequency ω_s , which is either greater (Stoke's Scattering) or lesser (anti-Stoke's scattering) than ω_i . Also there can be a possibility where the incident light suffers no frequency shift due to scattering and is called Rayleigh scattering. Brillouin[3] and Mandelstam[4] predicted similar scattering effects from sound waves in dense media. The term 'Raman scattering' is now used to describe light scattering from various kinds of excitation like phonons, magnons etc. In my thesis, I have concentrated only upon light scattering from magnons or spin waves which are the lowest-lying collective excitations that occur in magnetically ordered material.

1.2 Two-magnon Raman Scattering from Pure Antiferromagnets

It was shown by Elliot and Loudon[5] that the mechanism responsible for light scattering from magnons is the electric dipole interaction. The magnons in the magnetic material create a spatially periodic modulation of the permittivity and the light gets scattered by the fluctuation

in permittivity. The first observation of Raman scattering from magnons was carried out by Fleury[6] where he studied the temperature-dependent light-scattering spectra from one and two-magnon excitations in antiferromagnetic FeF_2 . Since the incident photon has essentially zero wavevector, one-magnon scattering arises from magnons with wavevector near the center of the Brillouin zone (BZ), while for two-magnon excitation, the magnons have equal and opposite momenta. Soon many experiments followed to observe Raman scattering from magnons in other antiferromagnets like MnF_2 [7], RbMnF_3 [8] and NiF_2 [9]. An apparently surprising result emerged from these experiments which is the two-magnon cross-section is usually larger than the one-magnon cross section. This can be trivially explained by noting that the scattering cross-section is proportional to the magnon density of states (DOS) and the DOS is very small for magnons with wavevector close to the center of the BZ. I will be mostly interested in looking at the two-magnon scattering phenomenon in antiferromagnets.

Elliot and Thorpe[11] have shown that in an antiferromagnet the spectrum of the scattered light as a function of energy transfer from the photon to two magnons is very sensitive to the interaction between the two magnons. The reason is that the two magnons are created at two neighbouring sites and hence the interaction is rather important (Fig. (1.1)). The necessity of invoking the magnon-magnon interaction to explain the complete lineshape was experimentally confirmed by Fleury[8] on RbMnF_3 , Thorpe[12] on MnF_2 , Parkinson[13] and Fleury *et al.*[14] on two dimensional antiferromagnets such as K_2NiF_4 . The essential feature of the scattering spectrum borne out of experiments is that the two-magnon peak occurs at a transferred photon frequency of $J(2SZ - 1)$, whereas the joint magnon DOS peaks at $2JSZ$. It indicates that the presence of the first spin deviation leads to a reduction in energy for the second spin deviation.

At zero temperature, the two-magnon Raman cross-section was derived by Elliot and Thorpe[11] using a Green's function theory. They employed a refined decoupling procedure to linearize the Green's function equations in a controlled manner. It is appropriate here to

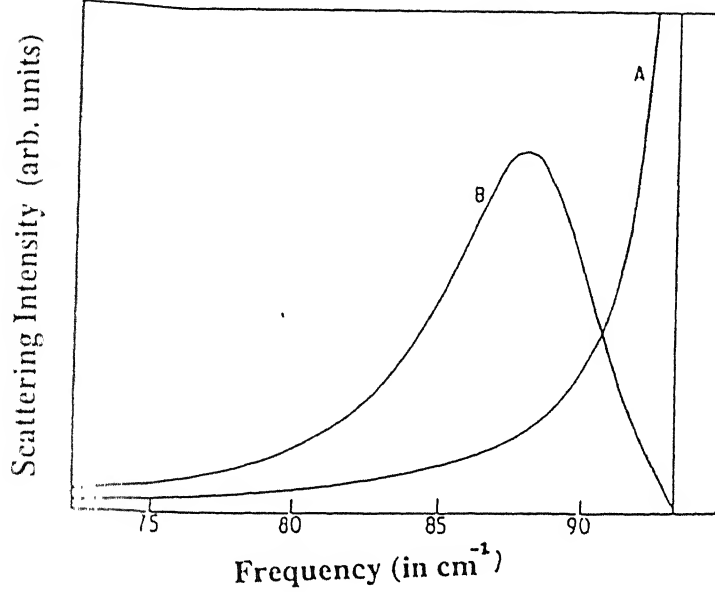


Figure 1.1: Two-magnon Raman lineshape for Rb_2MnF_4 without magnon-magnon interaction (curve A) and with magnon-magnon interaction (curve B). (From Ref. [13])

briefly describe the theory due to Elliot and Thorpe[15].

To calculate the two-magnon Raman spectrum one needs to calculate the imaginary part of the two-magnon propagator given by,

$$G(\hat{\delta}, \hat{\delta}') = \langle P_{\hat{\delta}}^T P_{\hat{\delta}'}^T \rangle$$

Where $P_{\hat{\delta}}^T$ is the transverse spin-pair operator given by,

$$P_{\hat{\delta}}^T = \frac{1}{2} \sum_{\mathbf{r}} (S_{\mathbf{r}}^+ S_{\mathbf{r}+\hat{\delta}}^- S_{\mathbf{r}}^- S_{\mathbf{r}+\hat{\delta}}^+)$$

and $\hat{\delta}, \hat{\delta}'$ are unit vectors connecting nearest neighbours. When one writes down the equation of motion for $\langle P_{\hat{\delta}}^T, P_{\hat{\delta}'}^T \rangle$ following Zubarev[16], it turns out that one has to evaluate the commutator $[P_{\hat{\delta}}^T, H_R]$ where H_R is the light scattering Hamiltonian given by Fleury and Loudon[17],

$$H_R = A \sum_r (\mathbf{E}_{\text{inc}} \cdot \hat{\delta})(\mathbf{E}_{\text{sc}} \cdot \hat{\delta}) \mathbf{S}_r \cdot \mathbf{S}_{r+\hat{\delta}} \quad (1.1)$$

where \mathbf{E}_{inc} and \mathbf{E}_{sc} are the incident and scattered Electric field vectors of the photon. The commutator leads to terms like $S_{\mathbf{r}_1}^z S_{\mathbf{r}_2}^+ S_{\mathbf{r}_3}^-$ where either all of the site indices \mathbf{r}_1 , \mathbf{r}_2 and \mathbf{r}_3 either correspond to different sites or at most two sites are same. The above product of spin operators must be decoupled in order to obtain a set of linear equations that may be solved to yield $\langle P_{\hat{\delta}}^T P_{\hat{\delta}'}^T \rangle$. A simple minded decoupling is to replace $S_{\mathbf{r}_1}^z$ by $\pm S$ depending upon the sublattice. But this yields the non-interacting spin-wave result which has got very poor agreement with experiments. The deficit was taken care of by introducing an improved decoupling procedure. If \mathbf{r}_1 , \mathbf{r}_2 and \mathbf{r}_3 are all different then replace $S_{\mathbf{r}_1}^z$ by $\pm S$ appropriate to the sublattice, while if $\mathbf{r}_1 = \mathbf{r}_2$ then replace

$$S_{\mathbf{r}_1}^z S_{\mathbf{r}_1}^+ \rightarrow S S_{\mathbf{r}_1}^+$$

and,

$$S_{\mathbf{r}_1}^+ S_{\mathbf{r}_1}^z \rightarrow (S - 1) S_{\mathbf{r}_1}^+$$

for spins in the \uparrow -spin sublattice. Similar replacement for spins on the \downarrow -spin sublattice (by changing S to $-S$) and also for the case $\mathbf{r}_1 = \mathbf{r}_3$. This decoupling straightforwardly yields the two-magnon cross-section to be proportional to,

$$\text{Im} \left[\frac{G_0}{1 + JG_0} \right]$$

where J is the self-energy arising from the magnon-magnon interaction and G_0 is the non-interacting two-magnon propagator given by,

$$G_0(\Omega) = \frac{1}{N} \sum_q \frac{\phi_q^2}{(\Omega^2 - 4\Omega_q^2)}$$

where ϕ_q is the symmetry factor appropriate to the lattice and Ω_q is the spin-wave energy obtained at the RPA level given by $\Omega_q = ZJS\sqrt{1 - \gamma_q^2}$ and $\gamma_q = \frac{1}{Z} \sum_{\delta} e^{iq \cdot \delta}$ where Z is the number of neighbours. The spectrum thus obtained has got excellent agreement with

experiments. A generalization of the calculation to finite temperature was done by Sólyom[4] by taking into account the temperature dependence coming from the Bose factors describing the occupation number of magnons. He finds that the two-magnon peak shifts with increasing temperatures towards low energies and the peak broadens. Also it is observed that the peak does not disappear at the Neél temperature T_N and even continues to persist upto as high as $4T_N$. This can be qualitatively understood by arguing that the short range spin correlation plays an important role in the two-magnon Raman scattering and that does not vanish at T_N . There were other theoretical efforts to extend the theory at finite temperature during the early seventies. These include a diagrammatic scheme using the Dyson-Maleev transformation[19] for $T < T_N$ [20] and the equation-of-motion approach using a modified decoupling procedure for $T > T_N$ [21].

1.3 Two-magnon Raman Scattering from Impurity Doped Antiferromagnets

The introduction of low concentration of substitutional impurity into an antiferromagnetic insulator modifies the spectrum of magnetic excitations. In general, the spectrum consists of a set of impurity modes associated with the defect and it's immediate neighbours. The impurity modes occur outside the band of host excitations and are localized in the neighbourhood of the defect.

1.3.1 Non-magnetic impurity

Raman scattering from pairs of magnons in antiferromagnets in presence of non-magnetic impurities like Mg, Zn etc. were studied experimentally for both low and high impurity concentrations. It was observed that the position of the peak shifts towards lower frequency and the spectrum broadens with increase in impurity concentration. Fleury *et al.*[22] studied Raman scattering in doped antiferromagnets like $\text{KNi}_{1-x}\text{Mg}_x\text{F}_3$ upto a concentration x as high as 0.75. Also experiments were done on Zn doped systems such as $\text{Mn}_{1-x}\text{Zn}_x\text{F}_2$ [23,

24] and it displayed a similar concentration dependence as observed in $\text{KNi}_{1-x}\text{Mg}_x\text{F}_3$. The two-magnon peak was observable upto $x \sim 0.7$ but was very weak. Again the peak frequency decreased linearly with x , but the linearity persisted only upto $x \simeq 0.3$. Some other groups[25] have looked at Raman scattering from mixed crystals like $\text{Fe}_{1-x}\text{Zn}_x\text{F}_2$ where the peak frequency showed a linear fall off with x upto $x \simeq 0.5$ and then it roughly remained constant upto about $x = 0.75$.

1.3.2 Magnetic Impurity

Broadly we can classify the experimental work done on Raman scattering from magnon pairs in antiferromagnets diluted by magnetic impurity into two types. The first is the scattering from point defects i.e. at very low impurity concentration (e.g. $\sim 1\%$). Secondly, at high concentration the scattering involves excitation of magnons in each sublattice A and B giving rise to three kinds of pair excitations, viz. A – A, A – B and B – B.

Scattering from point defect type had been observed in several mixed antiferromagnets viz. Ni doped RbMnF_3 [26, 27], and KMnF_3 [28] and Co in RbMnF_3 [29]. The general observation is that two-magnon peak moves towards higher frequency with increasing impurity concentration. With higher concentration the two-magnon Raman spectrum exhibits three distinct bands. The most detailed experimental account was provided by Lockwood *et al.*[30] where they studied the light scattering from $\text{KNi}_x\text{Mn}_{1-x}\text{F}_3$ for four different impurity concentration such as, $x = 0.84, 0.73, 0.54$ and 0.15 . The spectrum showed clearly two-magnon bands corresponding to the creation of magnons on neighbouring pairs of Ni ions, neighbouring Ni and Mn ions and neighbouring Mn ions. The frequencies at which these bands occurred had got good agreement with theoretical calculations done using Ising Cluster model along with an improvement done which incorporated the modifications in the exchange constants with lattice parameter due to doping. They had also performed a systematic study to look at the temperature dependence of these bands. The bands became broader with increase in temperature and shifted towards lower frequencies. Qualitatively the behaviour remained

the same for all the bands.

Before I close the discussion on light scattering from impure magnets, a very brief discussion of the Ising Cluster model is presented here. It provides a good description of frequency dependence of the scattering process in pure materials essentially because the zone boundary frequency of the magnons in antiferromagnets is given quite precisely by the Ising model. These zone boundary modes dominate the two-magnon scattering process because of their large DOS. Consequently we expect it to provide a substantial information of the two-magnon Raman scattering in these systems.

For high impurity concentration, the Raman intensities of the various bands in the spectra reflect the probability of finding the corresponding neighbour pairs, and are given by the simple Cluster model as,

$$I_{A-A} \propto (1 - x)^2$$

$$I_{A-B} \propto 2x(1 - x)$$

$$I_{B-B} \propto x^2$$

where x represents impurity concentration. The ratios of the intensities thus calculated have a fairly good agreement with the experiments done on $\text{KNi}_x\text{Mn}_{1-x}\text{F}_3$ except for the Mn – Mn band which was found to be much weaker than what is predicted by the Cluster model. This discrepancy arose because of a nearly resonant Raman process for the intermediate states associated with the virtual excitation of Ni ions. This renders a considerable intensity to the Ni – Ni band and even to the Ni – Mn band, since it depends on the overlap of the Ni excited states on neighbouring Mn. It is reasonable to assume that the intensity of the Mn – Mn band will be considerable only if one or both of the Mn – Mn ions are nearest neighbours

to a Ni ion. So, essentially it is roughly proportional to the Mn pairs which have Ni as nearest neighbour. But on increasing the Mn concentration the intensity of the band does not increase, as expected naively, due to a simultaneous decrease of nearest neighbour Ni ions.

The widths of the two-magnon bands are studied in detail by Lockwood *et al.*[30]. Evaluation of the two-magnon scattering intensity involves a summation over states within the BZ and hence there is a finite linewidth in the scattering spectrum even in the pure materials. In presence of impurities there will be two contributions to the width: one arising from the wavevector sum and the other from the width of the intrinsic excitations which presumably arises due to impurity-induced damping in the magnon spectrum.

1.4 Experiments done on Copper-Oxide based materials

Ever since the discovery of high- T_c superconductivity[31], there have been persistent efforts among the theoreticians to understand the mechanism responsible for pairing among the electrons. The widespread belief is that the strong electron correlation in these compounds may contain a clue to that. One of the important consequences of this correlation is that the undoped parent compounds are antiferromagnets. Raman scattering has proved to be a very useful tool to probe the collective magnetic excitations in these compounds. Common to all antiferromagnetic cuprates, the Raman studies reveal a well defined peak which is attributed to inelastic scattering from two-magnon excitations in the B_{1g} scattering geometry along with a weaker but still significant signal in the A_{1g} geometry at a transferred photon frequency close to 3000 cm^{-1} .

These antiferromagnetic compounds are well described by modeling the undoped CuO_2 layer with the Cu ions arranged antiferromagnetically in $3d^9$ configuration with the $3d$ holes carrying a spin $S = \frac{1}{2}$. A more detailed picture yields that the Cu spins are coupled to each other by superexchange via the Oxygen atoms.

In these systems the interaction between the spins may be expressed in terms of the Heisenberg Hamiltonian,

$$H = J \sum_{\langle ij \rangle} \mathbf{S}_i \cdot \mathbf{S}_j \quad (1.2)$$

where \mathbf{S}_i represents the spin vector at the site i and J is the exchange constant. Conventional spin-wave theory yields,

$$\omega_q = ZJS\sqrt{1 - \gamma_q^2}$$

for the spin-wave spectrum where $Z = 4$ (for 2D) and $S = \frac{1}{2}$. Neutron scattering experiments on these systems have confirmed the presence of 2D antiferromagnetic order. But due to energy limitations in the neutron scattering experiments it was not possible to measure the spin-wave dispersion with any degree of accuracy and hence the value of J could not be determined.

So to ascertain the value of J and to probe the spin-dynamics in detail, inelastic light scattering studies were performed in these systems and here I am going to provide a brief review of the experiments done on the insulating and doped phase of the Cuprates. In contrast to neutron scattering, these experiments show striking deviation from classical spin-wave behaviour.

The first experimental observation for the two-magnon Raman spectra came about in 1987[32, 33], when scattering measurements were performed on antiferromagnetic La_2CuO_4 . The lineshape is shown in Fig. (1.2). The symmetry consideration plays a crucial role in interpreting the polarization dependence of Raman scattering. From the spectral lineshape it can be noticed that,

(a) The two-magnon peak occurs at an energy close to $3J$, to be precise at $2.7J$ [34] which is predicted by a naive bond counting argument which goes as follows. The process of excit-

ation of two magnons in a Néel state involves breaking of 6 nearest neighbour bonds which results in an energy cost of $3J$ as opposed to $4J$, if the spins flipped were not neighbour pairs.

(b) The anomalously large linewidth of the profile which is found to be approximately 38% of the frequency at the spectral maximum, whereas the theoretically predicted value is only 11%.

(c) There is an appearance of signal in the A_{1g} and B_{2g} scattering geometries which are forbidden in the Néel ground state.

(d) The scattering intensity persists well beyond $4J$ whereas the joint magnon density of states vanishes at energies higher than $4J$.

(e) From the experiments the value of J was found to be $(1030 \pm 50)cm^{-1}$.

Initially[35] the deviation from the theoretical prediction was suggested to have extrinsic origin, such as impurities or non-magnetic scattering (e.g. from phonons). Almost immediately the problem was looked at by Singh and co-workers[34]. They took into account the effect of quantum spin fluctuation which leads to a substantial enhancement of the linewidth. Also the signals in the classically forbidden scattering geometries e.g. A_{1g} and B_{2g} can be argued to originate from diagonal nearest neighbour (NNN) or next nearest neighbour (NNNN) spin pair excitations which are Raman active solely by virtue of quantum fluctuations. To account for such a NNN term (or NNNN term) in the Raman operator, (see Eq. 1.1) $\hat{\delta}$ has to be changed to $\hat{\delta}'$ where $\hat{\delta}'$ connects to NNN (or NNNN) spins. Such a replacement makes no contribution to the B_{1g} geometry but accounts for the spectra in the A_{1g} and B_{2g} geometries.

Also the temperature dependence of the Raman spectra is investigated[35] and it is observed that the renormalisation of the overall Raman intensity with temperature is quite small compared to that of long wavelength magnons, because of the dominance of short wavelength magnons in the two-magnon scattering process. Typically the spectral weight

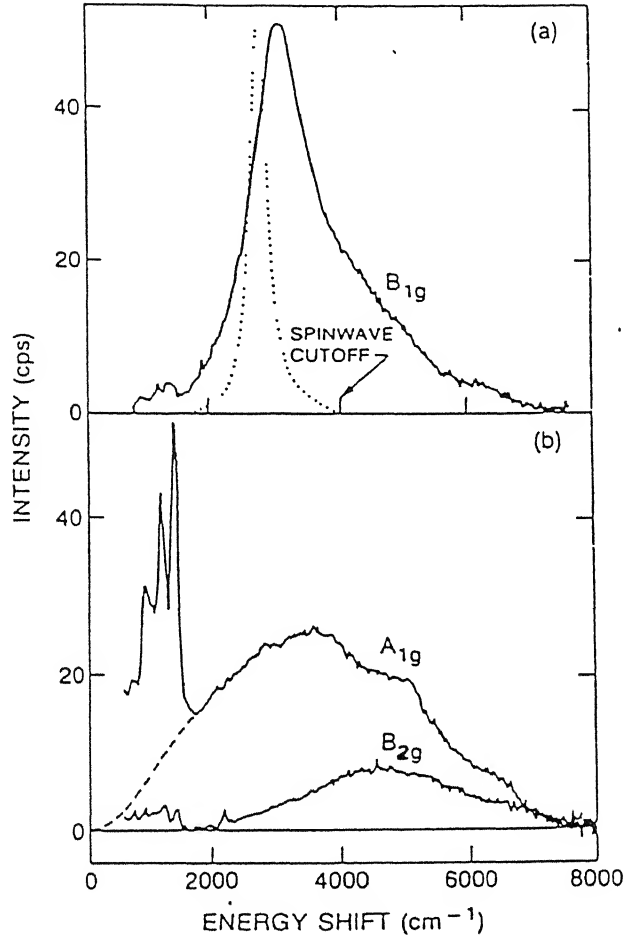


Figure 1.2: Two-magnon Raman spectra for La_2CuO_4 in the (a) B_{1g} and (b) A_{1g} and B_{2g} scattering geometry. In (a) the peak frequency $\omega_p (= 3170 \text{ cm}^{-1})$, is found to be slightly smaller than the first moment or the 'central frequency' ρ_1 . The second cumulant M_2 measures the width of the peak. In (b) σ, σ' are unit vectors connecting to the nearest neighbour (NN) and diagonal nearest neighbour (NNN) in a lattice. (From Ref. [34])

shifts towards lower energies by less than 5% between $T = 0$ and $T = T_N$ [14].

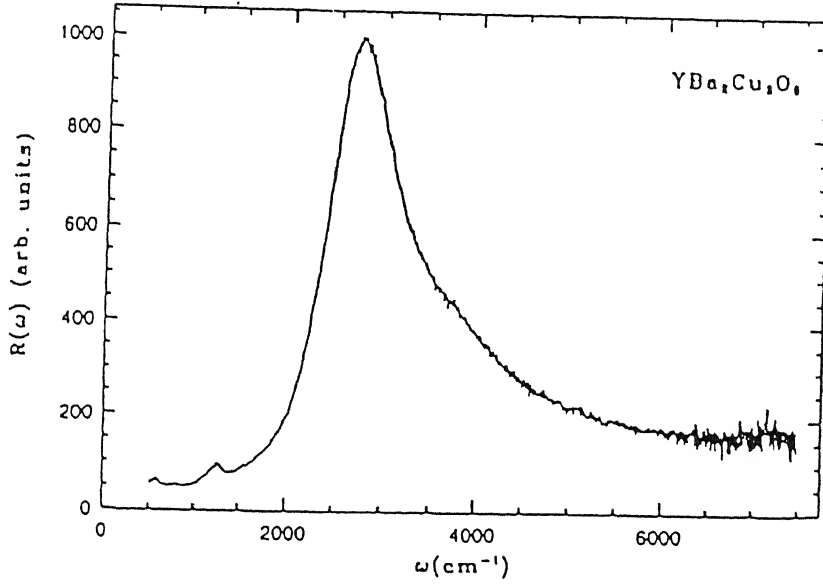


Figure 1.3: Two-magnon Raman scattering intensity shown for $\text{YBa}_2\text{Cu}_3\text{O}_6$ as a function of transferred photon frequency. (From Ref. [44])

Similar features are obtained for $\text{YBa}_2\text{Cu}_3\text{O}_6$ [35, 37]. The two-magnon peak occurs at somewhat lower in frequency and hence yielding a value of $J \simeq 950\text{cm}^{-1}$. The linewidth is even greater than La_2CuO_4 (Fig. (1.3))

Finally, the Raman scattering cross section was investigated in doped cuprates. Sugai *et al.*[38] and Sugai[39] obtained data on two-magnon Raman scattering in $(\text{La}_{1-x}\text{Sr}_x)_2\text{CuO}_4$ for various doping concentration ranging from 0.0 to 0.06 (Fig. (1.4)). It is observed that the position of the peak shifts towards lower frequencies and concomitantly the spectrum becomes broader. The peak structure almost disappears at $x \sim 0.06$. The scattering spectrum in $\text{YBa}_2\text{Cu}_3\text{O}_{6+x}$ is more robust to increase of oxygen concentration. The two-magnon peak survives upto $x \simeq 0.4$ before it becomes almost flat. The rapid suppression of the spectral weight is still an open issue. It could probably be related to the loss of intermediate charge transfer states of the two-magnon scattering process. This suggestion is consistent with the optical conductivity experiments[40] which demonstrates the transfer of spectral weight from above the charge transfer gap to the Drude peak. It was attempted by Lyons and Fleury[41]

to explain the effect of carriers on the spin-excitation spectrum using simple ideas depending upon whether the carriers reside predominantly on the Cu^{2+} or O^{2-} site. In the former case, Cu^{3+} , having no spin, appears as a vacancy (non-magnetic impurity with, of course, no potential barrier locally) in the lattice. In the latter case, the O^- acquires a spin and thus can interact with nearest neighbour Cu^{2+} ions. Regardless of the sign of this interaction, $\text{Cu} - \text{Cu}$ interaction turns ferromagnetic. This sign reversal in J is a local phenomenon and may have a more disruptive effect upon antiferromagnetism than a simple absence of spin in the Cu^{3+} case. But in either of the situations, disorder dilution of the lattice occurs. These ideas do not treat the holes as mobile vacancies. Till date, there is no firm theoretical prediction about the effect of carriers on the Raman spectra.

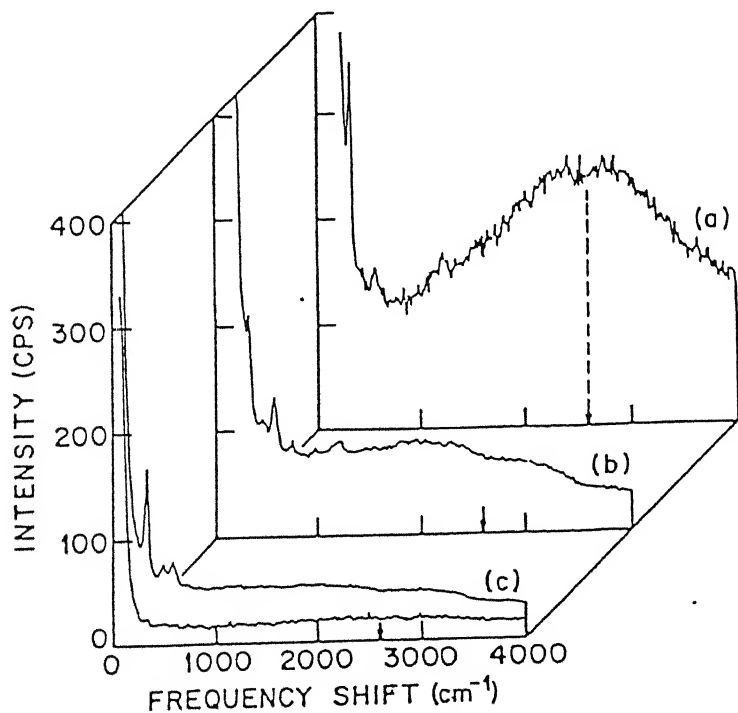


Figure 1.4: Two-magnon Raman spectra of $\text{YBa}_2\text{Cu}_3\text{O}_{6+x}$ for three values of x : (a) 0.0; (b) ~ 0.7 ; (c) ~ 0.9 . Incident wavelength is 4880\AA . (From Ref. [37])

The Fleury-Loudon theory works well for the incoming and outgoing photon frequen-

to be considerably smaller than the energy gap between the conduction and valence bands in copper oxide insulators. But in reality, Raman scattering experiments done on these cuprates, the frequencies are close to the energy gap value (both lying between 2 – 3 eV). A comprehensive study to clarify quantitatively the resonance behaviour was initiated by various groups[42, 43]. Blumberg *et al.* reported resonant Raman lineshape for single CuO_2 layer $\text{Sr}_2\text{CuO}_2\text{Cl}_2$ and bilayered antiferromagnetic systems like $\text{YBa}_2\text{Cu}_3\text{O}_{6+x}$ with a frequency range from 1.65 eV to 3.05 eV. Their data shows a composite structure of the lineshape and a strong non-monotonic dependence of the scattering intensity as a function of the incoming photon frequency. The results were analyzed using the idea of 'Triple Resonance' due to Chubukov and Frenkel[44].

1.5 Recent Theoretical Developments

In the early nineties, Shastry and Shraiman[5] have developed a systematic formalism for understanding Raman scattering from Mott insulators starting from an electronic Hamiltonian. In the absence of any resonance enhancements, they derived the Fleury-Loudon Hamiltonian. However, they find that, when one considers the scattering with the photon frequency close to the band gap in cuprates, in principle a large number of parameters are needed to describe the scattering process. One can organize the various terms by irreducible representations of the lattice symmetry group and by powers of $t/(U - \omega_i)$, where t represents the hopping matrix element, U , the on-site Coulomb term and ω_i being the frequency of the laser beam used. Within this theoretical framework, the intensities in various geometries are, in general not fixed and it may so happen that the signal in A_{1g} (or B_{2g}) geometry is stronger than that in B_{1g} geometry provided ω_i is appropriately tuned.

An interesting new term was observed by Shastry and Shraiman which is a scalar triple product of three spins at different lattice sites, which represents scattering from chiral fluctuations. They have also argued that the scattering of circularly polarized light can not be deduced from linearly polarized light, and by comparing various scattering intensities, in-

cluding the circularly polarized ones, one can disentangle the contributions from this chiral term.

To focus on the main aspects of the calculations due to Shastry and Shraiman, one can write down the Hubbard Hamiltonian which includes the interaction of light with the electronic system as a perturbation,

$$H = H_0 - t \sum_{\langle ij \rangle} (c_{i\sigma}^\dagger c_{j\sigma} e^{ie/hc \int \mathbf{A} \cdot d\mathbf{l}} + \text{h.c.})$$

where H_0 is the unperturbed part,

$$H_0 = U \sum_i n_{i\uparrow} n_{i\downarrow}$$

and A_q^α is the α -th component of the time dependent vector potential at wavevector q . Taking a Fourier transform allows one to write,

$$H = H_0 - e \sum_q j_q^\alpha A_{-q}^\alpha + \frac{e^2}{2} \sum_{q_1, q_2} \tau_q^{\alpha\beta} A_{-q_1}^\alpha A_{-q_2}^\beta$$

The component of current J_q^α and the inverse mass tensor are defined as,

$$J_q^\alpha = \sum_{k, \alpha} \frac{\partial \epsilon_k}{\partial k_\alpha} c_{k+\frac{q}{2}, \sigma}^\dagger c_{k-\frac{q}{2}, \sigma}$$

and,

$$\tau_q^{\alpha\beta} = \sum_{k, \alpha} \frac{\partial^2 \epsilon_k}{\partial k_\alpha \partial k_\beta} c_{k+\frac{q}{2}, \sigma}^\dagger c_{k-\frac{q}{2}, \sigma}$$

The Raman cross-section can now be obtained using Fermi's Golden rule where the initial and the final states are direct product of one-photon states and appropriate matter states (i.e. states of the Hubbard Model) with energies $E_i = \epsilon_i + \omega_i$ and $E_f = \epsilon_f + \omega_f$. So the inelastic scattering rate for transitions can be expressed as,

$$R = \sum_{i, f} \left| \langle f | \hat{M} | i \rangle \right|^2 \delta(E_f - E_i)$$

where \hat{M} is the Raman scattering operator comprising of two terms - a resonant (M_R) and a

on-resonant term (M_N). Hence,

$$\langle f|\hat{M}|i\rangle = \sum_{\alpha,\beta} (e_i^\alpha)(e_f^\beta)^* \langle f|M_R^{\alpha\beta} + M_N^{\alpha\beta}|i\rangle$$

e_i^α and $(e_f^\beta)^*$ are the polarization of the incoming and outgoing photons. $M_R^{\alpha\beta}$ is the resonant term which is relevant for discussion of the insulating phase of cuprates, whereas the non-resonant term $M_N^{\alpha\beta}$ becomes important for the doped case, since the inverse mass tensor $\tau_{q_1+q_2}^{\alpha\beta}$ has non-zero matrix elements between the states in the lower band, i.e. with low energy transfer.

The resonant term can be written as a combination of two terms — a direct and an exchange term shown in Fig. (1.5),

$$\langle f|M_R|i\rangle = \sum_{\alpha} \langle 0; \sigma_f | j_\mu(r) | 1; \alpha \rangle \langle 1; \alpha | j_\nu(r') | 0; \sigma_i \rangle \left[\frac{e_\mu^f e_\nu^i}{U - \omega_i} + \frac{e_\mu^i e_\nu^f}{U + \omega_f} \right]$$

$M_R^{\alpha\beta}$ can be decomposed into various scattering geometries pertaining to the D_{4h} tetragonal point group. For convenience of the future discussion three of the most commonly used scattering geometries are shown in Fig. (1.6)[46]. It was shown by Shastry and Shraiman that M_R can be expressed, to lowest order in $\frac{t}{U}$, as the Fleury-Loudon Hamiltonian.

As mentioned earlier, the expansion in the Shastry and Shraiman was actually in powers of $\frac{t}{U - \omega_i}$ (when $\omega_i \ll U$ then the expansion can be thought to be in power of $\frac{t}{U}$ as mentioned at the end of last paragraph) and for the light scattering experiments on high- T_c cuprates ω is roughly of the order U . Then one needs to question the validity of Fleury-Loudon Hamiltonian to calculate the scattering cross-section.

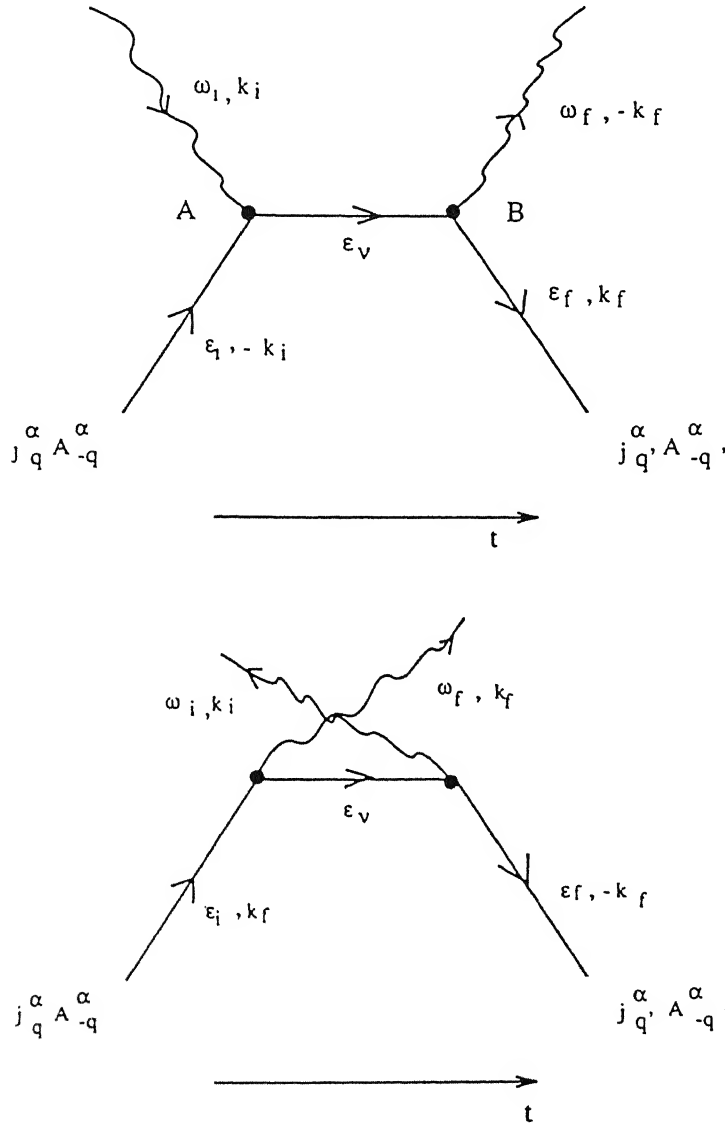


Figure 1.5: Diagrammatic representation of the Direct (top) and exchange (below) terms appearing in the resonant Matrix element $M_R^{\alpha\beta}$ (see the discussion in the text)

Chubukov and Frenkel[44] studied the case when ω_i or $(\omega_f) \simeq U$ (resonant two-magnon scattering) and looked at the variation of the overall scale of the coupling constant A (see Eq. 1.1) with the incident photon frequency ω . The problem was tackled diagrammatically and only the diagrams (Fig. (1.7)) which contribute to the intraband processes are retained. This idea has previously been applied for calculating the Raman intensity from two-phonon

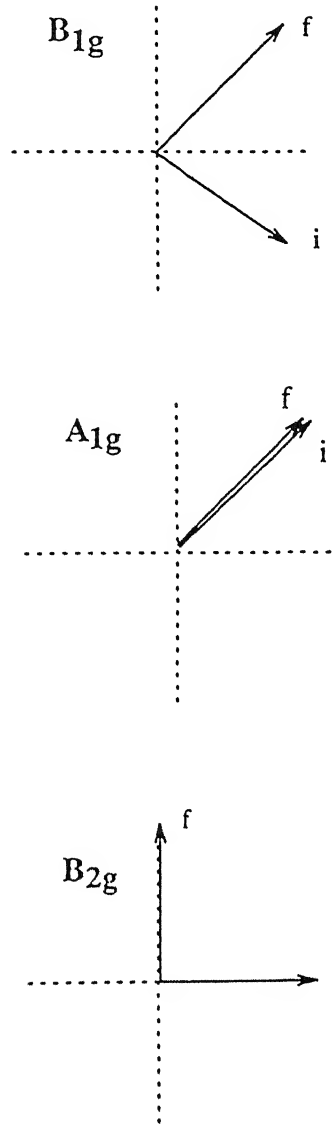
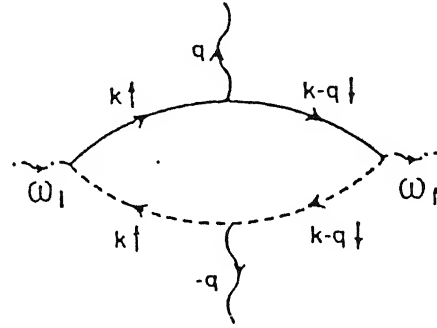


Figure 1.6: Commonly used scattering geometries.

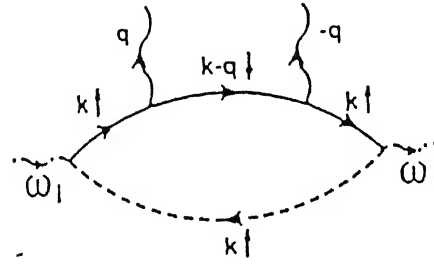
process.[47] From the explicit frequency integral of the diagrams, it can be noticed that these diagrams have more number of denominators than the ones relevant for the Fleury-Loudon case. There are in fact three of them, and all three vanish simultaneously for the photon and magnon frequencies satisfying some specific energy-momentum relation. This phenomenon is called as 'Triple Resonance' by the authors. Also they find that the 'Triple Resonance' yields

the strongest divergence of the Raman scattering cross-section and alongwith incorporating the spin density wave (SDW) dispersion relation for the carriers, the unusual experimental features of the two-magnon lineshape and the two-magnon peak intensity dependence on the incoming photon frequency can be explained.

The success of the theory relates to the experiments recently done on the Cu-Oxide based materials. The two-peak structure obtained in the two-magnon profile in Pr_2CuO_4 [48], a stronger one at $\omega \sim 3J$ and another one at $\sim 4J$ is in perfect accordance with the theory. The theory predicts scattering in both B_{1g} and A_{1g} geometry which is an experimental reality, as seen before. Furthermore, the calculation supports a single maximum, while the diagrams relevant to the Fleury-Loudon case might have given two peaks, one each at incoming and outgoing photon frequencies, commonly termed as incoming and outgoing resonances.[49].



(a)



(b)

Figure 1.7: Diagrams which are important for the resonant processes. All the three denominators in the diagram (a) can vanish simultaneously, which is known as 'Triple Resonance'. Additional relevant diagram (which is less dominant than (a)) is shown in (b). Here the fermions belonging to a valence (conduction) band is represented by a dashed (solid) line. The emitted magnons are denoted by the solid wavy lines whereas the dashed wavy lines are the incoming and outgoing photons. (From Ref. [44])

Recently, Schönfeld *et al.*[50] revisited the issue of resonance enhancement of the two-magnon intensity in a spin-density-wave (SDW) antiferromagnet. In their diagrammatic formulation they have carried out a systematic microscopic derivation for the two-magnon scattering intensity explicitly taking into account the resonance structure of the photon-

magnon coupling vertex. Essentially they confirmed the conclusions of the Triple Resonance theory due to Chubukov and Frenkel for the resonant scattering process.

Morr *et al.*[51] have studied two-magnon Raman scattering in a two-layer antiferromagnet for both Fleury-Loudon and the resonant case. It enables one to obtain an estimate of the interplanar exchange constant (J_{\perp}). In particular, they observed qualitatively new features for the scattering profile in the A_{1g} geometry. It is easy to show that a non-zero J_{\perp} gives a signal in A_{1g} geometry even for the Fleury-Loudon case. In addition to that, they obtained a strong resonance in the A_{1g} geometry for the transferred photon frequency ω ($= \omega_i - \omega_f$) to be equal to $4(J_{\parallel}J_{\perp})^{1/2}$ and at resonance, the amplitude of the A_{1g} signal is larger than that of the B_{1g} at the same frequency. The value of J_{\perp} as obtained from their calculation is $\sim 0.1J_{\parallel}$ and the upper limit is $\sim 0.25J_{\parallel}$. Hence J_{\perp} for the double-layered $YBa_2Cu_3O_6$ can be estimated to be $12MeV < J_{\perp} < 30MeV$ for $J_{\parallel} \simeq 120MeV$. This is consistent with the NMR data[52] $5MeV < J_{\perp} < 20MeV$ obtained on double-layered $Y_2Ba_4Cu_7O_{15}$, but has poor agreement with the infrared transmission and reflection measurements[53] where J_{\perp} is $0.55J_{\parallel}$.

Recently Nori *et al.*[54] took into account of magnon damping arising due to the interaction between the magnons and the lattice vibrations or phonons. They calculated the Raman spectrum for a $S = 1/2$ Heisenberg antiferromagnet by Exact Diagonalization and Quantum Monte Carlo techniques for systems ranging from 16 to 144 sites. They propose that the phonon-magnon interaction leads to a random fluctuation of the Heisenberg exchange J . They assumed that the random couplings δJ_{ij} can be drawn for each bond independently from a Gaussian distribution of width σ . A simple calculation to get an estimate of σ leads to a rather high value $\sim 0.4J$. Such an enormous variation of the exchange coupling seems physically unreasonable[50]. However, the Raman spectra calculated taking this random model show good agreement with the experiments done on the undoped cuprates. The lineshape shows a substantial broadening, a profound asymmetry appears in the higher frequency region due to the existence of a spectral weight and the intensity persists well beyond $4J$. In

Fig. (1.8), the lineshapes in the B_{1g} and A_{1g} geometries as obtained by Nori are shown which show a strong evidence that the Raman lineshape gets considerably modified due to interaction with the low-energy phonons which randomly distort the lattice.

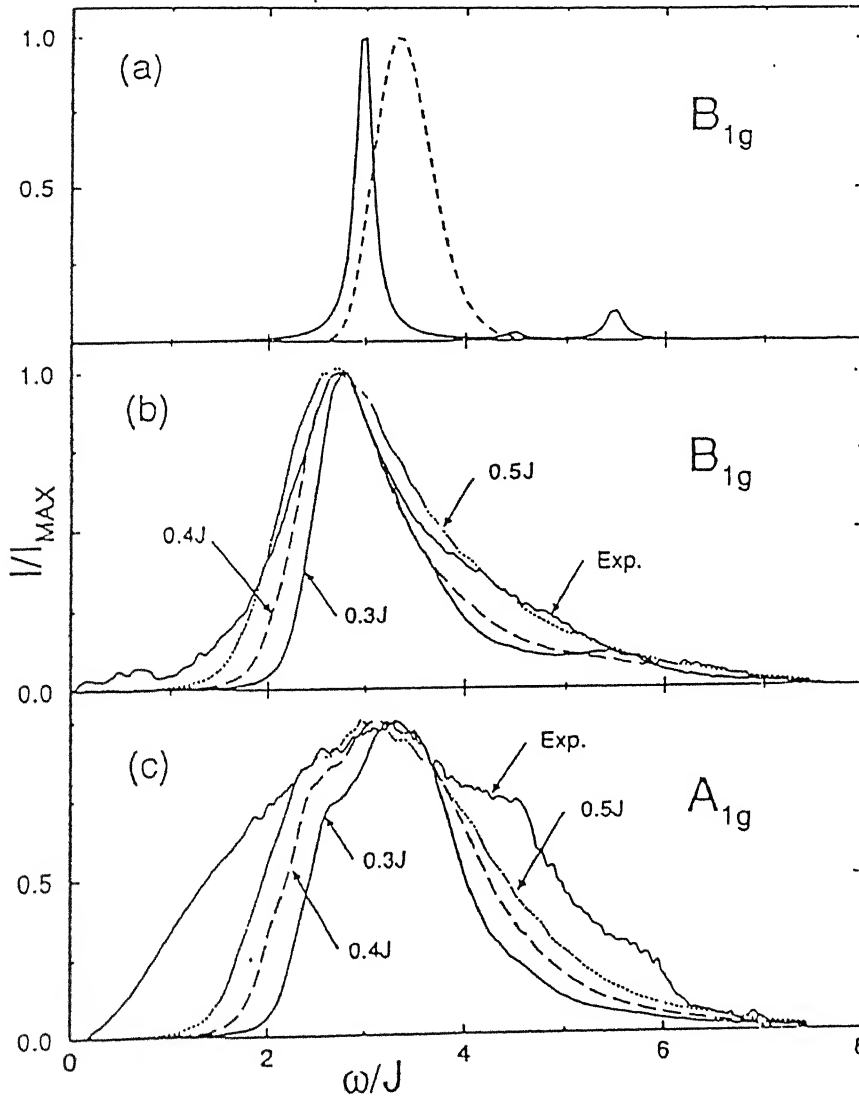


Figure 1.8: Normalized Raman cross-section $I(\omega)/I_{\text{max}}$ is shown as a function of scattered photon frequency ω (in units of J). The plot in solid line shown in (a) corresponds to the spectra obtained by Exact Diagonalization with $N = 16$ and the dashed one is obtained from Quantum Monte Carlo studies for $N = 144$ for $\sigma = 0.0$ in the B_{1g} symmetry. The plots shown in (b) and (c) corresponds to the scattering intensity in B_{1g} and A_{1g} symmetry corresponding to $\sigma = 0.3J$, $0.4J$, $0.5J$. (From Ref. [54])

Also Canali and Girvin[55] have attempted a systematic analysis within the spin-wave theory to incorporate the contribution coming from the four-magnon process to explain some of the anomalous features mentioned in the last paragraph. Although the first three moments of the scattering intensity are in good agreement with experiments and the series expansion results due to Singh et al.[34], but the full lineshape could not be successfully explained. The integrated four-magnon intensity is merely 2.9% of that coming from two-magnon processes. So, it seems the four-magnon contribution can barely modify the overall two-magnon Raman lineshape. Furthermore, they observed that the four-magnon peak frequency is 2.5 times larger than that of two-magnon. Hence this leads one to conclude that the four-magnon scattering can not contribute to the spectral intensity at a frequency close to $4J$.

Finally, before winding up the discussion on the theoretical progress that has taken place in recent times, I present a brief account of the Raman scattering studies performed in the $t - J$ model in presence of holes[56, 57]. The calculations were performed using Exact Diagonalization studies on a 4×4 lattice in the B_{1g} scattering geometry. The cases arising out of no hole, one hole and two holes are discussed. The study for the no-hole case reveals good agreement with the series expansion results obtained for the cumulants of the distribution[34]. In presence of holes the two-magnon shifts peak downward in energy and the intensity reduces with respect to the no-hole case, while the spectral weight appears at higher energies. The position of the two-magnon peak for the one hole (static) case as a function of transferred photon frequency has got good agreement with what one expects in the Ising limit from the flipping of two spins in the vicinity of the hole where the number of broken bonds created by the Fleury-Loudon term is only five while away from the hole is six. For the two-hole case (where the two holes are neighbours in the ground state in order to minimize the number of broken bonds) 3 possibilities arise, viz. both the spins flip away from the holes, one of them in the vicinity and both are in the vicinity of the holes. In the Ising limit the peaks occurring from such cases should be separated in energy by $\sim 0.5J$ and are in good agreement with the numerical work.

For a dynamical hole, Gagliano and Bacci[57] find that the spectrum broadens out (see Fig. (1.9)) while the two-magnon peak at $\sim 3J$ does not continue to be the dominant one and more peak structures appear in the lower energy regime. These effects have been experimentally observed[38] and show the relevance of doping concentration on the spin-fluctuation dynamics.

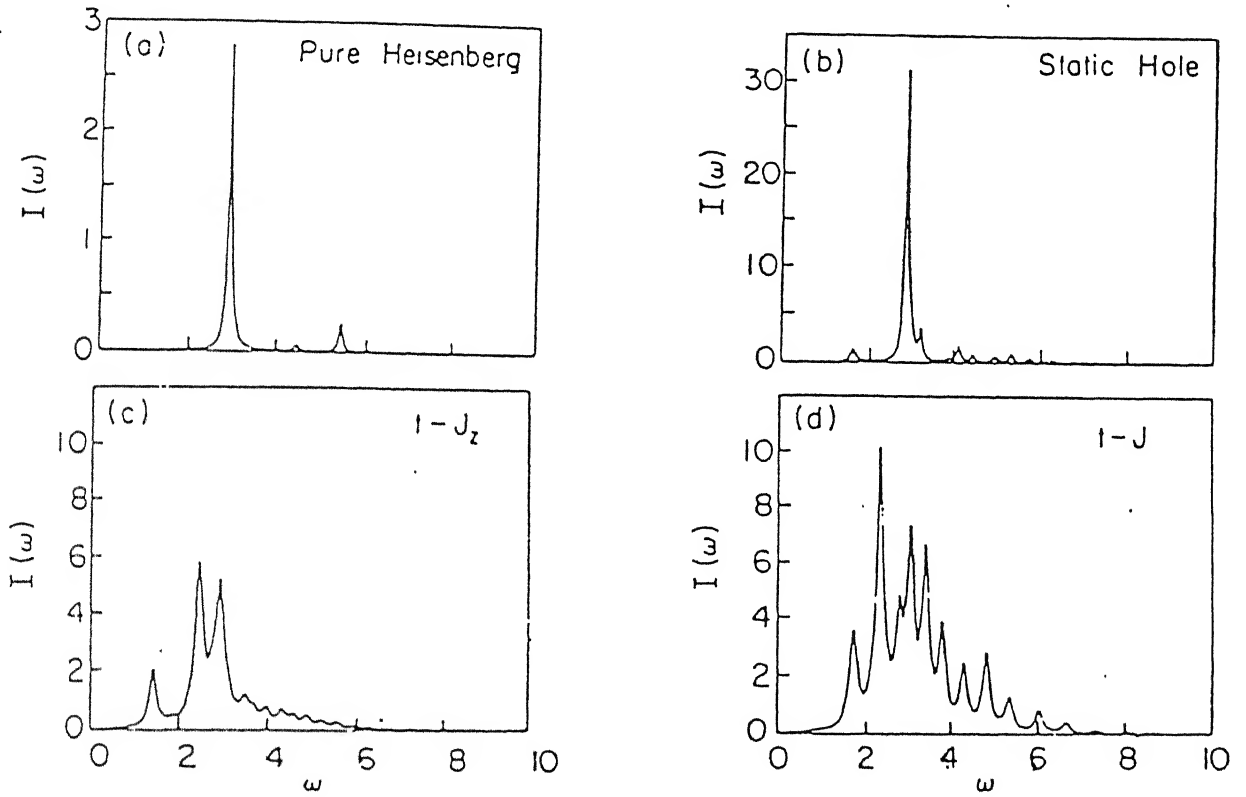


Figure 1.9: B_{1g} Raman spectrum for $J = 1$ in a 4×4 lattice, obtained from Exact Diagonalization studies. (a) Pure Heisenberg model; (b) static vacancy in the Heisenberg, (c) dynamical hole in the $t - J_z$; (d) dynamical hole in $t - J$ model. (From Ref. [57])

In spite of a great deal of success in explaining the two-magnon Raman lineshape for the insulating cuprates, at least three characteristic features do not get completely resolved – anomalously large linewidth of the profile, asymmetry towards the higher energy region with respect to the two-magnon peak and the lineshape considerably extending beyond $4J$ which corresponds to the maximum of joint magnon DOS. In my thesis, I have addressed these issues and in addition, investigated the effect of disorder on two-magnon Raman scattering spectra in antiferromagnets.

1.6 Brief Outline of the Thesis

In Chapter 2 we have developed a systematic diagrammatic scheme in order to study two-magnon Raman scattering in a pure antiferromagnet. There the fermionic structure of the magnon interaction vertex is studied at order $1/\mathcal{N}$ where \mathcal{N} denotes the orbital degeneracy. The full two-magnon propagator is then evaluated by including the interaction between the magnons at the ladder sum level and the scattering intensity is obtained by taking the imaginary part of the propagator. Finally the calculations are extended to the intermediate coupling regime in order to make connections with the experiments done on cuprate insulators. We also make an attempt to incorporate zero temperature magnon damping in a phenomenological way which yields a better agreement with the experiments performed on La_2CuO_4 .

In Chapter 3 we study the effect of hopping disorder in an antiferromagnet using both perturbation theory and exact eigenstate method. Here the lattice distortions arising out of quantum and thermal fluctuations are taken into account which essentially renders the exchange couplings J_{ij} , and hence the hopping integral t_{ij} , which depend upon the instantaneous positions of the ions, random. It was shown that while the low-energy long wavelength, low energy magnon modes are only weakly affected, the high energy modes are strongly renormalized because of a cooperative effect arising from local correlations in hopping disorder. We also discussed the implication of this highly asymmetric magnon energy renormalisation for two-magnon Raman scattering in cuprate antiferromagnets.

Chapter 4 deals with obtaining the Raman scattering intensity numerically in presence of hopping disorder. A consistent scheme of mode assignments is prescribed which establishes a one-to-one correspondence between the pure and disordered system. It was shown that for a substantially weak disorder, several features like the linewidth to peak position ratio, asymmetry with respect to the two-magnon peak and the spectral weight persisting all the way upto $6J$ agree with the experimental data.

In **Chapter 5** we have calculated the Raman scattering cross-section in presence of on-site disorder. It is found that the magnon modes are damped and this damping is obtained by considering the vertex corrections[58]. Even though it is observed that this damping is proportional to fourth power of the disorder strength, still for the high energy modes which are particularly relevant for the Raman studies, the damping goes as the DOS which shows a divergence at the upper band edge ($2J$) and hence is a significant quantity. We have utilized this damping to calculate the Raman lineshape for different disorder strengths. It is seen that there occurs a broadening of lineshape with a noticeable change towards the high frequency regime, whereas the correction in the low energy region is negligible.

In **Chapter 6** we develop a formalism to obtain the two-magnon Raman scattering intensity in real space. This involves calculation of the two-magnon propagator in terms of the eigensolutions of the zeroth order particle-hole propagator $[\chi^0]$. Finally the imaginary part of the two-magnon propagator is taken to obtain the scattering intensity which can be computed for various kinds of disorder such as hopping disorder, potential disorder, vacancies etc.

Bibliography

- [1] C.V. Raman, Ind. J. Phys. **2**, 387 (1928)
- [2] C.V. Raman and K.S. Krishnan, Nature, **121**, 501 (1928)
- [3] L. Brilluoin, Ann. Phys. (Paris) **17**, 88 (1922)
- [4] L.I. Mandelstam, Zh. Radio-Fiziko-Khimicheskogo Obschestva, **58**, 381 (1926)
- [5] R.J. Elliot and R. Loudon, Phys. Lett., **3**, 189 (1963)
- [6] P.A. Fleury, S.P.S. Porto, L.E. Cheesman and H.J. Guggenheim, Phys. Rev. Lett. **17**, 84 (1966)
- [7] P.A. Fleury, S.P.S. Porto and R. Loudon, Phys. Rev. Lett., **18**, 658 (1967)
- [8] P.A. Fleury, Phys. Rev. Lett., **21**, 151, (1968)
- [9] P.A. Fleury, Phys. Rev., **180**, 591, (1969)
- [10] R.J. Elliot et al., Phys. Rev. Lett., **21**, 147 (1968)
- [11] R.J. Elliot and M.F. Thorpe, J. Phys. C (Solid State Phys.), **2**, 1630 (1969)
- [12] M.F. Thorpe, J. Appl. Phys. **41**, 892 (1970)
- [13] J.B. Parkinson, J. Phys. C (Solid State Phys.), **2**, 2003 (1969)
- [14] P.A. Fleury and H.J. Guggenheim, Phys. Rev. Lett., **24**, 1346 (1970)

- [15] M.G. Cottam and D.J. Lockwood in *Light Scattering in Magnetic Solids* (John Wiley & Sons, 1986), Page – 133
- [16] N. Zubarev, *Sov. Phys. – Usp.* **3**, 320 (1960)
- [17] P.A. Fleury and R. Loudon, *Phys. Rev.*, **166**, 514, (1968)
- [18] J. Sólyom, *Z. Physik*, **243**, 382, (1971)
- [19] R.W. Davies, S.R. Chinn and H.J. Zeiger, *Phys. Rev. B*, **4**, 992 (1971)
- [20] U. Balucani and V. Tognetti, *Phys. Rev. B*, **8**, 4247 (1973)
- [21] T. Kawasaki, *J. Phys. Soc. Japan*, **29**, 1144 (1970)
- [22] P.A. Fleury and H.J. Guggenheim, *Phys. Rev. B*, **12**, 985 (1975)
- [23] H. Mitlehner et al., *Solid State Commun.*, **9**, 2039 (1971)
- [24] M. Buchanan et al., *J. Phys. C* **5**, 2011 (1972)
- [25] S.M. Rezende et al., *J. Raman Spectrosc.*, **10**, 173 (1981)
- [26] A. Oseroff, P.S. Pershan and M. Kesligian, *Phys. Rev.*, **188**, 1046 (1969)
- [27] G. Parisot et al., *J. Appl. Phys.*, **41**, 890 (1970)
- [28] G. Parisot et al., *J. Physique*, **32**, C1-803 (1971)
- [29] P. Moch, R. Moyal, C. Dugautier and H.J. Guggenheim, *J. Physique*, **32**, C1-806 (1971)
- [30] D.J. Lockwood et al., *J. Phys. C*, **12**, 4611 (1979)
- [31] J.G. Bednorz and K.A. Müller, *Z. Phys. B*, **64**, 189 (1986)
- [32] D. Vaknin et al., *Phys. Rev. Lett.*, **58**, 2802 (1987)
- [33] G. Shirane et al., *Phys. Rev. Lett.* **59**, 1613 (1987)

-
- [34] R.R.P. Singh, P.A. Fleury, K.B. Lyons and P.E. Sulewski, *Phys. Rev. Lett.* **62**, 2736 (1989)
- [35] K.B. Lyons, P.A. Fleury, J.P. Remeika, A.S. Cooper and T.J. Negran, *Phys. Rev. B*, **37**, 2353 (1988)
- [36] K.B. Lyons and P.A. Fleury, *Phys. Rev. B*, **37**, 2353 (1988)
- [37] K.B. Lyons et al., *J. Appl. Phys.*, **64**, 6075 (1988)
- [38] S. Sugai, S. Shamoto and M. Sato, *Phys. Rev. B* **38**, 6436 (1988)
- [39] S. Sugai in *Mechanism of High-Temperature Superconductivity* ed. H. Kamimura and K. Oshiyama, Springer-Verlag Berlin Heidelberg (1989)
- [40] S. Uchida et al., *Phys. Rev. B*, **43**, 7942 (1991)
- [41] K.B. Lyons et al., *Phys. Rev. B*, **39**, 9693 (1989)
- [42] G. Blumberg et al., *Phys. Rev. B*, *Phys. Rev. B*, **49**, 13296 (1994), **53**, 11930 (1996)
- [43] S. Sugai, *Phys. Rev. B*, **39**, 4306 (1989)
- [44] A.V. Chubukov and D.M. Frenkel, *Phys. Rev. Lett.* **74**, 3056 (1995), *Phys. Rev. B* **52**, 9760 (1995)
- [45] B.S. Shastry and B.I. Shraiman, *Phys. Rev. Lett.*, **65**, 1068 (1990), *Int. J. Mod. Phys. B*, **5**, 365 (1991)
- [46] W. Brenig, *Phys. Rep.*, **251**, 155 (1995)
- [47] M.V. Klein, *Phys. Rev. B*, **24**, 4208 (1981)
- [48] I. Tomeno et al., *Phys. Rev. B*, **43**, 3009 (1991)
- [49] M. Cardona in *Light Scattering in Solids II* ed. M. Cardona and G. Güntherodt, Springer-Verlag, New York (1975).

-
- [50] F. Schönfeld, A.P. Kampf and E. Müller Hartmann, Z. Phys. B, **102**, 25 (1997)
 - [51] D.K. Morr, A.V. Chubukov, A.P. Kampf and G. Blumberg, Phys. Rev. B, **54**, 3468 (1996)
 - [52] S. Shamoto et al., Phys. Rev. B, **48**, 13817 (1993), S.M. Hayden et al., Phys. Rev. Lett., **66**, 821 (1991), **67**, 3622 (1991)
 - [53] R. Stern et al., Phys. Rev. B, **50**, 426 (1994)
 - [54] F. Nori et al., Phys. Rev. Lett., **75**, 553 (1995)
 - [55] C.M. Canali and S.M. Girvin, Phys. Rev. B, **45**, 7127 (1992)
 - [56] E. Dagotto and D. Poilblanc, Phys. Rev. B, **42**, 7940 (1990)
 - [57] E. Gagliano and S. Bacci, Phys. Rev. B, **42**, 8772 (1990)
 - [58] A. Singh, M. Ulmke and D. Vollhardt, Report Number 9803094

Chapter 2

Two-Magnon Raman Scattering for a Pure Antiferromagnet

2.1 Introduction

As mentioned in the last chapter extensive studies have been carried out in antiferromagnets such as RbMnF_3 , MnF_2 , K_2NiF_4 , [1–5] and a good theoretical understanding exists for these systems with spin $S \geq 1$, within the interacting-magnon theory for the Quantum Heisenberg Antiferromagnet (QHAF) [6]. Recently there has been renewed interest since studies in La_2CuO_4 (a $S = 1/2$ system) have indicated evidence of substantial quantum spin fluctuations, [7–9] and the observed two-magnon Raman scattering linewidth is much too broad to be explained within the classical theory. [4] Moreover, scattering intensities are observed in geometries which, in the classical approximation, should yield no scattering. Interest in two-magnon Raman scattering continues also because upon doping with holes, the two-magnon peak broadens out and relaxes into the Raman continuum. In $\text{YBa}_2\text{Cu}_3\text{O}_{6+x}$, for example, the intensity of the two-magnon feature decreases rapidly with increasing x , and virtually disappears at $x = 0.5$. [10]

While theoretically two-magnon Raman scattering has been studied extensively within the QHAF, there have been so far only limited attempts to systematically study this within the Mott-Hubbard model. Recently a strong-coupling expansion in powers of t/U , the hopping term, has been carried out, and the Fleury-Loudon Hamiltonian has been obtained at the

second order level.[11] In this treatment, the hopping term is extended to include the gauge term $e \frac{i\hbar c}{\hbar c} \int_i^j \mathbf{A} \cdot d\mathbf{l}$ arising from the external transverse electro-magnetic field, and the transition matrix elements which determine the Raman scattering are obtained within a strong-coupling expansion. This has also been described in a somewhat detailed manner in the last chapter. However it appears that so far no systematic, formally weak-coupling expansion has been carried out which can continuously interpolate between the small- U and large- U limits.

Significantly, in the small- and intermediate- U regimes of the Mott-Hubbard antiferromagnet, when the interaction term U is less than or comparable to the free-electron bandwidth $B = 2Zt$ where $Z = 2D$, D being the dimensionality, the one-magnon density of states (DOS) exhibits a peak structure which broadens and shifts to lower energies with decreasing U . [12, 13] In contrast, in the large- U limit, the one-magnon DOS diverges at the upper band edge due to zone-boundary magnons at energy DJ , where $J = 4t^2/U$ is the exchange energy. This peak structure resembles a broadening due to magnon-interaction, and must be incorporated in any realistic theory of two-magnon Raman scattering when applied to the small- and intermediate- U regimes. Since it is believed that La_2CuO_4 does actually fall in the intermediate- U regime, a formally weak-coupling expansion scheme has a potential application as well.

In this chapter we describe a perturbation-theoretic, diagrammatic scheme for systematically obtaining the two-magnon Raman scattering in an antiferromagnet. Since within the Hubbard model itself there is no formal expansion parameter, we make use of the generalized Hubbard model with \mathcal{N} orbitals per site,[14] and develop a systematic expansion in powers of $1/\mathcal{N}$. This perturbation-theoretic scheme, which preserves the spin rotational symmetry, and hence the Goldstone mode, order by order in the perturbation theory, has been used earlier to systematically obtain quantum corrections to sublattice magnetization, spin-wave energy, perpendicular susceptibility and ground-state energy of a Hubbard antiferromagnet.[14] When this formally weak-coupling perturbative approach is carried to the large- U (strong-coupling) limit, which is analytically the simplest, one recovers identical results as obtained within the $1/S$ -expansion for the spin S Quantum Heisenberg model. We shall see that this holds for the two-magnon Raman scattering effect as well.

In spin-pair excitations by light, the two magnons are created on nearest-neighbour (NN) sites, and therefore strong interaction effects between magnons are important in a quantitative analysis. Considering a two-dimensional $S = 1/2$ system for concreteness, two spins flipped involve an excitation energy $4J$ when far apart but only energy $3J$ when on NN sites. This suggests that the interaction energy between magnons at the lowest order level is $-J$ when on NN sites, which shifts the peak in the two-magnon Raman scattering intensity to energy $\sim 3J$. Indeed, we find within our perturbation-theoretic approach, that to the lowest order in $1/V$, the interaction energy between magnons on NN sites is instantaneous and precisely $-J$ in the large- U limit.

In section 2.2 the two-magnon propagator and magnon-magnon interaction are considered at the lowest-order level in an expansion in powers of t^2/U^2 . In the next section we have extended the calculations to the intermediate- U regime by incorporating higher order terms in the magnon propagator and interaction terms. Finally in section 2.4 we make a simple estimate for zero temperature magnon damping and incorporate it to evaluate the Raman scattering intensity in the B_{1g} symmetry and compare with the observed Raman spectrum in La_2CuO_4 .

2.2 Two-magnon Propagator in the large- U limit

The Fleury-Loudon Hamiltonian which represents the interaction of spin pairs with photon pairs, as appears in Eq. (1.1), is written as,

$$H_R = A \sum_{\mathbf{r}, \hat{\delta}} (\mathbf{E}_{\text{inc}} \cdot \hat{\delta})(\mathbf{E}_{\text{sc}} \cdot \hat{\delta}) \mathbf{S}(\mathbf{r}) \cdot \mathbf{S}(\mathbf{r} + \hat{\delta}), \quad (2.1)$$

where the various symbols have been described in chapter 1. The sum over \mathbf{r} ensures that the spin-pair excitation has zero total wavevector as required by momentum conservation since the photons involved have essentially zero wavevector. To calculate the two-magnon spectrum, we need to extract parts of the spin operators which combine to create a pair of magnons. We focus therefore on the transverse part of the spin pair operator,

$$P_{\hat{\delta}} \equiv \sum_{\mathbf{r}} \mathbf{S}(\mathbf{r}) \cdot \mathbf{S}(\mathbf{r} + \hat{\delta}).$$

As mentioned in the last chapter, the two-magnon Raman scattering intensity is related to the correlation function of the spin-pair operator $P_{\hat{\delta}}$, which can be obtained as the imaginary part of the corresponding propagator. We consider the following time-ordered two-magnon Green's function,

$$G_{\hat{\delta}, \hat{\delta}'}(\Omega) = -i \int dt e^{i\Omega(t-t')} \langle \psi_G | T \left[\sum_{\mathbf{r}} S^-(\mathbf{r}, t) S^+(\mathbf{r} + \hat{\delta}, t) \right. \\ \left. \sum_{\mathbf{r}'} S^+(\mathbf{r}', t') S^-(\mathbf{r}' + \hat{\delta}', t') \right] | \psi_G \rangle \quad (2.2)$$

As mentioned earlier, in this chapter we develop a systematic perturbation expansion for this two-magnon propagator within the Hubbard model. We show the fermionic structure of the magnon-interaction vertex to $O(1/N)$, and evaluate the resulting two-magnon propagator in the large- U limit in order to make contact with the known results within the Heisenberg model formalism. Extension to higher orders in $(1/N)$ and to the intermediate- U regime can then be carried out.

At this point we will take a short break to discuss the spin-wave excitations in an antiferromagnet[12]. Spin waves are the lowest lying collective excitations that represent transverse spin fluctuations about the antiferromagnetic ground state. The spin-wave modes show up in the form of a pole in the transverse spin susceptibility evaluated in the AF ground state. The transverse spin susceptibility is defined in terms of the spin raising and lowering operators as,

$$\chi^{-+}(\mathbf{r}, t; \mathbf{r}', t') = i\theta(t - t') \langle \Psi_{AF} | [S^-(\mathbf{r}, t), S^+(\mathbf{r}', t')] | \Psi_{AF} \rangle. \quad (2.3)$$

Within random phase approximation (RPA) or at the ladder sum level for the above propagator one obtains,

$$\chi^{-+} = \frac{\chi^0}{1 - U\chi^0} \quad (2.4)$$

The zeroth-order term in the susceptibility, χ^0 , is evaluated with respect to the AF ground state and is given by the following relation in terms of the one-particle Green's functions,

$$\chi^0(r, r'; \Omega) = i \int_{-\infty}^{+\infty} \frac{d\Omega'}{2\pi} G^\dagger(r, r'; \Omega') G^\downarrow(r', r; \Omega' - \Omega). \quad (2.5)$$

The full RPA propagator χ^{-+} corresponding to the pure case has been discussed elaborately earlier in the large- U [12] and intermediate- U [12] regime.

Now we consider the non-interacting limit of the two-magnon propagator, $G_{\hat{\delta}, \hat{\delta}'}^0(\Omega)$, decompose it into the irreducible representations of the lattice, and then develop the perturbative expansion in powers of the magnon-interaction. In the non-interacting limit we have a magnon pair propagating from NN sites $\mathbf{r}, \mathbf{r} + \hat{\delta}$ to $\mathbf{r}', \mathbf{r}' + \hat{\delta}'$, and in terms of the magnon propagators, χ^{-+} and χ^{+-} , we obtain for the two-magnon propagator in the non-interacting limit:

$$G_{\hat{\delta}, \hat{\delta}'}^0(\Omega) = i \int dt e^{i\Omega(t-t')} \sum_{\mathbf{r}, \mathbf{r}'} \chi^{-+}(\mathbf{r}, t; \mathbf{r}', t') \chi^{+-}(\mathbf{r} + \hat{\delta}, t; \mathbf{r}' + \hat{\delta}', t') \quad (2.6)$$

Here we note that since $\hat{\delta}, \hat{\delta}'$ are vectors joining nearest neighbours, if \mathbf{r} and \mathbf{r}' belong to sublattices μ and ν respectively ($\mu, \nu = A/B$), then $\mathbf{r} + \hat{\delta}$ and $\mathbf{r}' + \hat{\delta}'$ belong to opposite sublattices $\bar{\mu}$ and $\bar{\nu}$ respectively, and therefore we obtain,

$$G_{\hat{\delta}, \hat{\delta}'}^0(\Omega) = i \int \frac{d\Omega_1}{2\pi} \sum_Q \sum_{\mu\nu} [\chi^{-+}(Q, \Omega_1)]_{\mu\nu} [\chi^{+-}(-Q, \Omega - \Omega_1)]_{\bar{\mu}\bar{\nu}} e^{iQ \cdot (\hat{\delta} - \hat{\delta}')} \quad (2.7)$$

It is convenient to (i) decompose $G_{\hat{\delta}, \hat{\delta}'}^0(\Omega)$ in terms of the irreducible representations $\phi_n(Q)$ of the lattice and (ii) consider G^0 in a 2×2 matrix form within the two-sublattice basis. This greatly simplifies the summation of the perturbative series in powers of magnon interaction, as we will see later. For the n -th irreducible representation, we obtain,

$$[G_n^0(\Omega)]_{\mu\nu} = i \int \frac{d\Omega_1}{2\pi} \sum_Q \phi_n^2(Q) [\chi^{-+}(Q, \Omega_1)]_{\mu\nu} [\chi^{+-}(-Q, \Omega - \Omega_1)]_{\bar{\mu}\bar{\nu}} \quad (2.8)$$

Finite-temperature evaluation of $[G_n^0(\Omega)]_{\mu\nu}$ can now be carried out in the standard way. Replacing the frequency Ω by the bosonic Matsubara frequency $i\Omega_m$ and the frequency integral over Ω_1 by a contour integral, and taking the contour around each singularity in the clockwise direction, we obtain,

$$[G_n^0(i\Omega_m)]_{\mu\nu} = i \oint \frac{d\Omega_1}{2\pi} \sum_Q \phi_n^2(Q) [\chi^{-+}(Q, \Omega_1)]_{\mu\nu} [\chi^{+-}(-Q, i\Omega_m - \Omega_1)]_{\bar{\mu}\bar{\nu}} \frac{1}{e^{\beta\Omega_1} - 1} \quad (2.9)$$

Adding the residues from the four poles, taking $e^{\beta i\Omega_m} = 1$, and finally replacing $i\Omega_m$ by Ω , yields the following matrix elements of $[G_n^0(\Omega)]$ [12],

$$\begin{aligned} [G_n^0(\Omega)]_{AA} &= \sum_Q \phi_n^2(Q) \left(\frac{DJ}{\Omega_Q} \right)^2 \left[1 + \left(\frac{\Omega_Q}{DJ} \right)^2 - \left(\frac{\Omega}{DJ} \right) \right] \frac{\Omega_Q}{\Omega^2 - 4\Omega_Q^2} \coth \left(\frac{\beta\Omega_Q}{2} \right) \\ [G_n^0(\Omega)]_{BB} &= \sum_Q \phi_n^2(Q) \left(\frac{DJ}{\Omega_Q} \right)^2 \left[1 + \left(\frac{\Omega_Q}{DJ} \right)^2 + \left(\frac{\Omega}{DJ} \right) \right] \frac{\Omega_Q}{\Omega^2 - 4\Omega_Q^2} \coth \left(\frac{\beta\Omega_Q}{2} \right) \\ [G_n^0(\Omega)]_{AB} &= \sum_Q \phi_n^2(Q) \left(\frac{DJ}{\Omega_Q} \right)^2 [\gamma_Q^2] \frac{\Omega_Q}{\Omega^2 - 4\Omega_Q^2} \coth \left(\frac{\beta\Omega_Q}{2} \right) = [G_n^0(\Omega)]_{BA} \end{aligned} \quad (2.10)$$

Adding these four matrix elements allows for all possibilities regarding positions of \mathbf{r} and \mathbf{r}' , and imaginary part of the sum yields the non-interacting limit of the two-magnon Raman scattering intensity.

$$R_n^0(\Omega) = \sum_Q \phi_n^2(Q) \left(\frac{DJ}{\Omega_Q} \right)^2 \delta(\Omega - 2\Omega_Q) \coth \left(\frac{\beta\Omega_Q}{2} \right) \frac{1}{1 - e^{-\beta\Omega}} \quad (2.11)$$

which is essentially the joint magnon density of states near the upper end of the magnon spectrum where $\Omega_Q \sim DJ$, and peaks at $\Omega = 2DJ$. Finite temperature corrections are negligible at temperatures $k_B T \ll J$. So the expression reduces to,

$$R_n^0(\Omega) = \sum_Q \phi_n^2(Q) \left(\frac{DJ}{\Omega_Q} \right)^2 \delta(\Omega - 2\Omega_Q) \quad (2.12)$$

We now turn to the magnon-interaction vertex within the Hubbard model, and obtain its fermionic structure at the lowest order level $O(1/\mathcal{N})$. The magnon-interaction vertex is evaluated in the large- U limit, wherein we only retain terms of order t^2/U^2 and neglect terms of order t^4/U^4 and smaller. $t^4/U^4 \sim J^2/U^2$ is a measure of the next-nearest-neighbour (NNN) spin-spin interaction within the equivalent extended-range Heisenberg model, and $O(J^2/U^2)$ terms will be included in the intermediate- U regime. The fermionic structure of the magnon interaction vertex, when the interacting magnons are on opposite sublattices, is shown in Fig. (2.1). There are 8 diagrams which contribute at the $O(1/\mathcal{N})$ level to the magnon interaction vertex. These diagrams essentially describe various \uparrow -spin and \downarrow -spin particle-hole processes involving the nearest neighbouring sites. The $+/-$ signs in these diagrams refers to the advanced/retarded nature of the one-particle Green's function, corresponding to states in the upper/lower Hubbard bands. The fermionic propagator signs indicated in the diagrams are not exhaustive of all possibilities, but correspond to choices which yield leading-order contribution at the t^2/U^2 level. The contributions of diagrams shown in Fig. 2.1 (a) - (h) are given in Table 2.1, and detailed evaluation of one of the diagrams is given in the Appendix A. Upto order t^2/U^2 the net contribution of all diagrams of $O(1/\mathcal{N})$ to the magnon interaction vertex is given by,

$$V_{\text{int}}(Q - Q', \Omega_1 - \Omega_2) = -2DJ\gamma_{Q-Q'} \quad (2.13)$$

implying nearest-neighbour, instantaneous interaction energy $-J$ between magnons. In the magnon-interaction vertex the entering and exiting magnon lines involve the same sublattice, and in fact the same site in large- U limit, so that in real space we can write

$$V_{\text{int}}(\mathbf{r}, \mathbf{r}', \mathbf{r} + \hat{\delta}, \mathbf{r}' + \hat{\delta}') = V_{\text{int}}(\mathbf{r}, \mathbf{r}, \mathbf{r} + \hat{\delta}, \mathbf{r} + \hat{\delta}) = -J$$

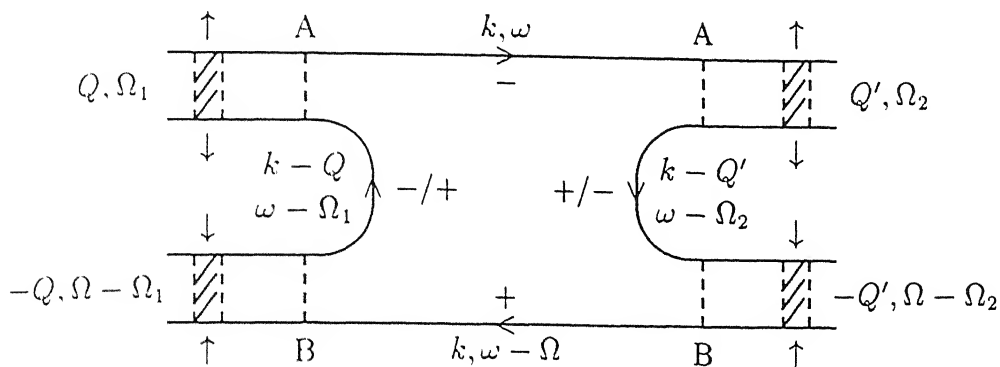
Therefore in the two sublattice basis the magnon-interaction vertex is diagonal:

$$[V_{\text{int}}(Q - Q')]_{\mu\nu} = -ZJ\gamma_{Q - Q'}\delta_{\mu\nu}$$

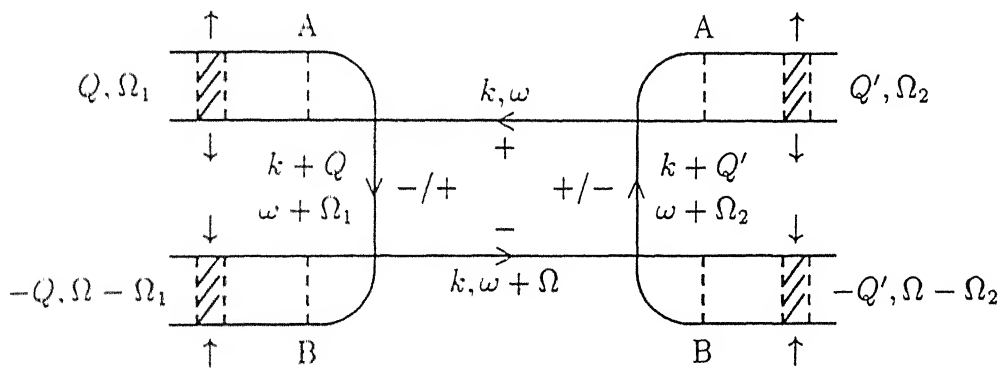
where $Z = 2D$ is the coordination number of the lattice. We also make use of the irreducible representations $\phi_n(Q)$ of the lattice to decouple the momentum dependence of the interaction vertex as,

$$V_{\text{int}}(Q - Q') = -zJ\gamma_{Q - Q'} = -J \sum_n \phi_n(Q)\phi_n(Q') \quad (2.14)$$

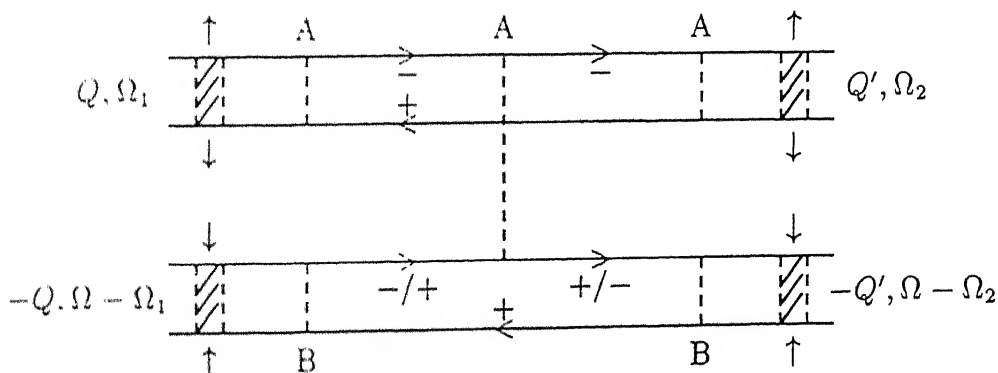
Here the irreducible representations $\phi_n(Q)$ are normalized so that $\sum_Q \phi_n^2(Q) = 1$ for all n .



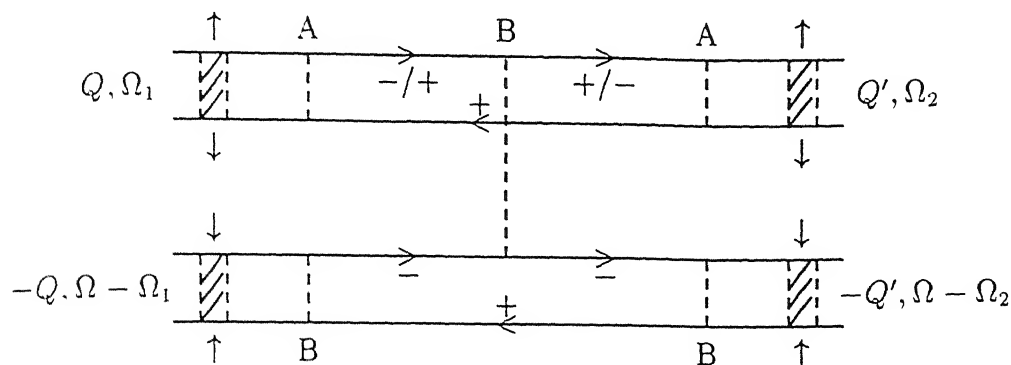
(a)



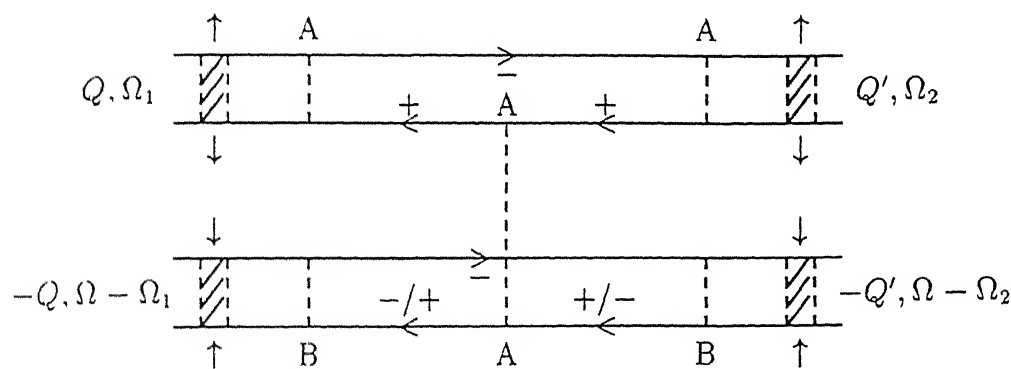
(b)



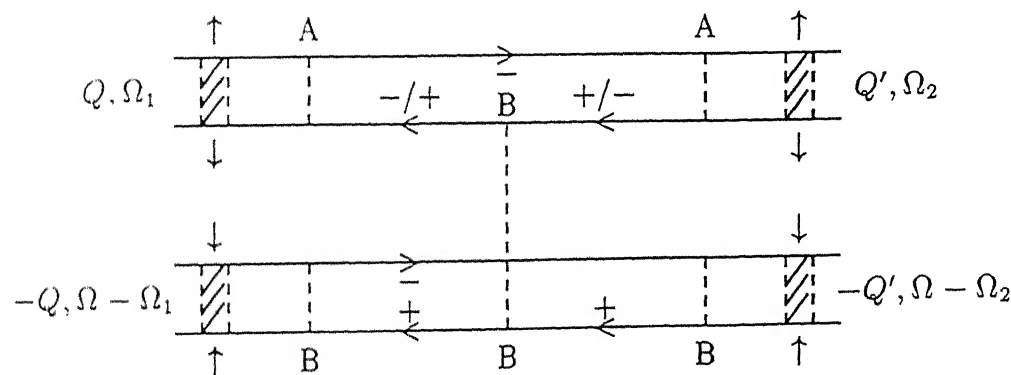
(c)



(d)



(e)



(f)

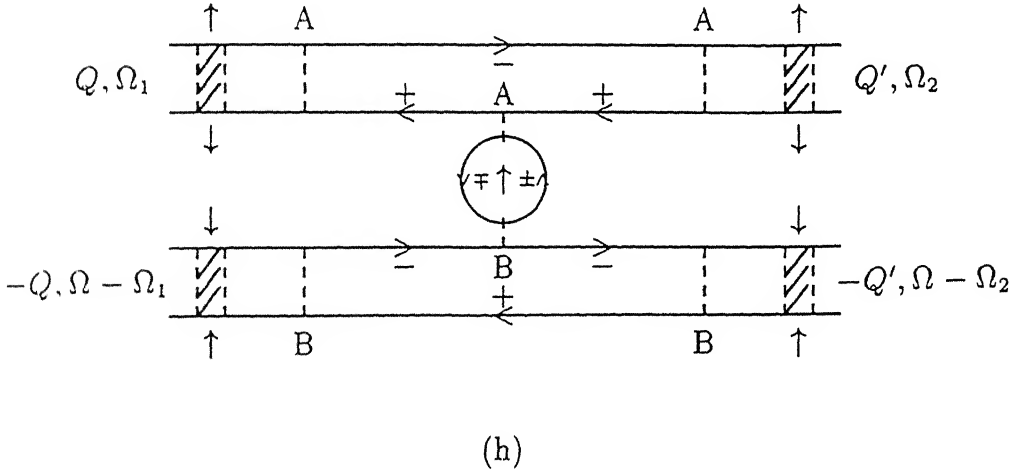
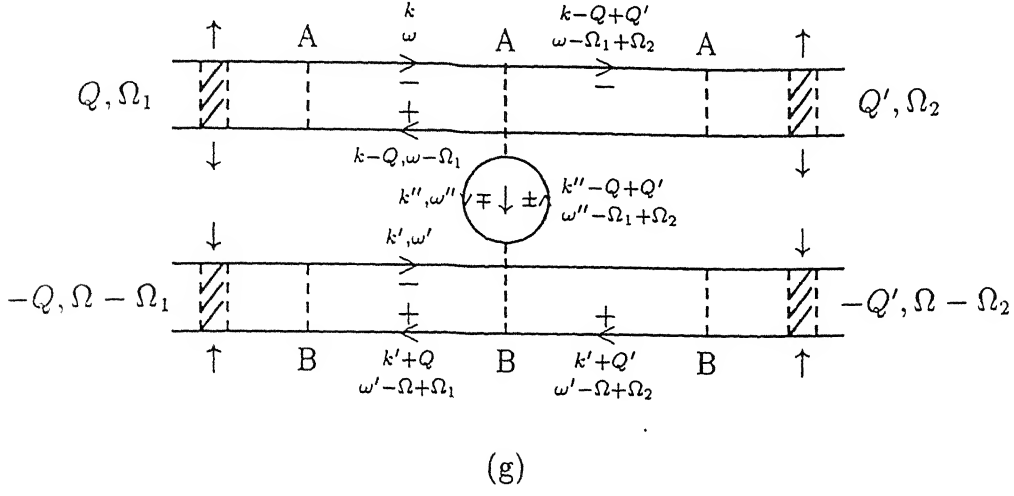


Figure 2.1: Fermionic structure of the diagrams contributing to the magnon interaction vertex at the order $1/N$ level and in the strong coupling limit. The interacting magnons are on A and B sublattice sites. The interaction vertices lie within the four wavy lines representing the Hubbard interaction. The hatched areas represent magnon propagators.

Table 2.1: Contributions to the magnon interaction vertex of diagrams shown in Fig. 2.1 (a)-(h), for various signs of the pair of fermion propagators which are off-diagonal in sublattice basis. The fermion-propagator signs refer to the advanced/retarded nature of the fermionic propagators.

Diagrams	Fermion-propagator signs	Contribution
Fig. 2.1(a),(b)	(++), (--)	$(JD/2)\gamma_{Q-Q'}$
Fig. 2.1(a),(b)	(+-), (-+)	$-2(JD/2)\gamma_{Q-Q'}$
Fig. 2.1(c),(d)	(--)	$(JD/2)\gamma_{Q-Q'}$
Fig. 2.1(c),(d)	(+-), (-+)	$-(JD/2)\gamma_{Q-Q'}$
Fig. 2.1(e),(f)	(++)	$(JD/2)\gamma_{Q-Q'}$
Fig. 2.1(e),(f)	(+-), (-+)	$-(JD/2)\gamma_{Q-Q'}$
Fig. 2.1(g),(h)	(+-), (-+)	$(JD/2)\gamma_{Q-Q'}$

This decoupling permits a straightforward summation of the perturbation series for the two-magnon propagator $[G_n(\Omega)]$ involving repeated magnon interactions in a ladder sum. The orthogonality of the irreducible representations $\phi_n(Q)$ leads to the following result in the two sublattice basis.

$$[G_n(\Omega)] = \frac{[G_n^0(\Omega)]}{1 + J[G_n^0(\Omega)]} \quad (2.15)$$

Again we need to add the four matrix elements of $[G_n(\Omega)]$ so as to allow for all possibilities regarding positions of \mathbf{r} and \mathbf{r}' . If we use $A(\Omega)$, $B(\Omega)$ and $C(\Omega)$ to denote the matrix elements $[G_n^0(\Omega)]_{AA}$, $[G_n^0(\Omega)]_{BB}$ and $[G_n^0(\Omega)]_{AB/BA}$ respectively which are given in Eq. (2.10), then the sum of matrix elements of $[G_n(\Omega)]$ is obtained as below. The imaginary part then yields $R_n(\Omega)$, the two-magnon Raman scattering intensity for a Hubbard antiferromagnet, in the strong coupling limit, at the ladder-sum level.

$$\sum_{\mu\nu} [G_n(\Omega)]_{\mu\nu} = \frac{(A + B + 2C) + 2J(AB - C^2)}{(1 + JA)(1 + JB) - J^2C^2} \quad (2.16)$$

Within the Heisenberg formalism, using a perturbative approach in which magnon-magnon interaction was taken into account in a ladder approximation, this result has been

obtained earlier by Solyom.[17] In this work four vertex functions were introduced corresponding to the four possibilities arising from the incoming and outgoing magnon lines belonging to the two sublattices. These vertex functions were obtained, within the ladder approximation, in the form of coupled equations, which were then solved and added to yield $\sum_{\mu\nu}[G_n(\Omega)]_{\mu\nu}$. On the other hand, by expressing the two-magnon propagator in the two-sublattice basis as 2×2 matrix, we are able to perform the ladder sum in a very straightforward manner, and summing the matrix elements *at the end* yields the same result. Of course our starting point is the Hubbard model, and we have treated the Hubbard interaction term perturbatively within a formally weak-coupling expansion scheme, and carrying this expansion to the strong coupling limit we have recovered the Solyom result. Our approach can therefore be extended to the intermediate- U and small- U regimes as well in principle.

Finally we consider the Ising limit of the expression for the two-magnon propagator given in Eq. (2.16), in order to clearly see the role of the nearest-neighbour magnon interaction. In the Ising limit when the spins can only be flipped completely, the spin-wave (spin-flip) energy is DJ , $\gamma_Q = 0$ and therefore $A = C = 0$ and $B = \sum_Q \phi_n^2(Q) (\frac{1}{\Omega-2DJ} - \frac{1}{\Omega+2DJ}) = (\frac{1}{\Omega-2DJ} - \frac{1}{\Omega+2DJ})$. In this limit $\sum_{\mu\nu}[G_n(\Omega)]_{\mu\nu}$ reduces to the following equation which shows the pole at $\Omega = 2DJ - J$ corresponding to the two-magnon spin-flip excitations created on nearest-neighbour sites:

$$\sum_{\mu\nu}[G_n(\Omega)]_{\mu\nu}|_{\text{Ising}} = \frac{1}{\Omega - 2DJ + J} \quad (2.17)$$

Several extensions of this analysis of two-magnon Raman scattering in the Hubbard model, carried out here in the large- U limit, are possible, some of which are discussed below. Higher-order corrections in the inverse-degeneracy expansion in powers of $1/\mathcal{N}$ may be included in the magnon-interaction vertex. Magnon damping which may be systematically incorporated in the theory in this manner is of particular interest because, after all, one magnon states are not exact eigenstates of the antiferromagnet, and hence damping of magnon modes is expected, particularly of the short-wavelength, high-energy modes. Also the one magnon lines themselves may be renormalized to include the magnon-interaction effects. At the $O(1/\mathcal{N})$ level the spin-wave energies are modified by the momentum-independent

multiplicative factor Z_c ($=1.16$ in $2D$ e.g.), and the spin-wave amplitude is reduced by the same factor as the sublattice magnetization relative to the HF value. Also of interest is the extension to the intermediate- U regime which is discussed below.

2.3 Extension of the calculation to Intermediate- U regime

As discussed in section II, in the intermediate- U regime the Hubbard model maps to an extended-range Heisenberg model and the NNN spin couplings of $O(t^4/U^3)$ can be obtained within the RPA analysis.[12] Alternatively the magnon-interaction vertices of Fig. (2.1) can be evaluated upto the next order, $O(t^4/U^4)$. Thus with the one-magnon propagator $\chi^{-+}(\Omega)$ and the magnon-interaction vertex both evaluated upto $O(t^4/U^4)$, one can systematically study the two-magnon Raman scattering in the intermediate- U regime. As mentioned earlier this regime is of interest because the modification of spin-wave spectrum results in a significantly different form of the magnon density of states. Instead of the divergence at energy $2J$ in DOS due to zone-boundary magnons, one instead gets a peak structure with a progressively increasing broadening as U/t decreases. This peak structure resembles the effect of magnon damping and therefore any quantitative treatment of two-magnon Raman scattering in the intermediate- U regime must take this intrinsic broadening into account. Here we consider a simple extension to the intermediate- U regime.

There are essentially two modifications that are required in our earlier analysis. Both the NN magnon-interaction energy and the spin-wave propagator acquire an order t^2/U^2 correction. Using results of reference [12] where spin-wave properties were obtained via a systematic expansion in powers of t^2/U^2 , we obtain after a zero-temperature evaluation of the two-magnon propagator the following matrix elements of $[G_n^0(\Omega)]$, the zeroth order two-magnon propagator, given in Eq. (2.10),

$$A(\Omega) = \sum_Q m^2 \phi_n^2(Q) \left(\frac{2J}{\Omega_Q} \right)^2 \left[a^2 - \left(\frac{\Omega_Q}{2J} \right)^2 - a \frac{\Omega}{2J} + \frac{1}{2} \left(\frac{\Omega}{2J} \right)^2 \right] \frac{\Omega_Q}{\Omega^2 - 4\Omega_Q^2}$$

$$\begin{aligned}
B(\Omega) &= \sum_Q m^2 \phi_n^2(Q) \left(\frac{2J}{\Omega_Q} \right)^2 \left[a^2 - \left(\frac{\Omega_Q}{2J} \right)^2 + a \frac{\Omega}{2J} + \frac{1}{2} \left(\frac{\Omega}{2J} \right)^2 \right] \frac{\Omega_Q}{\Omega^2 - 4\Omega_Q^2} \\
C(\Omega) &= \sum_Q m^2 \phi_n^2(Q) \left(\frac{2J}{\Omega_Q} \right)^2 [b^2 \gamma_Q^2] \frac{\Omega_Q}{\Omega^2 - 4\Omega_Q^2}
\end{aligned} \tag{2.18}$$

where $m = 1 - 2t^2/\Delta^2$ is the magnetization at the HF level, $2\Delta = mU$ is the Hubbard gap, and upto order t^2/Δ^2 we have the following results in the intermediate- U regime:

$$\begin{aligned}
\Omega_Q &= 2J \left[(1 - \gamma_Q^2) - \frac{t^2}{\Delta^2} (6 + 3 \cos Q_x \cos Q_y - 9\gamma_Q^2) \right]^{1/2} \\
a &= 1 - \frac{t^2}{\Delta^2} \left(3 + \frac{3}{2} \cos Q_x \cos Q_y + \gamma_Q^2 \right) \\
b &= 1 - \frac{t^2}{\Delta^2} \left(\frac{11}{2} \right)
\end{aligned} \tag{2.19}$$

A simple estimate for the NN magnon-interaction energy is now made as follows. We have seen that in the large- U limit, this interaction energy is nothing but the NN spin interaction energy. Since this result is consistent with the simple bond counting argument, we expect this to hold in the intermediate- U regime as well. Therefore we take the NN magnon interaction energy to be simply the modified NN spin interaction energy. An elementary quantitative analysis which relies on a comparison of spin-wave energy forms for the intermediate- U Hubbard model (evaluated upto order t^2/Δ^2) and the NNN Heisenberg model is given in Appendix B and yields for the NN spin interaction energy: $J_{NN} = J \left(1 - \frac{9}{2} \frac{t^2}{\Delta^2} \right)$.

The two-magnon Raman scattering intensity for the two-dimensional system is now evaluated in the intermediate- U regime from $G_n(\Omega) = G_n^0(\Omega)/[1 + J_{NN}G_n^0(\Omega)]$ and is shown in Fig. (2.2) for the case $\Delta/t = 3.5$ which corresponds to $U \sim B$ for the two-dimensional case where B denotes the bandwidth. We have taken the the symmetry factor as,

$$\phi_n(Q) = (\cos Q_x - \cos Q_y),$$

appropriate to the B_{1g} scattering geometry. We make a comparison with the large- U ($\Delta/t = 100$) limit result and it is clear that while there is a 25% increase in the linewidth in going to the intermediate U , this increase is not sufficient to account for the zero-temperature linewidth

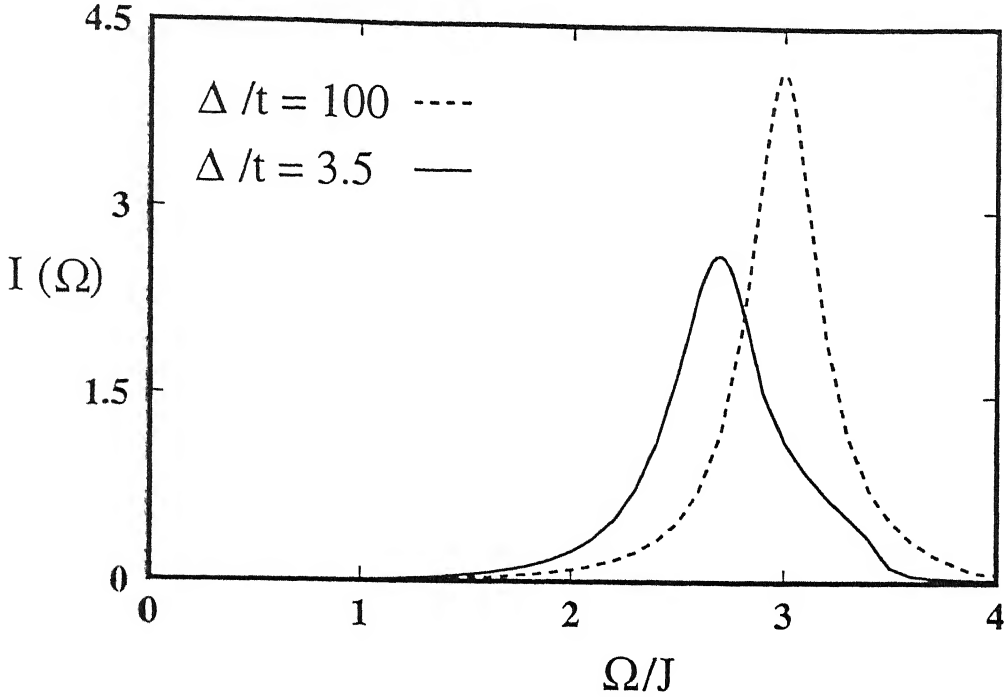


Figure 2.2: Calculated two-magnon Raman scattering intensity in the B_{1g} symmetry in the large- U limit (dashed) and intermediate- U limit (solid).

observed in La_2CuO_4 . Therefore while this contribution must be taken into account in any quantitative analysis, the large broadening seen in La_2CuO_4 must find an explanation elsewhere. In the following we consider an important source of broadening which is particularly relevant for La_2CuO_4 which is a low-spin and low-dimensional system.

2.4 Zero-temperature magnon damping

It is well established now that quantum spin fluctuations play an important role in La_2CuO_4 and other cuprate antiferromagnets which are spin $1/2$ and almost two-dimensional systems. There is a substantial reduction in the zero-temperature sublattice magnetization relative to the HF (Néel) value. Thus while long-range AF order is maintained in the $2D$ antiferromagnet, there is substantial amount of spin disorder. A consequence of this fluctuation-induced disorder is that spin-wave states are not exact eigenstates of the antiferromagnetic ground state, so that spin-wave or magnon damping must necessarily be present. And since two-magnon Raman scattering is related to the imaginary part of the two-magnon propagator,

magnon damping should play an important role in the observed broadening.

While finite-temperature magnon damping in the Heisenberg antiferromagnet has been studied in detail,[18–20] zero-temperature magnon damping is not easy to obtain in the antiferromagnetic insulator. The second-order magnon interaction process does not yield any damping at zero temperature owing to phase-space restriction. This process involves a magnon decaying into three magnons which subsequently reunite. From simple energy-momentum conservation considerations it is seen that for light-like linear dispersion this process has a vanishingly small phase space. This argument in fact holds for any convex energy-momentum dispersion, as for magnons.

We discuss below a simple estimate for zero-temperature magnon damping which is based on the following disorder analogy. Because of the substantial transverse spin fluctuations present in the $S = 1/2$, $D = 2$ antiferromagnetic insulator, magnons propagating in the system will see a fairly disordered magnetic lattice in which the spins, while maintaining overall AF long-range order, are slowly fluctuating in space and time. These fluctuations are slow on the time scale of $(2J)^{-1}$ and therefore zone-boundary, high-energy magnons of energy $2J$, which are of interest, will see an essentially static disorder. This disorder-analogy picture suggests that magnon damping will be proportional to the magnon density of states, which results in a qualitatively correct picture — substantial damping for zone-boundary magnons and very small damping for low-energy, long-wavelength magnons. Since we are interested only in the zone-boundary magnons, in view of the divergent magnon density of states at the upper edge at $2J$, a self-consistent evaluation of damping is therefore essential. We obtain the self-consistent magnon damping for zone-boundary magnons with energy $\Omega \sim 2J$ as given below:

$$\begin{aligned}\Gamma &= \gamma \operatorname{Im} \sum_Q [\chi^{-+}(Q, \Omega)] \\ &= \gamma \sum_Q \frac{2J}{\Omega_Q} \frac{\Gamma}{(\Omega - \Omega_Q)^2 + \Gamma^2}\end{aligned}\quad (2.20)$$

where γ is an effective disorder strength which measures the degree of spin disorder due to quantum transverse fluctuations, which we now proceed to estimate. An appropriate measure

of transverse spin fluctuations is the equal-time correlation function $\langle S^- S^+ \rangle$, and therefore the simplest estimate for the scattering vertex is $J\langle S^- S^+ \rangle$. And since the disorder strength γ represents two scattering processes, we obtain $\gamma \sim J^2 \langle S^- S^+ \rangle^2$. Now for the $D = 2$, $S = 1/2$ antiferromagnet, we know $\langle S^- S^+ \rangle = \sum_Q (1/\sqrt{1 - \gamma_Q^2}) - 1)/2 \approx 0.2$, which is precisely the quantum-fluctuation reduction in $\langle S_z \rangle$ or the sublattice magnetization.

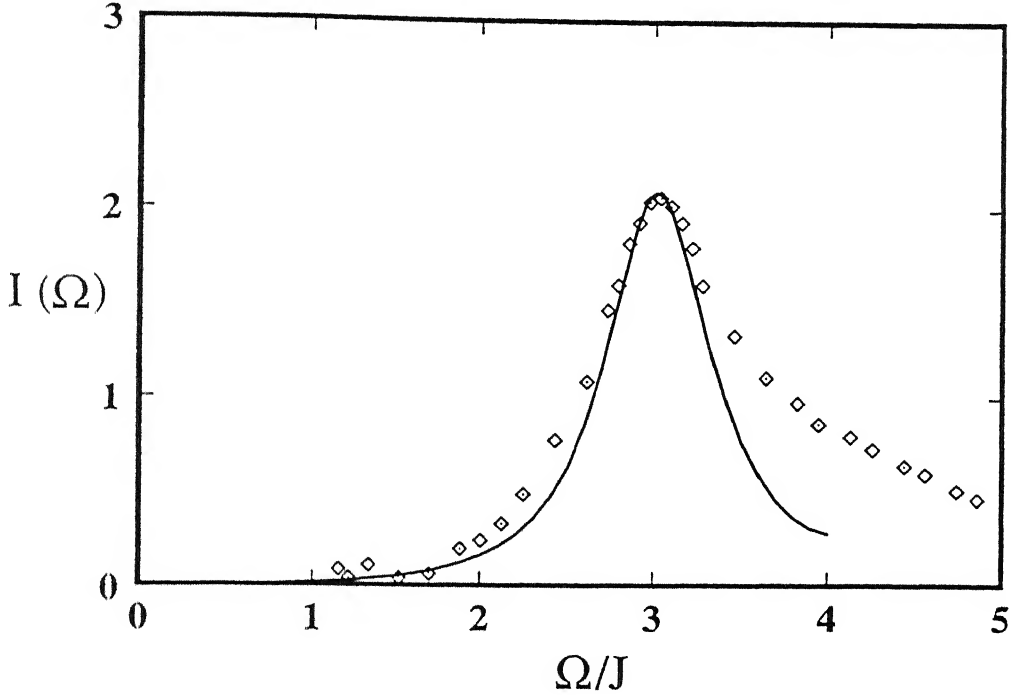


Figure 2.3: Calculated two-magnon Raman scattering intensity in the B_{1g} symmetry with a magnon damping of $\Gamma/J = 0.15$, and few points from the observed Raman scattering in La_2CuO_4 [taken from ref. 8].

Substituting this value of γ , the effective disorder strength, we self-consistently solve from Eq. (2.20) the effective one-magnon damping for zone-boundary magnons, and obtain $\Gamma/J = 0.15$. Thus even for zone-boundary magnons the resulting damping is small — only about 7% of the energy. We now incorporate this magnon damping arising from quantum spin fluctuations into the two-magnon Raman scattering evaluation from Eq. (2.16) in the large- U limit. This is done by simply adding the imaginary part $2i\Gamma$ to the two-magnon energy $2\Omega_Q$ in the energy denominators in Eq. (2.10). We take the symmetry factor $\phi_n(Q) = (\cos Q_x - \cos Q_y)$, appropriate to the B_{1g} symmetry, for comparison with Raman scattering observations

on La_2CuO_4 . The result of this evaluation, together with the Raman intensity observed in La_2CuO_4 taken from reference 8 is shown in Fig. (2.3). We adjust the energy scales so that the observed Raman peak at around 3200 cm^{-1} occurs at $3J$ where our calculated Raman scattering intensity peaks. As we have shown earlier, there will be additional broadening if the evaluation is done in the intermediate- U regime, appropriate to the cuprates. It is clear that while the linewidth compares reasonably well with the observed FWHM of about 1200 cm^{-1} , there is a marked asymmetry in the observed Raman line, and also a significantly larger scattering persisting at energies above $4J$. It has been suggested that four-magnon excitations are responsible for these features.

Appendix A

In this Appendix we discuss evaluation of diagrams shown in Fig. (2.1) (a)-(h) representing magnon interaction vertices relevant for the two-magnon propagator. The vertices are shown for interaction between magnons on opposite sublattices A and B. The evaluation is performed in the strong coupling limit in which case the interaction is actually effective only on nearest-neighbour sites. As mentioned earlier the interaction vertices represent spin- \uparrow , spin- \downarrow particle-hole processes in which energy-momentum is exchanged by the interacting magnons. All diagrams shown are of order $1/\mathcal{N}$ in an inverse-degeneracy expansion.

In each diagram there are precisely two fermionic lines connecting an A-sublattice site to a B sublattice site, and therefore off-diagonal in the two-sublattice basis. This pair of lines already contributes a factor t^2/U^2 , and therefore we need to retain only the leading order contributions from all other terms in each diagram. As a representative example, we discuss the evaluation of the diagram shown in Fig. 2.1 (g), where the fermion lines constituting the loop are off-diagonal in sublattice basis. The amplitudes of all other Green's functions are taken to be 1 and poles at energy $E_k^\pm = \pm U/2$, in order to obtain the leading-order contribution. Contributions of all diagrams shown in Fig. 2.1 (a)-(h) are given in Table 2.1. To the magnon interaction vertex the contribution of diagram shown in Fig. 2.1 (g) is given by:

$$\begin{aligned}
& V_{\text{int}}(Q = Q', \Omega_1 = \Omega_2)|_{(g)} \\
&= i(iU')^6 \int \frac{d\Omega}{2\pi} \sum_{\mathbf{k}} G_{\uparrow}^-(\mathbf{k}, \Omega)_{AA} G_{\uparrow}^-(\mathbf{k} - Q + Q', \Omega - \Omega_1 + \Omega_2)_{AA} G_{\downarrow}^+(\mathbf{k} - Q, \Omega - \Omega_1)_{AA} \\
&\quad \int \frac{d\Omega'}{2\pi} \sum_{\mathbf{k}'} G_{\downarrow}^-(\mathbf{k}', \Omega')_{BB} G_{\uparrow}^+(\mathbf{k}' + Q, \Omega' - \Omega + \Omega_1)_{BB} G_{\uparrow}^+(\mathbf{k}' + Q', \Omega' - \Omega + \Omega_2)_{BB} \\
&\quad (-1) \int \frac{d\Omega''}{2\pi} \sum_{\mathbf{k}''} G_{\uparrow}^{\mp}(\mathbf{k}'', \Omega'')_{AB} G_{\downarrow}^{\pm}(\mathbf{k}'' - Q + Q', \Omega'' - \Omega_1 + \Omega_2)_{BA} \\
&= (iU')^6 \int \frac{d\Omega}{2\pi i} \sum_{\mathbf{k}} \left(\frac{1}{\Omega - (-U/2) - i\eta} \right)^2 \left(\frac{1}{\Omega - U/2 + i\eta} \right)
\end{aligned}$$

$$\begin{aligned}
& \int \frac{d\Omega'}{2\pi i} \sum_{k'} \left(\frac{1}{\Omega - (-U/2) - i\eta} \right) \left(\frac{1}{\Omega - U/2 + i\eta} \right)^2 \\
& (-1) \int \frac{d\Omega''}{2\pi i} \sum_{k''} \left(\frac{\epsilon_{k''}/U}{\Omega'' - (\mp U/2) \mp i\eta} \right) \left(\frac{\epsilon_{k''} - Q + Q'/U}{\Omega'' - (\pm U/2) \pm i\eta} \right) \\
& = (tU')^6 \left(\frac{-1}{t'^2} \right) \left(\frac{1}{t'^2} \right) (-1) \left(\frac{-1}{U^3} \right) \sum_{k''} \epsilon_{k''} \epsilon_{k''} - Q + Q' \\
& = \frac{4t^2}{t'} \frac{D}{2} \gamma_Q - Q' = (JD/2) \gamma_Q - Q' \tag{2.21}
\end{aligned}$$

Appendix B

We discuss below an estimation of the NN spin interaction energy in the intermediate- U regime. The idea is to compare the spin-wave energy expressions obtained from (i) the spin-1/2 Heisenberg model with NNN spin interaction, and (ii) the intermediate- U Hubbard model, both for the two-dimensional, square-lattice case. If J and J' refer to the NN and NNN Heisenberg antiferromagnetic spin interactions, respectively, then for the spin-wave energy we have:

$$\Omega_Q \approx 2J[(1 - \gamma_Q^2) - (2J'/J)(1 - \gamma'_Q)]^{1/2} \quad (2.22)$$

where $\gamma'_Q \equiv \cos Q_x \cos Q_y$, and terms of order $(J'/J)^2$ have been neglected. We compare this expression now with the result for the Hubbard model obtained at the RPA level by an expansion[12] in powers of t^2/Δ^2 , where $2\Delta = mU$ is the Hubbard gap.

$$\Omega_Q = 2(4t^2/U)[(1 - \gamma_Q^2) - (t^2/\Delta^2)(6 + 3\gamma'_Q - 9\gamma_Q^2)]^{1/2} \quad (2.23)$$

which, after separating the γ_Q and γ'_Q pieces, can be rewritten as:

$$\Omega_Q \approx 2(4t^2/U)(1 - 9t^2/\Delta^2)^{1/2}[(1 - \gamma_Q^2) + (3t^2/\Delta^2)(1 - \gamma'_Q)]^{1/2} \quad (2.24)$$

Now comparing these two spin-wave energy expressions, we obtain for the NN spin coupling:

$$J \approx \frac{4t^2}{U} \left(1 - \frac{9}{2} \frac{t^2}{\Delta^2} \right) \quad (2.25)$$

and a *ferromagnetic* NNN spin coupling:

$$\frac{J'}{J} = -\frac{3}{2} \frac{t^2}{\Delta^2}. \quad (2.26)$$

Appendix C

In this appendix we present a list of the irreducible representations for the square lattice antiferromagnet which are relevant for our purpose,

$$\phi_1(Q) = \frac{1}{\sqrt{2}}(\cos Q_x - \cos Q_y) \quad (2.27)$$

$$\phi_2(Q) = \frac{1}{\sqrt{2}}(\cos Q_x + \cos Q_y) \quad (2.28)$$

$$\phi_3(Q) = \frac{1}{\sqrt{2}}(\sin Q_x - \sin Q_y) \quad (2.29)$$

$$\phi_4(Q) = \frac{1}{\sqrt{2}}(\sin Q_x + \sin Q_y) \quad (2.30)$$

$$(2.31)$$

Among these, the first two are appropriate to the B_{1g} and A_{1g} scattering geometry. Also the orthonormality property of these irreducible representations can be written as,

$$\sum_Q \phi_n^2(Q) = 1 \quad \text{for all } n$$

Bibliography

- [1] R. J. Elliott, M. F. Thorpe, G. F. Imbusch, R. Loudon, J. B. Parkinson, Phys. Rev. Lett. **21**, 147 (1968).
- [2] P. A. Fleury, Phys. Rev. Lett. **21**, 151 (1968).
- [3] M. F. Thorpe, J. Appl. Phys. **41**, 892 (1970).
- [4] J. B. Parkinson, J. Phys. C **2**, 2012 (1969).
- [5] P. A. Fleury and H. J. Guggenheim, Phys. Rev. Lett. **24**, 1346 (1970).
- [6] R. J. Elliott and M. F. Thorpe, J. Phys. C **2**, 1630 (1969).
- [7] K. Lyons, P. A. Fleury, J. P. Remeika, A. S. Cooper and T. J. Negran, Phys. Rev. B **37**, 2353 (1988).
- [8] R. R. P. Singh, P. A. Fleury, K. B. Lyons, and P. E. Sulewski, Phys. Rev. Lett. **62**, 2736 (1989).
- [9] P. E. Sulewski, P. A. Fleury, K. B. Lyons, S-W. Cheong and Z. Fisk, Phys. Rev. **41**, 225 (1990).
- [10] S. L. Cooper, D. Reznick, A. L. Kotz, M. A. Karlow, R. Liu, M. V. Klein, W. C. Lee, J. Giapintzakis, D. M. Ginzberg, B. W. Veal and A. P. Paulikas, Phys. Rev. B **47**, 8233 (1993).
- [11] B. S. Shastry and B. Shraiman, Int. J. Mod. Phys. B **5**, 365 (1991).

- [12] A. Singh, Phys. Rev. B **48**, 6668 (1993).
- [13] P. Sen and A. Singh, Phys. Rev. B **48**, 15792 (1993).
- [14] S. Basu and A. Singh, Phys. Rev. B **54**, 6356 (1996)
- [15] A. Singh, Phys. Rev. B **43**, 3617 (1991).
- [16] A. Singh and Z. Tešanović, Phys. Rev. B **41**, 614 (1990); *ibid.* **41**, 11457 (1990).
- [17] J. Solyom, Z. Physik, **243**, 382 (1971).
- [18] A. B. Harris, D. Kumar, B. I. Halperin, and P. C. Hohenberg, Phys. Rev. B **3**, 961 (1971).
- [19] S. Tye and B. I. Halperin, Phys. Rev. B **42**, 2096 (1990).
- [20] P. Kopietz, Phys. Rev. B **41**, 9228 (1990).
- [21] F. Nori, R. Merlin, S. Haas, A. W. Sandvik, and E. Dagotto, Phys. Rev. Lett. **75**, 553 (1995).
- [22] M. J. Massey, R. Merlin, and S. M. Girvin, Phys. Rev. Lett. **69**, 2299 (1992).
- [23] P. Knoll *et al.*, Phys. Rev. B **42**, 4842 (1990).
- [24] A. V. Chubokov and D. M. Frenkel, Phys. Rev. Lett. **74**, 3057 (1995); Phys. Rev. B **52**, 9760 (1995).

Chapter 3

Hopping Disorder and Asymmetric Magnon-Energy Renormalization in an Antiferromagnet

3.1 Introduction

We have seen in the last chapter that there remains a few anomalous features such as the large linewidth, significant asymmetry in the Raman lineshape and substantial intensity observed in the classically forbidden A_{1g} geometry could not be explained within the existing theoretical framework.[1-6] Several new ideas have been put recently to resolve these issues which include the exchange disorder caused by zero point lattice fluctuations,[7] and resonant Raman scattering in which the incident photon energy is comparable to the energy gap in cuprates[8].

When lattice distortions, caused by quantum and thermal fluctuations, are taken into account in the adiabatic or Born-Oppenheimer approximation, the hopping terms t_{ij} , and hence the exchange couplings J_{ij} , which depend upon the instantaneous position of ions, must therefore include random terms. This approximation should be valid for high-energy magnon excitations in cuprates where the magnon energies of order $2J \sim 2000\text{cm}^{-1}$ are much greater than the Debye energy $\hbar\omega_D \sim 340\text{cm}^{-1}$. The exchange disorder caused by zero-point lattice vibration was recently taken into account within a nearest-neighbor (NN) Heisenberg model where the exchange energy $J + \delta J_{ij}$ at each bond includes random terms.[7] For a

Gaussian distribution of the random terms, this model was studied using the Quantum Monte Carlo (QMC) technique and Raman intensities were obtained numerically in different scattering symmetries. Satisfactory fitting was obtained with the experimental Raman intensity lineshape for a Gaussian variance of $\sigma \sim 0.4$. However, no clear insight emerges from this QMC calculation regarding the explicit effects of exchange disorder on (i) low-energy, long-wavelength magnon modes, (ii) the magnon velocity, and (iii) the high-energy magnon modes with energy $\sim 2J$ which are mainly responsible for the Raman scattering. Ascertaining the exchange-disorder-induced renormalization of the magnon energy scale is of vital importance, however, as it is from comparison of this scale with experiments (such as neutron scattering, Raman scattering, magnetization versus temperature etc.) that a reliable value of J for the cuprates is extracted.

In this chapter we therefore examine these questions in the context of an antiferromagnet (AF) with off-diagonal disorder. We consider the following Hubbard Hamiltonian on a square lattice, with randomness in the hopping terms, and with a filling of one fermion per site, so that an antiferromagnetic insulating state is obtained. Generalization to three dimension and to other bipartite lattices is straightforward. Random terms δt_{ij} are included in NN hopping terms, and are chosen independently for each NN pair of sites from a Gaussian distribution,

$$\hat{H} = - \sum_{\langle ij \rangle, \sigma} (t + \delta t_{ij}) (\hat{a}_{i\sigma}^\dagger \hat{a}_{j\sigma} + \text{h.c.}) + U \sum_i \hat{n}_{i\uparrow} \hat{n}_{i\downarrow}, \quad (3.1)$$

$$P(\delta t_{ij}/t) = \frac{1}{\sqrt{2\pi}\sigma} \exp \left[-\frac{(\delta t_{ij}/t)^2}{2\sigma} \right]. \quad (3.2)$$

The distribution width $\sqrt{\sigma}$ measures the disorder in hopping. Since for weak disorder $\delta J_{ij}/J \sim 2\delta t_{ij}/t$, therefore the distribution widths $\sqrt{\sigma_J}$ and $\sqrt{\sigma_t}$ for random exchange-energy terms and hopping terms should be related via $\sigma_J = 4\sigma_t$. An estimate for σ_J has been obtained[7] using $\sigma_J = (\partial \ln J / \partial r) (\langle \delta r \rangle / r)$, where the relative amplitude of the zero-point motion $\langle \delta r \rangle / r$ was estimated as about 5%. The dependence of the exchange energy J on the in-plane Cu-Cu distance r is taken to be of the form $J \sim r^{-\alpha}$. The exponent α for cuprates

has been obtained using high-pressure studies[9] in the range $\alpha = 4 \pm 2$, whereas a stronger dependence ($\alpha = 6.8 \pm 0.8$) has been reported by others.[10] In their QMC calculations Nori *et al.* have considered the cases $\sigma_J = 0.3, 0.4$ and 0.5 .

We have examined — both perturbatively and numerically — effects of hopping disorder on magnon energies, their wavefunctions, and on the density of states (DOS). In both schemes the magnon modes are obtained at the level of Random Phase Approximation (RPA). At this level the magnon propagator has the form $[\chi^{-+}(\omega)] = [\chi^0(\omega)]/1 - U[\chi^0(\omega)]$, where $[\chi^0(\omega)]$ is the zeroth-order antiparallel-spin particle-hole propagator evaluated in the broken-symmetry AF state. Eigensolutions of the $[\chi^0(\omega)]$ matrix yield the magnon energies and wavefunctions. In the perturbative analysis we obtain the disorder-induced perturbation to $[\chi^0(\omega)]$, and obtain resulting corrections to its eigenvalues, which then yield the renormalized magnon energies. For analytical convenience we have considered the strong-correlation limit as the perturbative analysis is particularly simple in this limit. We have also numerically obtained $[\chi^0(\omega)]$ using the self-consistent eigenstates of the HF Hamiltonian in the AF state with the random hopping terms included from the beginning. This method can be applied for arbitrary interaction strength U/t .

We find that there is strong renormalization in energy of high-energy magnon modes due to a cooperative effect arising from local correlations in hopping disorder, which results in appreciable magnon DOS well above the maximum energy $2J$ for the pure system, even for σ_J as small as 0.1 . This result is significant because it not only clearly shows how the two-magnon Raman scattering intensity, which involves the one-magnon DOS, can extend well beyond the energy $4J$ when hopping disorder is present, but it also yields an insight into why Raman scattering is so sensitive to the tiny zero-point fluctuations. We also show that these high-energy magnon modes at the upper end of the spectrum are strongly localized in regions of the lattice where the locally-averaged hopping strength is maximum, i.e. at sites where all δt_{ij} 's connecting to the site have maximum average. We have also obtained the energy renormalization of the low-energy, long-wavelength modes, both to first order and second order in $\delta t_{ij}/t$. We find that the first-order correction to magnon energies are of the random-walk type, which decrease like $1/\sqrt{N}$ with increasing system size, but can be significant

for finite-size lattices. The second-order correction, on configuration averaging, yields a momentum-independent multiplicative renormalization of the magnon energy by a factor $1 + \sigma$, i.e. $\omega_q = 2J(1 + \sigma)\sqrt{1 - \gamma_q^2}$. Thus the Goldstone mode is preserved, and the low-energy, long-wavelength magnons are weakly perturbed by off-diagonal, hopping disorder. This is in contrast to the case of potential scattering (diagonal disorder) where in two dimensions singular corrections to low-energy magnon modes were obtained[11].

3.2 Perturbative Analysis

To obtain the magnon energies and wavefunctions, we evaluate the transverse spin fluctuation (magnon) propagator $\chi^{-+}(rt, r't') \equiv \langle AF | S^-(rt) S^+(r't') | AF \rangle$ which, at the RPA level, is given by $[\chi^0(\omega)]/1 - U[\chi^0(\omega)]$ after Fourier transformation to frequency space. Here $[\chi^0(\omega)]$ is the antiparallel-spin particle-hole propagator evaluated in the broken-symmetry, self-consistent state, with matrix elements given by, $[\chi^0(\omega)]_{ij} = i \int (d\omega'/2\pi) G_{ij}^\uparrow(\omega') G_{ji}^\downarrow(\omega' - \omega)$. The magnon energies are then given by the poles in the magnon propagator, $1 - U\lambda(\omega) = 0$, where $\lambda(\omega)$ is the eigenvalue of the $[\chi^0(\omega)]$ matrix.

In the perturbative technique, the disorder-induced perturbation $[\delta\chi^0]$ to the $[\chi^0(\omega)]$ matrix is obtained diagrammatically in powers of $\delta t_{ij}/t$. Resulting corrections to the eigenvalues of $[\chi^0(\omega)]$ then yield the renormalization in magnon energies. Diagrams which contribute to $[\delta\chi^0]$ to first order in δt_{ij} are shown in Fig. 3.1 (a). The upper and lower lines are respectively the \uparrow -spin and \downarrow -spin propagators with frequencies ω' and $\omega' - \omega$. In the diagonal matrix element $[\delta\chi^0]_{ii}$, k is summed over all NN sites of i . Other diagrams are obtained by exchanging the i and k vertices of the dashed line and by putting the dashed line in the lower (\downarrow -spin) propagator etc. In the strong-correlation limit we obtain,

$$[\delta\chi^0]_{ii} = -\frac{t^2}{2\Delta^3} \sum_k \delta t_{ik}/t; \quad [\delta\chi^0]_{ij} = -\frac{t^2}{2\Delta^3} \delta t_{ij}/t. \quad (3.3)$$

where $2\Delta = mU$ is the Hubbard gap characterizing the AF insulating state, and only terms upto order (t^2/Δ^3) have been retained, appropriate to the strong-correlation limit. We notice that the sum of all the NN matrix elements $[\delta\chi^0]_{ij}$ is precisely the diagonal matrix element

$[\delta\chi^0]_{ii}$. An immediate consequence of this correlation is that the Goldstone mode is preserved and that generally the effective scattering of low-energy, long-wavelength modes is weak. To begin with we consider the first-order correction to the eigenvalue $\lambda(\omega)$ due to the perturbation $[\delta\chi^0]$. For this we require the eigensolutions of $[\chi^0(\omega)]$ in the pure AF state, which can be labeled by momentum due to translational symmetry within the two-sublattice basis. We first consider the case of low-energy, long-wavelength modes for which $q \ll 1$ and $\omega/2J \ll 1$. Up to order q^2 , $(\omega/2J)^2$ and in the strong-correlation limit, the eigenvector and eigenvalue of $[\chi^0(\omega)]$ for the pure AF are given by,[12]

$$\phi_q^{(0)}(r) = \frac{1}{\sqrt{N}} \begin{pmatrix} \sqrt{1 + \omega/2J} \\ -\sqrt{1 - \omega/2J} \end{pmatrix} e^{iq \cdot r} \quad (3.4)$$

$$\lambda_q^{(0)} = \frac{1}{U} - \frac{t^2}{\Delta^3} \left[\frac{q^2}{4} - \frac{1}{2} \left(\frac{\omega}{2J} \right)^2 \right]. \quad (3.5)$$

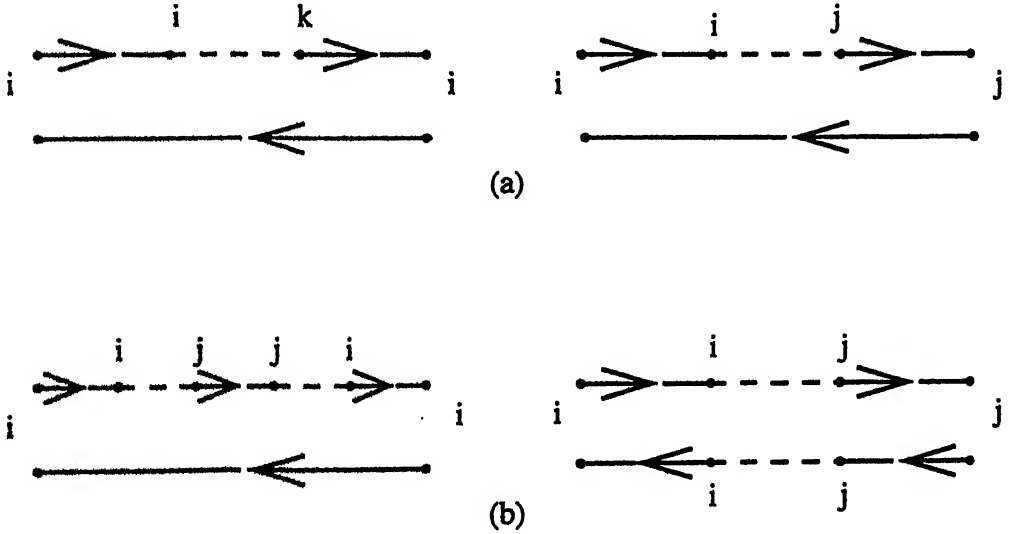


Figure 3.1: Diagrams contributing at the (a) first-order level in δt (dashed lines) and (b) second-order level to the diagonal matrix element $[\delta\chi^0]_{ii}$ and the nearest-neighbor matrix element $[\delta\chi^0]_{ij}$

Therefore for the first-order correction we obtain,

$$\delta\lambda_q^{(1)} = \langle \phi_q^{(0)} | [\delta\chi^0] | \phi_q^{(0)} \rangle = -\frac{1}{2} \frac{t^2}{\Delta^3} \left[(r_x + r_y) \left(\frac{\omega}{2J} \right)^2 + r_x q_x^2 + r_y q_y^2 \right], \quad (3.6)$$

$$\begin{aligned} \text{where} \quad r_x &\equiv \frac{1}{N} \sum_i \delta t_{ij}/t & (\vec{r}_j = \vec{r}_i + a\hat{x}) \\ \text{and} \quad r_y &\equiv \frac{1}{N} \sum_i \delta t_{ij}/t & (\vec{r}_j = \vec{r}_i + a\hat{y}) \end{aligned} \quad (3.7)$$

are the lattice averages of the random hopping terms δt_{ij} taken in the x and y directions respectively. Significantly the order ω terms cancel exactly for arbitrary distribution of δt_{ij} , and their cancellation follows from the fact that the A- and B-sublattice sums of the diagonal terms $[\delta\chi^0]_{ii}$ are identical, i.e. $\sum_{i \in A} [\delta\chi^0]_{ii} = \sum_{i \in B} [\delta\chi^0]_{ii}$.

Now, r_x and r_y will vanish for an infinite system if the random hopping terms δt_{ij} are distributed symmetrically about zero, and therefore in the infinite-size limit, there will be no first-order correction to long-wavelength magnon energies. However, for a finite-size system the averages r_x and r_y are like random-walk averages and will scale like $1/\sqrt{N}$. This is because the terms $\sum_i \delta t_{ij}/t$ in r_x and r_y are sums of N Gaussian random variables, and therefore will themselves have a Gaussian distribution of width $\sqrt{N}\sigma$.

Solving for ω from the equation, $1 - U(\lambda_q^{(0)} + \delta\lambda_q^{(1)}) = 0$ yields the renormalized magnon energies for long-wavelength modes:

$$\omega_q = \sqrt{2J[q_x^2(1 + 3r_x + r_y) + q_y^2(1 + 3r_y + r_x)]^{1/2}} \quad (3.8)$$

We now examine the effects of hopping disorder to first order on the high-energy magnon modes with energy $\approx 2J$. In the pure AF the maximum magnon energy is $2J$ and these magnon modes have non-zero amplitudes only on sites of one sublattice, corresponding to creating spin deviation on these sites. The energy cost due to a spin deviation of this kind is therefore $4(J/2) = 2J$, where $J/2$ is the bond strength and 4 is the number of broken bonds. Now, when hopping disorder is present the highest-energy magnon mode will correspond to creating a spin deviation on that site where the sum of the NN bonds is maximum. This

will clearly occur in a region of the lattice where the hopping disorder terms δt_{ij} neighboring a site have the maximum average. In fact, generally the high-energy magnon modes with energy $\geq 2J$ will be localized around such sites across the lattice.

Interestingly, in such regions where the locally averaged hopping is significantly higher than the bulk average t , the diminished U/t ratio leads to a lowering of the local staggered magnetization $m(r)$, and hence of the local charge gap $2\Delta(r) \equiv m(r)U$. Fig. (3.2) shows the magnetization $m(r)$ calculated for $\sigma = 0.1$ and $U/t = 10$ for a 10×10 system. As mentioned above we can see a local lowering of the charge gap at certain regions where the magnon wavefunction is found to have the maximum amplitude. Thus the localization of the high-energy magnon modes in such regions is suggestive of the high-energy magnons acquiring a charge due to hopping disorder and getting trapped in the local depressions of the charge gap. This can be seen formally by examining the self-energy correction, $\Sigma_{ij} = U^2 \delta \chi_{ij}^0$, to the magnon modes due to hopping disorder, particularly the diagonal terms which will act like potential terms for the magnons. From Eqn. (3.3) we obtain,

$$\Sigma_{ii} = -J \sum_{\delta} \frac{\delta t_{i,i+\delta}}{t}. \quad (3.9)$$

Now $\sum_{\delta} \delta t_{i,i+\delta}/t$ is the sum of z (coordination number) Gaussian variables and will therefore itself have a Gaussian distribution with an effective second moment of $Z\sigma$. Thus the local self-energy Σ_{ii} has a scale of J and is randomly distributed according to a Gaussian distribution with a much bigger width $\sqrt{Z\sigma}$. The high-energy magnons thus effectively experience a random potential and therefore get trapped in the local potential depressions. In fact, Σ_{ii} precisely yields the extra magnon energy for the localized high-energy modes, and therefore we can conclude that these modes will extend well beyond $2J$ in energy, and that the excess in energy will have a Gaussian distribution of width $\sqrt{Z\sigma}$. This result has a significant impact on the one-magnon density of states, indicating that there will be a Gaussian tail in the DOS extending well beyond energy $2J$. Indeed, this is evident from Fig. (3.3) showing the magnon DOS obtained numerically which is discussed in the following section.

We have thus shown that while the low-energy, long-wavelength magnon modes are very

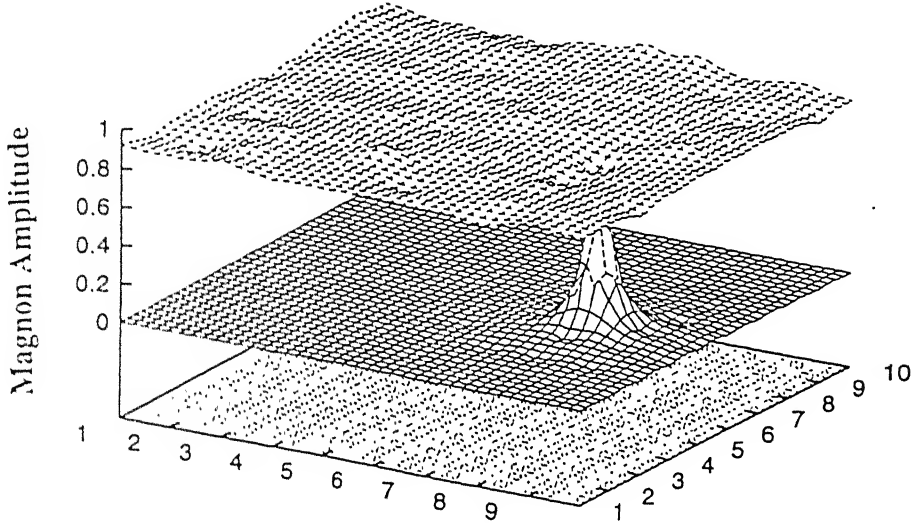


Figure 3.2: The amplitude for the highest magnon-mode (below) and the magnetization profile (top) obtained from numerically is shown for a 10×10 lattice for $U/t = 10$ in presence of disorder ($\sigma = 0.1$).

weakly affected by hopping disorder, on the other hand the high-energy magnon modes are strongly affected because of a cooperative effect due to local correlations in hopping disorder. There is therefore a strong asymmetry in the energy shifts of low-energy and high-energy magnon modes, which is also evident from the magnon DOS shown in Fig. (3.3). Now the asymmetric lineshape in the two-magnon Raman scattering in cuprate antiferromagnets has been a puzzling feature. If indeed it is the randomness in hopping due to zero-point motion which is responsible for this feature, then we have shown that this asymmetry is basically arising from the asymmetric energy renormalization of high-energy and low-energy magnons due to hopping disorder. Also, the strong energy renormalization of high-energy magnons due to this cooperative effect of hopping disorder leads to an insight into the extraordinary sensitivity of the Raman scattering process on zero-point motion of the lattice. This is the central result of this chapter.

We have seen that the first-order correction to $[\chi^0(\omega)]$ yields vanishing contribution to the

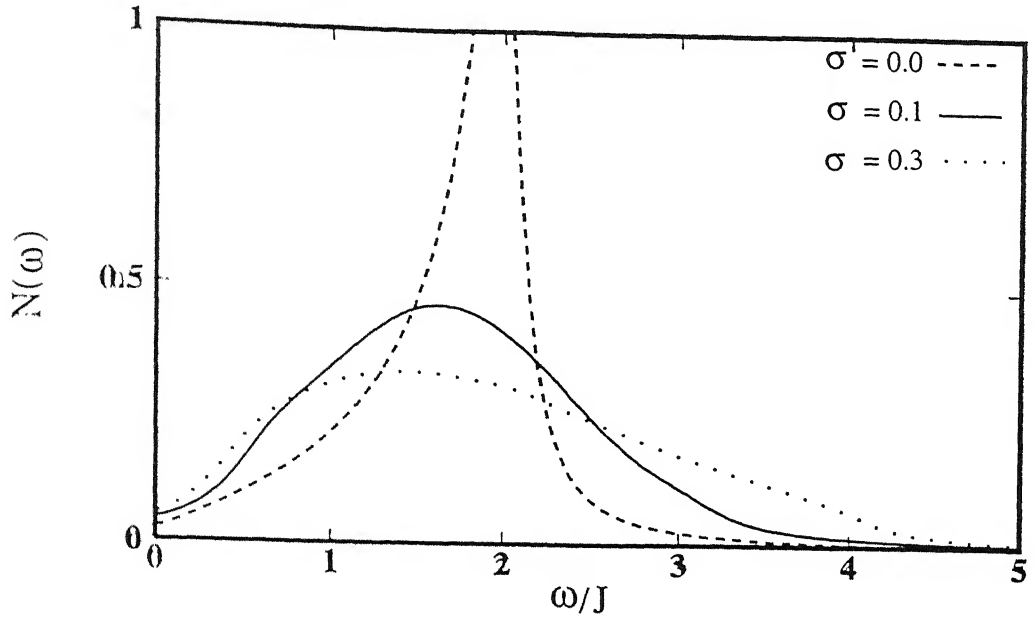


Figure 3.3: The configuration-averaged magnon density of states obtained numerically for a 10×10 hopping disordered system with $\sigma = 0.1$ and 0.3 , in the strong-correlation limit ($U/t = 10$).

low energy, long-wavelength magnon energies in the limit of infinite system size. Therefore it is necessary to consider second-order correction to $[\chi^0(\omega)]$, for which the relevant diagrams are shown in Fig. 3.1(b). Summing all the processes, we obtain after configuration averaging,

$$\begin{aligned} \langle \delta \chi_{ii}^0 \rangle &= -\frac{2t^2}{U^3} \sum_k \left\langle \left(\frac{\delta t_{ik}}{t} \right)^2 \right\rangle = -\frac{2Zt^2}{U^3} \sigma \\ \langle \delta \chi_{ij}^0 \rangle &= -\frac{2t^2}{U^3} \left\langle \left(\frac{\delta t_{ij}}{t} \right)^2 \right\rangle = -\frac{2t^2}{U^3} \sigma. \end{aligned} \quad (3.10)$$

After adding to $[\chi^0(\omega)]$, and Fourier transforming within the two-sublattice basis, we obtain,

$$[\chi^0(q, \omega)] = \frac{1}{U} \mathbf{1} - (1 + \sigma) \frac{t^2}{\Delta^3} \begin{bmatrix} 1 + \frac{\omega}{2J'} & \gamma_q \\ \gamma_q & 1 - \frac{\omega}{2J'} \end{bmatrix} \quad (3.11)$$

where $2J' \equiv 2J(1 + \sigma)$ is the renormalized magnon-energy scale. Therefore, all magnon energies are simply renormalized by a momentum-independent multiplicative factor $(1 + \sigma)$, and we have,

$$\omega_q = 2J(1 + \sigma)(1 - \gamma_q^2)^{1/2} \quad (3.12)$$

3.3 Numerical analysis

We now briefly describe a numerical method for obtaining the magnon energies and wave functions. Details of this method have been discussed earlier for the impurity-doped AF with on-site potential disorder.[13] The idea is to self-consistently obtain the AF state for the hopping-disordered system within the Hartree-Fock approximation, and then determine the magnon eigensolutions from the transverse spin propagator, evaluated in the broken-symmetry state. Since we are concerned here with an AF insulating state for the one-fermion-per-site system, the HF-plus-fluctuations approach is expected to be quantitatively accurate even in the strong correlation limit, as has been shown to be the case for the pure system.[14]

Within the HF approximation we construct the Hamiltonian matrix on a two-dimensional square lattice with periodic boundary conditions. The random hopping terms δt_{ij} are obtained for each pair of NN sites using a Gaussian random number generator. In the site basis matrix elements of the Hamiltonian for spin σ are given by $\langle i|\hat{H}_\sigma|i\rangle = U\langle n_{i\bar{\sigma}}\rangle$ and $\langle i|\hat{H}_\sigma|j\rangle = -t(\pm\delta t_{ij})$ if i and j are nearest neighbors. Starting with some initial configuration for the spin densities, the Hamiltonian matrix is constructed and diagonalized to yield the eigensolutions $\{E_{k\sigma}, \phi_{k\sigma}\}$. From these the spin densities are re-evaluated, the H-matrix is updated, and the procedure iterated until self-consistency is achieved. These eigenstates obtained numerically of the self consistent AF state are used to construct the $[\chi^0(\omega)]$ matrix as described earlier.[13]

It is convenient to express the transverse spin fluctuation propagator at RPA level in terms of the eigensolutions $\{\phi_\lambda(\omega), \lambda(\omega)\}$, of the $[\chi_0(\omega)]$ matrix:

$$[\chi^{-+}(\omega)] = \sum_{\lambda} \frac{|\phi_{\lambda}(\omega)\rangle\langle\phi_{\lambda}(\omega)|}{1 - U\lambda(\omega)}. \quad (3.13)$$

In this form we have a propagator representation for the magnon, with the magnon wavefunction given by the eigenvector $|\phi_{\lambda}(\omega)\rangle$ and magnon energies obtained from the pole, $1 - U\lambda(\omega) = 0$. The energy ω_n of the n -th magnon mode is obtained by solving, $1 - U\lambda_n(\omega_n) = 0$ for the appropriate (n -th from the top) eigenvalue $\lambda_n(\omega)$. The root of the equation, $\lambda_n(\omega_n) = 1/U$ is determined by obtaining $\lambda_n(\omega)$ for closely spaced values of ω on both

sides of the root, and finally linearly extrapolating between them. Suppose $(\lambda_n^1, \omega_n^1)$ and $(\lambda_n^2, \omega_n^2)$ are two sets of values for two energies very close to, and on either side of the root, then the root ω_n is determined from,

$$\lambda(\omega_n) = \frac{1}{t'} = \lambda_n^1 + \frac{\lambda_n^2 - \lambda_n^1}{\omega_n^2 - \omega_n^1}(\omega_n - \omega_1) \quad (3.14)$$

The whole procedure therefore involves obtaining the self-consistent state for a given realization of the hopping-disordered system, followed by constructing and diagonalizing the $[\chi^0](\omega)$ matrix, and finally from the set of eigenvalues $\lambda_n(\omega)$ the magnon energies are obtained by interpolation as described above. This scheme for obtaining the magnon energies is then repeated for several configurations.

We find that the highest magnon energies always extend well beyond the maximum energy $2J$ for the pure case. Even for σ as low as 0.1, the highest magnon energy obtained is 1.36 in units of t whereas $2J \sim 0.8$ in units of t (for $U/t = 10$). This is in agreement with the perturbative analysis finding that the high-energy magnon modes are strongly renormalized due to the correlated effect of hopping disorder.

In Table 3.1 we show the variation with σ of this hopping-disorder-induced increase in the magnon energy for the highest magnon magnon mode, and compare with the perturbative result derived earlier [Eqn. (3.9)]. For a given σ the highest magnon mode energy is configuration averaged over 25 configurations of the hopping-disordered system to yield $\bar{\omega}_m$. The difference with the maximum magnon energy $\dot{\omega}_m^0$ for the pure case yields the excess due to hopping disorder. This difference is compared with the perturbative result for the magnon self-energy given in Eqn. (3.9) for high-energy magnon modes with energy near $2J$. For a given realization of the random hopping terms, the nearest neighbour sum $\sum_\delta \delta t_{ij}/t$ is performed for all lattice sites, yielding the local self-energies σ_{ii} . From this the maximum is picked out, and this is averaged over 25 configurations, yielding the configuration-averaged maximum self energy correction, $\bar{\sigma}_m$. That the excess is magnon energy for the highest mode matches well with the maximum of the local self-energy correction strongly supports that the high energy magnon modes involves spin-deviation at those sites where the locally averaged hopping terms are the maximum. This implies that the upper end of the magnon-energy

spectrum is entirely determined by local correlations in random hopping terms. In as much as this part of the magnon spectrum is most important in the two-magnon scattering, features such as the strong asymmetry can thus be traced to these local correlations in hopping disorder.

Table 3.1: Variation of the configuration-averaged maximum magnon energy $\overline{\omega_m}$ with hopping disorder strength σ . Also shown are the configuration-averaged increase in magnon energy $\overline{\omega_m} - \omega_m^0$ for the highest magnon mode relative to the pure-case energy ω_m^0 , and comparison with the configuration-averaged maximum self-energy correction $\overline{\Sigma_m}$ evaluated from Eq. (3.9).

σ	$\overline{\omega_m}/J$	$(\overline{\omega_m} - \omega_m^0)/J$	$\overline{\Sigma_m}/J$
0.0	1.89	0	0
0.1	3.05	1.16	1.12
0.2	3.44	1.55	1.58
0.3	3.95	2.06	1.93

A convenient way to exhibit the strong renormalization of high-energy magnons is via the magnon density of states:

$$N(\omega) = \lim_{\eta \rightarrow 0} \frac{1}{\pi} \frac{1}{N_n} \sum_n \frac{\eta}{(\omega - \omega_n)^2 + \eta^2} \quad (3.15)$$

where ω_n 's denote the magnon energies and η is chosen to be of the order of average level spacing. N_n represents the total number of modes obtained from the 50 different configurations considered. The results for the magnon DOS are plotted in Fig. (3.3) for different values of σ . Also shown for comparison is the DOS for the pure system which extends upto energy $\sim 2J$. It is observed that the DOS for the hopping-disordered system extends well beyond the maximum energy $2J$, though the position of the peak remains roughly the same.

We have also examined the magnon wavefunction for modes at the high-energy end of the spectrum, and find that indeed these modes are strongly localized in certain regions of the lattice, as expected from the analysis discussed earlier. The magnon amplitudes are contained in the eigenvectors $|\phi_\lambda(\omega)\rangle$ of the $[\chi^0(\omega)]$ matrix evaluated at the magnon

energies. A useful way to exhibit the magnon modes on the lattice is via arrows with size proportional to the local magnon amplitude ϕ_λ^i , and orientation proportional to the rotation angle $\theta_i = \sin^{-1}(\phi_\lambda^i/S_z^i)$, where S_z^i is the local magnetization.[15] The zero-energy (Goldstone) mode in this representation is characterized by identical rotation angles, despite the local magnetization and magnon amplitudes having different magnitudes on the lattice sites due to disorder. We have also confirmed that this localization of high-energy magnon modes occurs in those regions of the lattice where the locally-averaged hopping is significantly higher than the bulk average, so that the locally-averaged U/t ratio and the local magnetization are low.

In conclusion, we have studied the antiferromagnet with hopping disorder, both perturbatively and also using a numerical method, in the strong correlation limit. We have shown that while the low-energy, long-wavelength magnon modes are only weakly affected, the high-energy modes are strongly affected because of a cooperative effect arising from local correlations in hopping disorder. There is therefore a strong asymmetry in the energy shifts of the low-energy and high-energy magnon modes. If indeed zero-point motion leads to hopping disorder in cuprates, then this work provides a qualitative understanding of the anomalous linewidth and asymmetric lineshape seen in the two-magnon Raman scattering in cuprate antiferromagnets. Also, the strong energy renormalization of high-energy magnons due to the cooperative effect of hopping disorder leads to an insight into the extraordinary sensitivity of the Raman scattering process on the zero-point motion of the lattice.

Appendix A

In this Appendix we discuss the evaluation of the $[\delta\chi_0]_{ii}$ matrix element in the strong correlation limit wherein terms only upto order $\frac{t^2}{\Delta^3}$ have been retained. From Fig. 3.1(a) one can write,

$$[\delta\chi_0]_{ii} = i \int \frac{d\omega'}{2\pi} G_{ii}^{\dagger\ominus}(\omega') \sum_k \delta t_{ik} G_{ki}^{\dagger\ominus}(\omega') G_{ii}^{\downarrow\oplus}(\omega - \omega') \quad (3.16)$$

where G 's represent the host Green's functions, \oplus, \ominus refer to the quasiparticle bands and the sum over k represents the sum over all z nearest neighbours. Substituting the expressions for the Green's functions appropriate upto order t/Δ one obtains,

$$[\delta\chi_0(\omega)]_{ii} = i \int \frac{d\omega'}{2\pi} \left(\frac{1}{\omega' - \Delta^\ominus - i\eta} \right) \cdot \sum_k \delta t_{ik} \cdot \left[\frac{-t/2\Delta}{\omega' - \Delta^\ominus - i\eta} + \frac{t/2\Delta}{\omega' - \Delta^\oplus + i\eta} \right] \cdot \left(\frac{1}{\omega' - \omega - \Delta^\oplus + i\eta} \right) \quad (3.17)$$

where $\Delta^\ominus/\Delta^\oplus = -\Delta/\Delta$.

The frequency integral yields,

$$[\delta\chi_0(\omega)]_{ii} = -\frac{t^2}{4\Delta^3} \sum_k \frac{\delta t_{ik}}{t} \quad (3.18)$$

Identical result is obtained corresponding to the dashed line (δ_{ik}) being put in the lower (\downarrow -spin) propagator. Hence summing up the contribution from both these processes we obtain,

$$[\delta\chi_0(\omega)]_{ii} = -\frac{t^2}{2\Delta^3} \sum_k \frac{\delta t_{ik}}{t} \quad (3.19)$$

Similarly the off-diagonal contribution $[\delta\chi_0]_{ij}$ can be shown to be equal to,

$$[\delta\chi_0(\omega)]_{ij} = -\frac{t^2}{2\Delta^3} \frac{\delta t_{ij}}{t} \quad (3.20)$$

Bibliography

- [1] K. Lyons, P. A. Fleury, J. P. Remeika, A. S. Cooper and T. J. Negran, Phys. Rev. B **37**, 2353 (1988).
- [2] R. R. P. Singh, P. A. Fleury, K. B. Lyons, and P. E. Sulewski, Phys. Rev. Lett. **62**, 2736 (1989).
- [3] P. E. Sulewski, P. A. Fleury, K. B. Lyons, S-W. Cheong and Z. Fisk, Phys. Rev. **41**, 225 (1990).
- [4] S. Basu and A. Singh, Phys. Rev. B **54**, 6356 (1996).
- [5] P. A. Fleury and R. Loudon, Phys. Rev. **166**, 514 (1968).
- [6] J. Solyom, Z. Physik, **243**, 382 (1971).
- [7] F. Nori, R. Merlin, S. Haas, A. W. Sandvik, and E. Dagotto, Phys. Rev. Lett. **75**, 553 (1995).
- [8] A. V. Chubokov and D. M. Frenkel, Phys. Rev. Lett. **74**, 3057 (1995); Phys. Rev. B **52**, 9760 (1995).
- [9] S. L. Cooper, D. Reznick, A. L. Kotz, M. A. Karlow, R. Liu, M. V. Klein, W. C. Lee, J. Giapintzakis, D. M. Ginzberg, B. W. Veal and A. P. Paulikas, Phys. Rev. B **47**, 8233 (1993).
- [10] M. C. Aronson, S. B. Dierkar, B. S. Dennis, S. W. Cheong, and Z. Fisk, Phys. Rev. B **44**, 4657 (1991).

-
- [11] P. Sen and A. Singh, Phys. Rev. B **53**, 328 (1996).
 - [12] A. Singh and Z. Tešanović, Phys. Rev. B **41**, 11457 (1990).
 - [13] S. Basu and A. Singh, Phys. Rev. B **53**, 6406 (1996).
 - [14] A. Singh, Phys. Rev. B **43**, 3617 (1991).
 - [15] A. Singh and Z. Tešanović, Phys. Rev. B **41**, 614 (1990).

Chapter 4

Hopping-disorder-induced effects upon Raman Scattering spectrum in an Antiferromagnet

4.1 Introduction

In Chapter 3 we have discussed the hopping-disorder-induced effects upon the magnon spectrum in an antiferromagnet. It has been shown explicitly that while the low-energy magnon modes are negligibly affected by disorder, there is a substantial effect upon the high energy modes. It was also mentioned there that such asymmetric magnon energy renormalization can provide a clue to the considerable asymmetry in the two-magnon Raman lineshape. Here we are going to investigate the effects of hopping disorder upon the two-magnon Raman scattering intensity in an antiferromagnet.

We have seen earlier that in Nori *et al.*'s[1] approach the hopping disorder is looked upon as an interaction between the lattice excitation (i.e. phonons) and the spin excitations (i.e. magnons) which induces changes δJ_{ij} , in the exchange integral J . An estimate of the mean square deviation $\langle (\frac{\delta J_{ij}}{J})^2 \rangle$ is made and to make a comparison with the experimental data the corresponding value is considered to be as high as 0.5. It has been suspected[2] that such a large variation in J appears physically unreasonable and questioned that whether more moderate values of $\langle \frac{\delta J_{ij}}{J} \rangle$ are sufficient to achieve agreement with experiments. Essentially what one obtains is that the coupling of phonons to the spin excitations leads to the broadening of

a two-magnon peak, the asymmetry of the lineshape about its maximum towards the higher energy regime and appearance of scattering intensity in forbidden geometries like A_{1g} , B_{2g} etc.

Earlier, we have investigated,[3] the effect of lattice fluctuation induced hopping disorder in the context of Mott-Hubbard AF where the hopping term t_{ij} include random terms. The Hubbard Hamiltonian in this case can be written as,

$$\hat{H} = - \sum_{\langle ij \rangle, \sigma} (t + \delta t_{ij}) (a_{i\sigma}^\dagger \hat{a}_{j,\sigma} + \text{h.c.}) + U \sum_i \hat{n}_{i\uparrow} \hat{n}_{i\downarrow} \quad (4.1)$$

$$P\left(\frac{\delta t_{ij}}{t}\right) = \frac{1}{\sqrt{2\pi}\sigma} \exp\left[-\frac{(\delta t_{ij}/t)^2}{2\sigma}\right] \quad (4.2)$$

where the random terms δt_{ij} 's for each bond are chosen independently from a gaussian distribution and the distribution width $\sqrt{\sigma}$ measures the strength of disorder. There we have examined both perturbatively and using a numerical method - effects of hopping disorder on magnon energies, their wavefunctions and on the density of states (DOS). In both schemes, the spin-wave energies are obtained at the Random Phase Approximation (RPA) level. We have obtained a strong renormalization in energy of the high energy magnon modes, arising from locally correlated hopping, which results in appreciable one-magnon DOS well beyond the maximum spin-wave energy $2J$ for the pure system. This result has got important implications in explaining the experimentally observed Raman spectrum.

To obtain the Raman scattering intensity we need to consider the imaginary part of the full two-magnon propagator which in turn requires the knowledge of spin-wave energies. For a finite size system these energies are obtained numerically at the RPA level in presence of disorder using a numerical method discussed in detail in Chapter 3. Following a prescription of the mode assignments discussed in section 4.3, it is possible to obtain the symmetry factor required for the B_{1g} scattering geometry. It is observed that even for a sufficiently small strength of disorder, $\sigma = 0.01$, (much smaller than the values considered by Nori *et al.*[1])

though the Raman spectrum on the lower energy side is weakly affected, there is a substantial change in the higher frequency regime and a good agreement is obtained with the experimental data. This confirms our earlier statement[3] that if indeed the randomness in hopping due to zero-point lattice fluctuation is playing a key-role in explaining the long standing puzzling feature of the Raman lineshape regarding the asymmetry, then it essentially arises from the highly asymmetric magnon-energy renormalization.

4.2 Configuration averaging of the two-magnon propagator

The Fleury-Loudon (FL) Hamiltonian which represents the interaction between the photon and the spin pairs can be written as,

$$H_R = A \sum_{\mathbf{r}, \hat{\delta}} (\mathbf{E}_{\text{inc}} \cdot \hat{\delta}) \cdot (\mathbf{E}_{\text{sc}} \cdot \hat{\delta}) \mathbf{S}(\mathbf{r}) \cdot \mathbf{S}(\mathbf{r} + \hat{\delta}) \quad (4.3)$$

Where the \mathbf{E}_{inc} and \mathbf{E}_{sc} are the incident and the scattered electric field vectors, $\hat{\delta}$ is the unit vector connecting nearest neighbour (NN) sites of opposite sublattices and A is a constant. The sum over \mathbf{r} ensures that the spin excitations have net zero momentum as the incoming photon has essentially zero momentum. For calculation of the Raman intensity one needs to consider the correlation function of the spin pair operator,

$$P_{\hat{\delta}} = \sum_{\mathbf{r}} \mathbf{S}(\mathbf{r}) \cdot \mathbf{S}(\mathbf{r} + \hat{\delta}) \quad (4.4)$$

For the B_{1g} symmetry we have,

$$\mathbf{E}_{inc} \sim \hat{x} - \hat{y},$$

$$\mathbf{E}_{sc} \sim \hat{x} + \hat{y}.$$

So that the Hamiltonian assumes the form,

$$H_R \sim \sum_{\mathbf{r}, p=\pm 1} \mathbf{S}(\mathbf{r}) \cdot \{\mathbf{S}(\mathbf{r} + p\hat{x}) - \mathbf{S}(\mathbf{r} + p\hat{y})\} \quad (4.5)$$

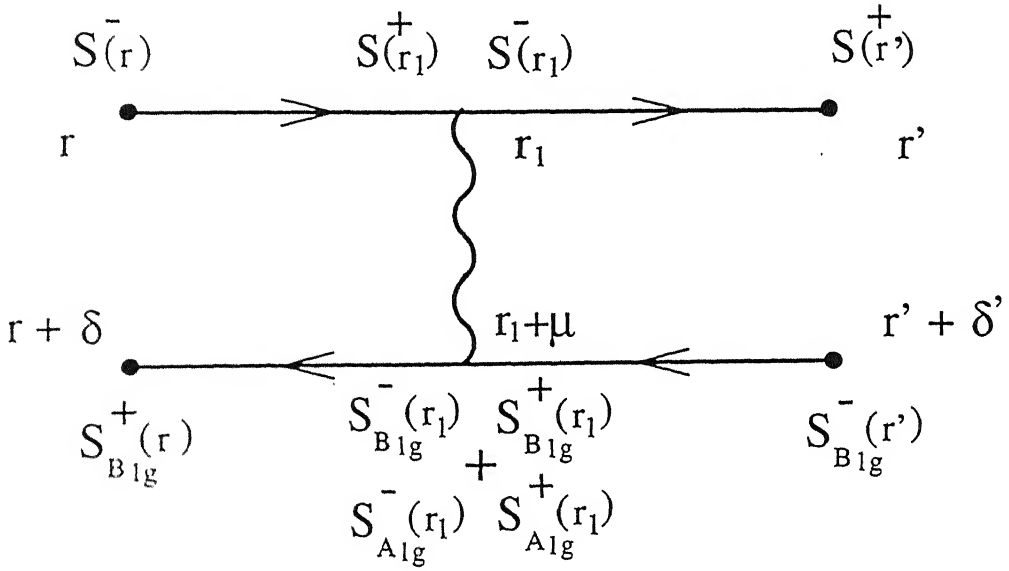


Figure 4.1: Interaction between two magnons is shown where the bold lines represent the two magnons propagating from neighbouring sites \mathbf{r} and $\mathbf{r} + \delta$ to \mathbf{r}' and $\mathbf{r}' + \delta'$. The wavy lines denotes the interaction between the magnons at sites \mathbf{r}_1 and $\mathbf{r}_1 + \mu$ where μ connects to the nearest neighbouring sites. The creation and destruction of magnons at these points are shown by S^+ and S^- where the subscripts B_{1g} and A_{1g} correspond to different scattering geometries defined in the text.

Now let us consider the diagram representing (Fig. (4.1)) the interaction between the magnons in real space. The interaction between the magnons excited at sites \mathbf{r}_1 and $\mathbf{r}_1 + \mu$ can be written as,

$$\hat{V}_{\text{int}} = -J \sum_{\mathbf{r}_1, \mu} S^-(\mathbf{r}_1) S^+(\mathbf{r}_1) S^-(\mathbf{r}_1 + \mu) S^+(\mathbf{r}_1 + \mu) \quad (4.6)$$

where μ connects to NN sites of the opposite sublattice. The form of the interaction indicates that the propagators on either sides of the interaction line are coupled as μ can connect both in the \hat{x} and \hat{y} direction. But they can be decoupled if one rewrites the interaction term as (see Fig. (4.1)),

$$\begin{aligned} \hat{V}_{\text{int}} = -J \sum_{\mathbf{r}_1} S^-(\mathbf{r}_1) S^+(\mathbf{r}_1) & \left[S_{O_1}^-(\mathbf{r}_1) S_{O_1}^+(\mathbf{r}_1) + S_{O_2}^-(\mathbf{r}_1) S_{O_2}^+(\mathbf{r}_1) \right. \\ & \left. + S_{O_3}^-(\mathbf{r}_1) S_{O_3}^+(\mathbf{r}_1) + S_{O_4}^-(\mathbf{r}_1) S_{O_4}^+(\mathbf{r}_1) \right] \end{aligned} \quad (4.7)$$

where the 4 operators are defined in the following way,

$$S_{O_1}^\pm(\mathbf{r}) = \frac{1}{2} \sum_p \{ S^\pm(\mathbf{r} + p\hat{x}) - S^\pm(\mathbf{r} + p\hat{y}) \}$$

$$S_{O_2}^\pm(\mathbf{r}) = \frac{1}{2} \sum_p \{ S^\pm(\mathbf{r} + p\hat{x}) + S^\pm(\mathbf{r} + p\hat{y}) \}$$

$$S_{O_3}^\pm(\mathbf{r}) = \frac{1}{2} \sum_p \{ p S^\pm(\mathbf{r} + p\hat{x}) - p S^\pm(\mathbf{r} + p\hat{y}) \}$$

$$S_{O_4}^\pm(\mathbf{r}) = \frac{1}{2} \sum_p \{ p S^\pm(\mathbf{r} + p\hat{x}) + p S^\pm(\mathbf{r} + p\hat{y}) \}$$

where the +sign and the -sign in the superscript refers to raising and lowering operators respectively. It can be seen that these operators correspond to the different irreducible representations presented in Appendix C of Chapter 2. The first two operators correspond to B_{1g} and A_{1g} symmetry factors respectively. Hence explicitly we write them as $S_{B_{1g}}^\pm$ and $S_{A_{1g}}^\pm$ for our convenience. In this new notation the interaction term looks like,

$$\hat{V}_{\text{int}} = -J \sum_{\mathbf{r}_1} S^-(\mathbf{r}_1) S^+(\mathbf{r}_1) \left[S_{\mathbf{B}_{1\mathbf{g}}}^-(\mathbf{r}_1) S_{\mathbf{B}_{1\mathbf{g}}}^+(\mathbf{r}_1) + S_{\mathbf{A}_{1\mathbf{g}}}^-(\mathbf{r}_1) S_{\mathbf{A}_{1\mathbf{g}}}^+(\mathbf{r}_1) \right. \\ \left. + S_{\mathbf{O}_3}^-(\mathbf{r}_1) S_{\mathbf{O}_3}^+(\mathbf{r}_1) + S_{\mathbf{O}_4}^-(\mathbf{r}_1) S_{\mathbf{O}_4}^+(\mathbf{r}_1) \right] \quad (4.8)$$

Having written the interaction term we proceed to define the spin-wave propagators for different geometries. In Fig. (4.1) the spin raising and lowering operators at \mathbf{r} and $\mathbf{r} + \hat{\delta}$ are denoted by $S^-(\mathbf{r})$ and $S_{\mathbf{B}_{1\mathbf{g}}}^-(\mathbf{r})$ and those at \mathbf{r}' and $\mathbf{r}' + \hat{\delta}'$ are denoted by $S^-(\mathbf{r}')$ and $S_{\mathbf{B}_{1\mathbf{g}}}^-(\mathbf{r}')$. This immediately suggests that $\hat{\delta}$ and $\hat{\delta}'$ which connect NN pairs are fixed in space and we can write the spin-wave propagators as,

$$\chi^{-+}(\mathbf{r}, \mathbf{r}') = \langle \psi_G | S^-(\mathbf{r}) S^+(\mathbf{r}') | \psi_G \rangle \quad (4.9)$$

corresponding to the upper line and,

$$\chi_{\mathbf{B}_{1\mathbf{g}}}^{+-}(\mathbf{r}, \mathbf{r}') = \langle \psi_G | S_{\mathbf{B}_{1\mathbf{g}}}^+(\mathbf{r}) S_{\mathbf{B}_{1\mathbf{g}}}^-(\mathbf{r}') | \psi_G \rangle \quad (4.10)$$

corresponding to the lower one in Fig. (4.1). Now the time-ordered two-magnon propagator in the $\mathbf{B}_{1\mathbf{g}}$ geometry can be defined as,

$$G_{\mathbf{B}_{1\mathbf{g}}}^{(0)}(\omega) = -i \int dt e^{i\omega(t-t')} \langle \psi_G | T \left[\sum_{\mathbf{r}, \mathbf{r}'} S^-(\mathbf{r}, t) S_{\mathbf{B}_{1\mathbf{g}}}^+(\mathbf{r}, t) S^+(\mathbf{r}', t') S_{\mathbf{B}_{1\mathbf{g}}}^-(\mathbf{r}', t') \right] | \psi_G \rangle \quad (4.11)$$

For calculating the Raman intensity first consider the non-interacting limit of the two-magnon propagator,

$$G_{\mathbf{B}_{1\mathbf{g}}}^{(0)}(\omega) = i \int \frac{d\omega_1}{2\pi} \sum_{\mathbf{r}, \mathbf{r}'} \chi^{-+}(\mathbf{r}, \mathbf{r}', \omega_1) \chi_{\mathbf{B}_{1\mathbf{g}}}^{+-}(\mathbf{r}, \mathbf{r}', \omega - \omega_1) \quad (4.12)$$

The configuration averaged two-magnon Raman propagator is given by,

$$\overline{G_{\mathbf{B}_{1\mathbf{g}}}^{(0)}(\omega)} = i \int \frac{d\omega_1}{2\pi} \sum_{\mathbf{r}, \mathbf{r}'} \overline{\chi^{-+}(\mathbf{r}, \mathbf{r}', \omega_1) \chi_{\mathbf{B}_{1\mathbf{g}}}^{+-}(\mathbf{r}, \mathbf{r}', \omega - \omega_1)} \quad (4.13)$$

We can decouple the two propagators if we neglect the corrections arising due to exchange between the magnons. This allows us to write,

$$\overline{G_{B_{1g}}^0(\omega)} = i \int \frac{d\omega_1}{2\pi} \sum_{\mathbf{r}, \mathbf{r}'} \overline{\chi^{-+}(\mathbf{r}, \mathbf{r}', \omega_1)} \overline{\chi_{B_{1g}}^{+-}(\mathbf{r}, \mathbf{r}', \omega - \omega_1)} \quad (4.14)$$

Having done the configuration averaging of $G^0(\omega)$ one can proceed to calculate the two-magnon Raman intensity which is obtained from imaginary part of $\overline{G(\omega)}$ where,

$$\overline{G(\omega)} = \left[\frac{G_0(\omega)}{1 + JG_0(\omega)} \right] \quad (4.15)$$

We can neglect the vertex corrections since they appear only at the second order level and hence proportional to the fourth power of the disorder strength *i.e.* $\left(\frac{\delta t}{t}\right)^4$ (in reference [4] this result is shown explicitly for the on-site (diagonal) disorder case and calculation of the vertex correction is discussed elaborately in presence of on-site disorder in Chapter 5). So for weak disorder, the correction will be insignificant. This enables to write,

$$\overline{G(\omega)} = \left[\frac{\overline{G_0(\omega)}}{1 + J\overline{G_0(\omega)}} \right] \quad (4.16)$$

We have shown it in Appendix A that the B_{1g} symmetry factor viz. $(\cos q_x - \cos q_y)^2$ corresponding to the pure case is obtained by Fourier transforming the non-interacting two-magnon propagator $G_{B_{1g}}^0$. This symmetry factor is important for calculating the two-magnon Raman spectrum. It can also be noted that due to the form of the interaction *i.e.* presence of both B_{1g} and A_{1g} terms in \hat{V}_{int} , off-diagonal combinations of different scattering geometries in $G^0(\omega)$ are possible. In that case the symmetry factor will contain contributions from different geometries. We can see it clearly if one considers the term, $\langle S_{B_{1g}}^+(\mathbf{r}) S_{A_{1g}}^-(\mathbf{r}') \rangle$, which when Fourier transformed yields,

$$\sum_q (\cos q_x - \cos q_y)(\cos q_x + \cos q_y) \chi^{+-}(q, \omega) \quad (4.17)$$

But this symmetry term can be shown to be identically equal to zero for all frequencies be-

cause of the symmetry present in the magnetic Brillouin Zone. Hence the only terms which survive are the ones that are diagonal in scattering geometries[5].

4.3 Mode Assignments

Here we want to establish a one-to-one correspondence between the pure system and the one in presence of hopping disorder. This we believe to be valid if the strength of disorder is weak. For doing this we calculate the magnon modes numerically for a 10×10 system in absence of disorder in the strong-coupling limit ($U/t = 200$). This procedure of obtaining the magnon modes numerically has been discussed in Chapter 3. These modes thus obtained are assigned a pair of mode numbers n_x and n_y which are related to the wavevectors q_x and q_y via the relation $q_{x/y} = \frac{2\pi}{L}n_{x/y}$ in the translationally invariant (pure) case. The numbers n_x and n_y are chosen such that the corresponding q_x and q_y are restricted to the upper-half (first two quadrants) of the Brillouin Zone (BZ) where q_x is allowed to have both positive and negative values (ranging from $-\pi$ to $+\pi$) whereas q_y is assigned only positive values (from 0 to π). The other half of the BZ does not need to be considered as the q_x and q_y values (or equivalently the n_x and n_y) lying within the region specified (see Fig. (4.2)) are sufficient to label all the modes. The Goldstone mode or the lowest energy mode is assigned with the mode numbers $n_x = 0$, $n_y = 0$, the second collective mode with $n_x = 1$, $n_y = 0$ (or equivalently $n_x = 0$, $n_y = 1$), the third one with $n_x = 1$, $n_y = 1$ and so on. Having done with the assigning scheme it is now possible to form the symmetry factor for the B_{1g} scattering geometry which is $\phi_n^2 = [\cos(\frac{2\pi}{L}n_x) - \cos(\frac{2\pi}{L}n_y)]^2$. As mentioned earlier this symmetry factor is crucial for calculating the two-magnon Raman intensity. The consistency of the mode assigning scheme is checked by re-evaluating the magnon energies using the mode numbers via the relation $\omega_n = 2J\sqrt{1 - \gamma_n^2}$ where $\gamma_n = \frac{1}{2}[\cos(\frac{2\pi}{L}n_x) + \cos(\frac{2\pi}{L}n_y)]$ and $J = \frac{4t^2}{U} = 0.02$ (i.e. $U/t = 200$). The energies thus obtained show excellent agreement with the ones calculated from the numerical method. The same mode assignments are expected to be carried over for the intermediate coupling regime. We show the comparison between

the energies calculated numerically and the ones evaluated by using the analytical expression relevant to the intermediate- U regime ($U/t = 10$) in Table 4.1 where we have,

$$\omega_n = 2J \left[(1 - \gamma_n^2) - \frac{t^2}{\Delta^2} \left\{ 6 + 3 \cos \left(\frac{2\pi}{L} \right) n_x \cos \left(\frac{2\pi}{L} \right) n_y - 9 \gamma_n^2 \right\} \right]^{1/2} \quad (4.18)$$

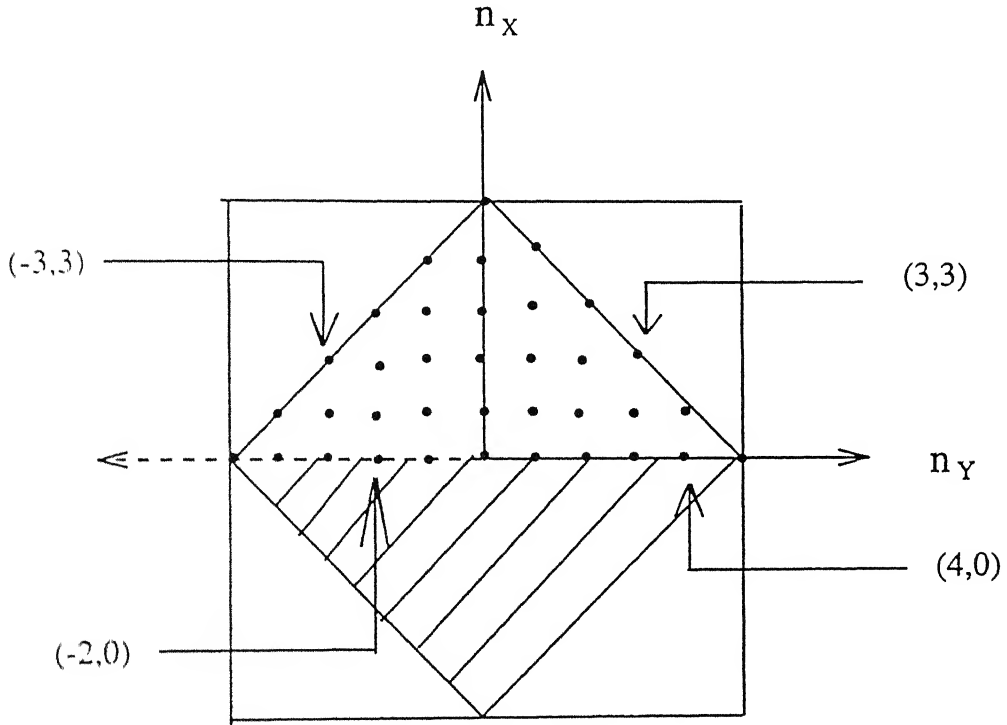


Figure 4.2: The region in the Brillouin Zone (BZ) is shown where the dots denote the mode numbers n_x and n_y chosen so as to assign labels to the mode energies calculated. A few of the mode numbers are indicated. The first two quadrants are required for assigning numbers to all the modes.

We establish the correspondence between the pure and the disordered system by assuming

the same assigning scheme continues to work for the disordered system. We show the mode energies for the disordered system ($\sigma = 0.1$) for a particular configuration in Table 4.2. We also notice that the degeneracy of the modes is lifted due to the presence of disorder and the low energy modes are not significantly affected whereas there is a considerable effect towards the higher energy side.

Table 4.1: The mode energies are obtained using the expression relevant to the intermediate- U regime ($U/t = 10$ or $\Delta/t = 5$) for a 10×10 system where $n_{x/y} = (\frac{L}{2\pi})q_{x/y}$ are the mode numbers specified in the leftmost column. Also we have shown the energies calculated numerically using the exact eigenstate method for comparison. The symmetry factors for both B_{1g} and A_{1g} scattering geometries are obtained using the mode numbers.

Mode Nos. (n_x, n_y)	ω_n (numerical)	ω_n (formula)	$\phi_n^2(B_{1g})$	$\phi_n^2(A_{1g})$
(-5,0)	0.7548	0.7505	4.000	0.000
(4,0) (0,4) (-4,0) (-5,1)	0.7438	0.7408	2.618	0.000
(4,1) (1,4) (-4,1) (-1,4)	0.7396	0.7356	0.382	0.000
(3,2) (2,3) (-3,2) (-2,3)	0.7150	0.6931	3.272	0.037
(3,1) (1,3) (-3,1) (-1,3)	0.7030	0.6927	1.250	0.250
(4,2) (2,4) (-4,2) (-2,4)				
(3,0) (0,3) (-3,0) (-5,2)	0.6882	0.6793	0.000	0.382
(2,2) (3,3) (-2,2) (-3,3)	0.6765	0.6696	1.713	0.478
(2,1) (1,2) (-2,1) (-1,2)	0.5945	0.5826	0.250	1.250
(4,3) (3,4) (-4,3) (-3,4)				
(2,0) (0,2) (-2,0) (-5,3)	0.5469	0.5458	0.477	1.714
(1,1) (4,4) (-1,1) (-4,4)	0.4199	0.4102	0.000	2.618
(1,0) (0,1) (-1,0) (-5,4)	0.3061	0.2987	0.036	3.273
(0,0)	0.0000	0.0000	0.000	4.000

Table 4.2: Here the assignment of the mode numbers n_x and n_y is shown for the mode energies calculated numerically for both pure and disordered systems ($\sigma = 0.1$) of system size 10×10 and for $U/t = 10$.

Mode Nos. (n_x, n_y)	ω_n (pure case)	ω_n (disordered case)
(-5,0)	0.7548	1.3006
(4,0) (0,4) (-4,0) (-5,1)	0.7438	1.2222, 1.2024, 1.1960, 1.1346
(4,1) (1,4) (-4,1) (-1,4)	0.7396	1.0578, 1.0178, 1.0137, 0.9955
(3,2) (2,3) (3,2) (-2,3)	0.7150	0.8557, 0.8414, 0.8291, 0.7934
(3,1) (1,3) (3,1) (-1,3)	0.7030	0.7854, 0.7762, 0.7698, 0.7641
(4,2) (2,4) (-4,2) (-2,4)		0.7228, 0.7018, 0.6935, 0.6624
(3,0) (0,3) (-3,0) (-5,2)	0.6882	0.6614, 0.6554, 0.6364, 0.6197
(2,2) (3,3) (-2,2) (-3,3)	0.6765	0.6020, 0.5773, 0.5668, 0.5411
(2,1) (1,2) (-2,1) (-1,2)	0.5945	0.5251, 0.5167, 0.4926, 0.4784
		0.4527, 0.4361, 0.4256, 0.4151
(2,0) (0,2) (-2,0) (-5,3)	0.5469	0.3969, 0.3711, 0.3595, 0.3424
(1,1) (4,4) (-1,1) (-4,4)	0.4199	0.3320, 0.3170, 0.2909, 0.2778
(1,0) (0,1) (-1,0) (-5,4)	0.3061	0.2390, 0.2118, 0.1801, 0.1643
(0,0)	0.0000	0.0000

4.4 Calculation of the two-magnon Raman intensity

As before,[6] (also see Chapter 2) we can express the propagator in terms of it's non-interacting components $G_0(\omega)$. The mode assignments allows us to write $G_0(\omega)$ in a 2×2 matrix form with the mode energies and the symmetry factors labeled by the mode numbers $n (= \sqrt{n_x^2 + n_y^2})$. Hence we can sum up the perturbation series in powers of the interaction between the magnons and which yields,

$$[G_n(\omega)] = \frac{[G_{0n}]}{1 + J[G_{0n}]} \quad (4.19)$$

As in reference [6] the above equation is written in terms of the matrix elements,

$$[G_{0n}(\omega)]_{AA} = A_n,$$

$$[G_{0n}(\omega)]_{BB} = B_n \quad \text{and}$$

$$[G_{0n}(\omega)]_{AB} = [G_{0n}(\omega)]_{BA} = C_n$$

$$\overline{G_n(\omega)} = \frac{A_n + B_n + 2C_n + 2J(A_n B_n - C_n^2)}{(1 + JA_n)(1 + JB_n) - J^2 C_n^2} \quad (4.20)$$

where A_n , B_n and C_n are defined as,

$$\begin{aligned} A_n &= \frac{1}{n} \sum_n m^2 \phi_n^2 \left(\frac{2J}{\omega_n} \right)^2 \left[a_n^2 - \left(\frac{\omega_n}{2J} \right)^2 - \left(\frac{a_n \omega}{2J} \right) + \frac{1}{2} \left(\frac{\omega}{2J} \right)^2 \right] \left[\frac{1}{\omega - 2\omega_n} - \frac{1}{\omega + 2\omega_n} \right] \\ B_n &= \frac{1}{n} \sum_n m^2 \phi_n^2 \left(\frac{2J}{\omega_n} \right)^2 \left[a_n^2 - \left(\frac{\omega_n}{2J} \right)^2 + \left(\frac{a_n \omega}{2J} \right) + \frac{1}{2} \left(\frac{\omega}{2J} \right)^2 \right] \left[\frac{1}{\omega - 2\omega_n} - \frac{1}{\omega + 2\omega_n} \right] \\ C_n &= \frac{1}{n} \sum_n m^2 \phi_n^2 \left(\frac{2J}{\omega_n} \right)^2 [b^2 \gamma_n^2] \left[\frac{1}{\omega - 2\omega_n} - \frac{1}{\omega + 2\omega_n} \right] \end{aligned}$$

where,

$$\begin{aligned} m &= 1 - 2 \frac{t^2}{\Delta^2}, \quad a_n = 1 - \frac{t^2}{\Delta^2} \left\{ 3 + \frac{3}{2} \cos\left(\frac{2\pi}{L} n_x\right) \cos\left(\frac{2\pi}{L} n_y\right) + \gamma_n^2 \right\} \quad \text{and} \\ b &= 1 - \frac{11}{2} \frac{t^2}{\Delta^2} \end{aligned}$$

In Fig. (4.3) we have shown the Raman scattering spectra in the B_{1g} symmetry as a function of transferred photon frequency ω (in units of J) for a system size 10×10 in presence of disorder ($\sigma = 0.1$) and $U/t = 10$. It is noticed that the linewidth to peak position ratio is even higher than unity, whereas the experimentally value is closed to 0.38[8]. This shows clearly that the strength of disorder σ (or equivalently the mean square deviation $\langle (\frac{\delta J_{ij}}{J})^2 \rangle$) does not need to be as large as 0.1 in order to get an agreement with the experimentally observed data for the Raman spectrum. Fig. (4.4) shows the same plot for more moderate values of σ viz $\sigma = 0.01$ and 0.03 . The spectral lineshape for the pure case ($\sigma = 0$) is included for comparison. This plot is reminiscent of the magnon DOS shown in Fig. (3.4). There we have considered much larger strengths of disorder ($\sigma = 0.1$ and 0.3). It can be observed that the linewidth to peak position ratio increases from 0.283 corresponding to the pure case to 0.37 for $\sigma = 0.01$ and 0.410 for $\sigma = 0.03$ whereas the position of the peak roughly stays the same in all the cases. So it looks like $\sigma = 0.01$ roughly corresponds to the value that is needed

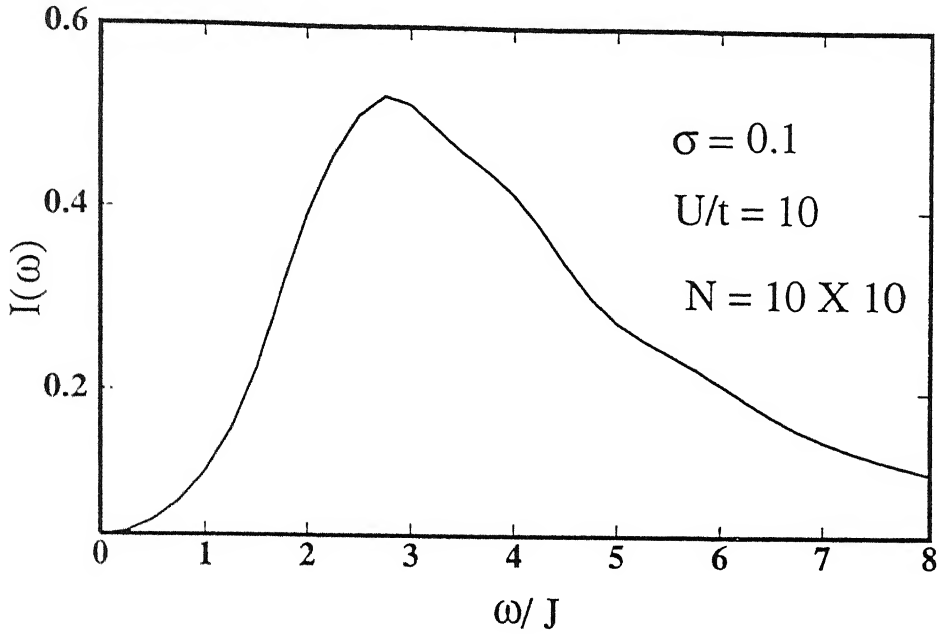


Figure 4.3: The two-magnon scattering intensity is plotted as a function of transferred photon frequency ω (in units of J) for the hopping disordered case with a gaussian disorder of width $\sigma = 0.1$.

for parameterizing disorder strength in order to obtain agreement with the experimentally obtained Raman lineshape. Also it is seen that in presence of disorder there is a pronounced asymmetry in the higher frequency region of the spectrum and a considerable intensity is observed all the way upto $6J$ and even more. This can be explained by arguing that the high energy magnon modes are strongly affected due to a cooperative effect arising from local correlations of hopping disorder, which resulted in an appreciable one-magnon DOS beyond the maximum energy $2J$ for the pure system[3]. So it seems that a much lesser value of the disorder strength can actually account for the puzzling features of the Raman lineshape. Finally, in Fig. (4.5) we plot the scattering spectrum in the strong coupling limit ($U/t = 100$) for various disorder strengths viz. $\sigma = 0.01, 0.03$ and 0.1 in order to draw comparisons with the results obtained by Nori *et al.*[1] since their work deals with the strong coupling limit *i.e.* $U/t \rightarrow \infty$. The linewidth to peak position ratio in this case comes out to be $0.333, 0.406$ and 1 corresponding to $\sigma = 0.01, 0.03$ and 0.1 . Also there is a pronounced asymmetry with

respect to the two-magnon peak in the higher frequency regime. To obtain an idea about the asymmetry we measure the quantity $I(\omega = 4J)/I_{max}(\omega)$. This has a value close to 0.4 which agrees very well with the corresponding quantity obtained from the experiments done on La_2CuO_4 (see Fig. (1.2)). Nori *et al.* obtained agreement with experiments for $\sigma_J \sim 0.5J$ (they have defined σ_J in units of J) which is much more than what we have considered. This can be explained by noting that their Quantum Monte Carlo (QMC) calculations of the Raman spectrum for a $S = 1/2$ Heisenberg antiferromagnet in the B_{1g} scattering geometry reveals a much lesser linewidth to peak-position ratio (~ 0.176) since in their calculation the intrinsic magnon damping has not been taken into account (remember we obtained 0.283 for the corresponding quantity from Fig. 2.2 which is much closer to the experimental value 0.38 than that of Nori *et al.*). This explains the reason why they need a much bigger width (σ) in the distribution of the exchange constant J so as to have an agreement with experiments. In fact, the evaluation of the different spectral moments of the Raman lineshape due to Singh *et al.*[8] shows the ratio of the second moment to that of the first one (which is like the linewidth to peak-position ratio) as 0.23 which tallies very well with the experimental value 0.28. In Appendix B we have included a brief discussion on the evaluation of different spectral moments which was extensively used by Singh *et al.*[8, 9] to analyze the Raman lineshape.

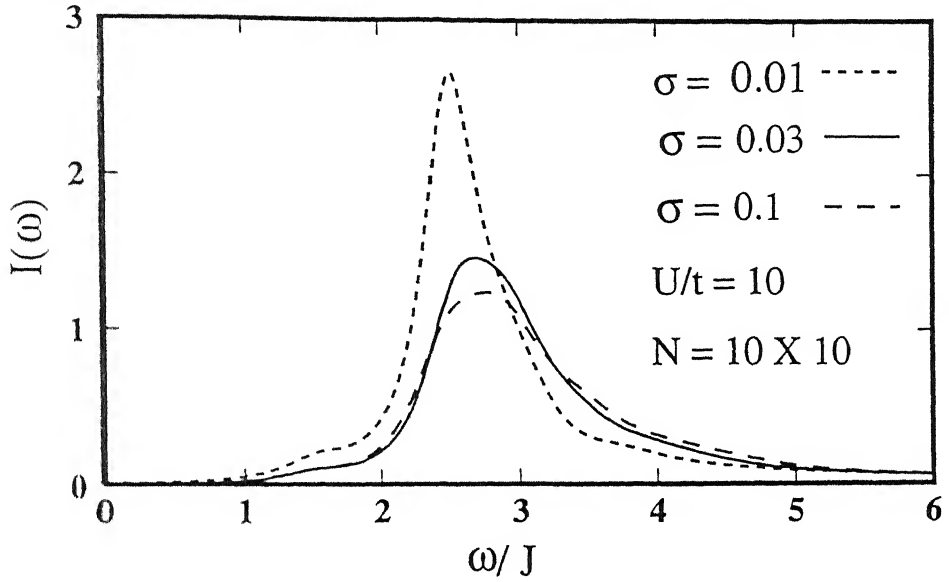


Figure 4.4: The two-magnon Raman lineshape is shown for more moderate values of disorder, viz. $\sigma = 0.01$ and 0.03 . The pure case ($\sigma = 0.0$) is included for comparison

In conclusion, we have studied the effects of hopping disorder on the two-magnon Raman intensity using the magnon energies calculated numerically. The energies for the disordered case are assumed to have a one-to-one correspondence with the ones in the pure case. This correspondence is established by assigning mode numbers n_x and n_y which are related to the momentum labels via the relation $q_{x/y} = (\frac{2\pi}{L})n_{x/y}$. The validity of the assigning scheme is checked for the pure case by re-evaluating the mode energies using the mode numbers and hence comparing them with the ones obtained numerically. Once the consistency of the assigning scheme is checked, the numbers can be used to determine the symmetry factors which are required for calculating the Raman intensity in different scattering geometries. For the Raman lineshape in the B_{1g} in presence of a small amount of disorder (σ as small as 0.01) symmetry it is observed that the lineshape broadens and alongwith there appears a substantial asymmetry towards the higher frequency side while the low-energy modes are weakly affected. It is also observed that the spectral intensity persists even beyond $6J$ where the joint magnon DOS diverges at $4J$. We also obtained a good agreement for the linewidth

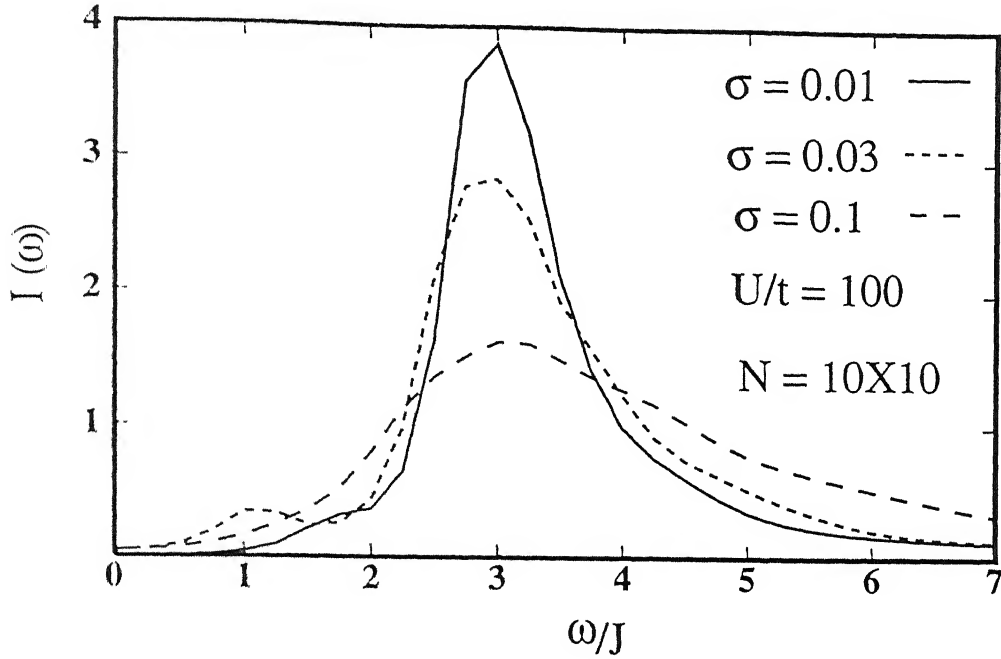


Figure 4.5: The two-magnon Raman lineshape is shown for the strong coupling case ($U/t = 100$) in order to compare with the results of Reference [1]. The values taken for disorder are $\sigma = 0.01, 0.03$ and 0.1 .

and asymmetry of the two-magnon profile observed experimentally from the Raman studies on cuprate insulators for $\sigma \approx 0.01$. This clearly reflects the role of zero-point fluctuations of the lattice to explain the anomalous features appearing in Raman spectrum for the cuprate antiferromagnets via a highly asymmetric magnon energy renormalization arising due to correlation of hopping disorder.

Appendix A

Here we find an expression for the symmetry factor appropriate to the B_{1g} scattering geometry. The Fleury-Loudon Hamiltonian for the B_{1g} scattering geometry is written as (see Eqn. (4.5)),

$$H = A \sum_{\mathbf{r}, p=\pm 1} \mathbf{S}(\mathbf{r}) \cdot \{\mathbf{S}(\mathbf{r} + p\hat{x}) - \mathbf{S}(\mathbf{r} + p\hat{y})\} \quad (4.21)$$

The two magnon propagator in the non-interacting limit for this case is,

$$G_0(\omega) = i \int \frac{d\omega_1}{2\pi} \sum_{\mathbf{r}, \mathbf{r}'} \chi^{+-}(\mathbf{r}, \mathbf{r}', \Omega_1) \chi_{B_{1g}}^{+-}(\tilde{\mathbf{r}}, \tilde{\mathbf{r}}', \omega - \omega_1) \quad (4.22)$$

where \mathbf{r}, \mathbf{r}' denote lattice sites and $\tilde{\mathbf{r}} = \mathbf{r} + \hat{\delta}$, $\tilde{\mathbf{r}}' = \mathbf{r}' + \hat{\delta}'$, where $\hat{\delta}/\hat{\delta}'$ connect to the sites neighbouring to \mathbf{r} and \mathbf{r}' in all the four directions i.e. $\hat{\delta}/\hat{\delta}'$ can be $p\hat{x}$ and $p\hat{y}$ with $p = \pm 1$. Also the spin raising and lowering operators forming the propagator is shown in the Fig. 4.5. Clearly $\chi_{B_{1g}}^{+-}$ consists of 16 terms with $\hat{\delta}$ and $\hat{\delta}'$ having all possible combinations which are enumerated below (the energy dependance is dropped temporarily).

$$\begin{aligned} \chi_{B_{1g}}^{+-}(\tilde{\mathbf{r}}, \tilde{\mathbf{r}}') &= \chi^{+-}(\mathbf{r} + \hat{x}, \mathbf{r}' + \hat{x}) + \chi^{+-}(\mathbf{r} + \hat{x}, \mathbf{r}' - \hat{x}) \\ &- \chi^{+-}(\mathbf{r} + \hat{x}, \mathbf{r}' + \hat{y}) - \chi^{+-}(\mathbf{r} + \hat{x}, \mathbf{r}' - \hat{y}) \\ &+ \chi^{+-}(\mathbf{r} - \hat{x}, \mathbf{r}' + \hat{x}) + \chi^{+-}(\mathbf{r} - \hat{x}, \mathbf{r}' - \hat{x}) \\ &- \chi^{+-}(\mathbf{r} - \hat{x}, \mathbf{r}' + \hat{y}) - \chi^{+-}(\mathbf{r} - \hat{x}, \mathbf{r}' - \hat{y}) \\ &- \chi^{+-}(\mathbf{r} + \hat{y}, \mathbf{r}' + \hat{x}) - \chi^{+-}(\mathbf{r} + \hat{y}, \mathbf{r}' - \hat{x}) \\ &+ \chi^{+-}(\mathbf{r} + \hat{y}, \mathbf{r}' + \hat{y}) + \chi^{+-}(\mathbf{r} + \hat{y}, \mathbf{r}' - \hat{y}) \\ &- \chi^{+-}(\mathbf{r} - \hat{y}, \mathbf{r}' + \hat{x}) - \chi^{+-}(\mathbf{r} - \hat{y}, \mathbf{r}' - \hat{x}) \\ &+ \chi^{+-}(\mathbf{r} - \hat{y}, \mathbf{r}' + \hat{y}) + \chi^{+-}(\mathbf{r} - \hat{y}, \mathbf{r}' - \hat{y}) \end{aligned} \quad (4.23)$$

To obtain the symmetry factor one has to fourier transform all the 16 terms in $G_0(\omega)$. As an example, the calculations for the first two terms are shown below,

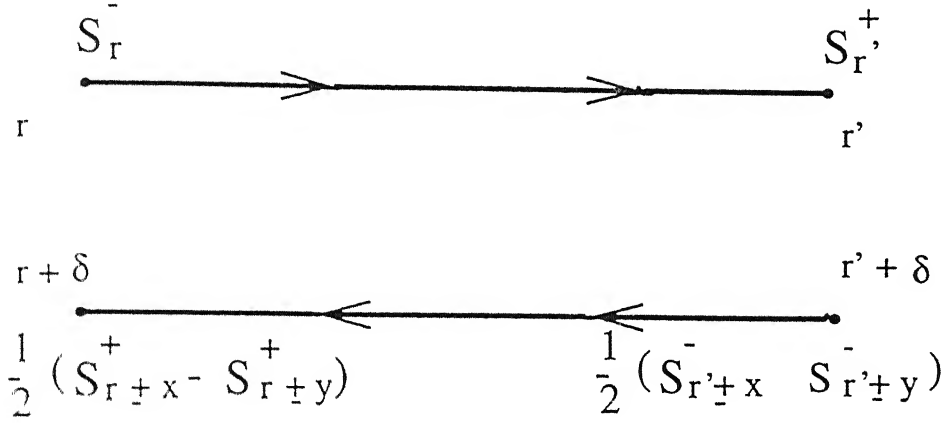


Figure 4.6: The spin raising and lowering operators are shown for the $G_0(\Omega)$.

(1) The first term is,

$$i \int \frac{d\omega_1}{2\pi} \sum_{\mathbf{r}, \mathbf{r}'} \chi^{-+}(\mathbf{r}, \mathbf{r}') \chi^{+-}(\mathbf{r} + \hat{x}, \mathbf{r}' + \hat{x})$$

Taking the Fourier Transform,

$$i \int \frac{d\omega_1}{2\pi} \sum_{\mathbf{r}, \mathbf{r}'} \sum_{q, q'} \chi^{-+}(q) e^{iq \cdot (\mathbf{r} - \mathbf{r}')} \chi^{+-}(q') e^{iq' \cdot (\mathbf{r} - \mathbf{r}')}$$

Which can be written as,

$$i \int \frac{d\omega_1}{2\pi} \sum_q \chi^{-+}(q) \chi^{+-}(-q)$$

(2) And the second term,

$$i \int \frac{d\omega_1}{2\pi} \sum_{\mathbf{r}, \mathbf{r}'} \chi^{-+}(\mathbf{r}, \mathbf{r}') \chi^{+-}(\mathbf{r} + \hat{x}, \mathbf{r}' - \hat{x})$$

Fourier Transforming the above quantity yields,

$$i \int \frac{d\omega_1}{2\pi} \sum_{\mathbf{r}, \mathbf{r}'} \sum_{q, q'} \chi^{-+}(q) e^{iq \cdot (\mathbf{r} - \mathbf{r}')} \chi^{+-}(q') e^{iq' \cdot (\mathbf{r} - \mathbf{r}' - 2\hat{x})}$$

Which is equivalent to,

$$i \int \frac{d\omega_1}{2\pi} \sum_q \chi^{-+}(q) \chi^{+-}(-q) e^{-2iq\hat{x}}$$

Likewise we can calculate the contributions from the other 14 terms and all of them combine to give,

$$I_{11}(\omega) = i \int \frac{d\omega_1}{2\pi} \sum_q \chi^{-+}(q, \omega_1) \chi^{+-}(-q, \omega - \omega_1) [(\cos q_x - \cos q_y)^2] \quad (4.24)$$

Hence the symmetry factor used in the B_{1g} geometry is $(\cos q_x - \cos q_y)^2$. By taking the appropriate signs (positive) for the spin operators corresponding to the lower line in Fig. 4.6 for the A_{1g} geometry, it is trivial to show that the symmetry factor is $(\cos q_x + \cos q_y)^2$.

Appendix B

Singh *et al.*[8] calculated the different spectral moments of the Raman scattering spectrum which are obtained in terms of the multiple spin correlations in the ground state of the Heisenberg-Ising Hamiltonian,

$$H = J_z \sum_{\langle ij \rangle} S_i^z S_j^z + J_{xy} \sum_{\langle ij \rangle} (S_i^x S_j^x + S_i^y S_j^y) \quad (4.25)$$

where the $J_{xy} \rightarrow 0$ limit corresponds to the Ising model and is trivially solvable. The authors have expanded the frequency moments of the Raman lineshape in powers of $x (= \frac{J_{xy}}{J_z})$ and extrapolate the series to estimate the quantities of interest for the Heisenberg model ($x = 1/4$). In particular, the scattering intensity is given by,

$$I(\omega) = \sum_i |\langle 0 | H_R | i \rangle|^2 \delta(\omega - (E_i - E_0)) \quad (4.26)$$

where E_0 is the ground state energy, E_i is the energy for the state $|i\rangle$ and H_R is the FL Hamiltonian described earlier. The spectral moments are extracted using,

$$M_1 = \int \omega I(\omega) d\omega \quad (4.27)$$

and,

$$(M_n)^n = \int (\omega - M_1)^n \frac{I(\omega) d\omega}{I_T} \quad \text{for } n > 1 \quad (4.28)$$

where I_T is the integrated intensity given by $I_T = \int I(\omega) d\omega$.

A comparison is done for the B_{1g} scattering spectrum in La_2CuO_4 with the various calculated moments. The peak frequency ω_p for the two-magnon excitation process is somewhat smaller than the first moment M_1 . The second moment M_2 measures the width of the spectrum. The ratio M_2/M_1 comes out to be 0.23 which is good agreement with the experimental

Table 4.3: Experimental values for the peak frequency, first, second and third moments of the B_1 scattering profile in La_2CuO_4 corresponding to the laser excitation wavelength of 4880 \AA . The experimental lineshape is shown in Fig. (1.2). Also the values calculated using equations (4.27) and (4.28) are given.

	ω_p	M_1	M_2	M_3	M_2/M_1	M_3/M_1
Exp.	3440 cm^{-1}	3700 cm^{-1}	1050 cm^{-1}	1000 cm^{-1}	0.28	0.27
Theory		3.6 J	0.8 J	1.0 J	0.23	0.27

value (~ 0.28). The ratio M_3/M_1 is the measure of skewness of the intensity profile which put bounds on the high frequency tail of the spectrum. This ratio comes out to be 0.27 which has an excellent experimental agreement. In the Table 4.3 we present the data from reference [8].

Bibliography

- [1] F.Nori, R. Merlin, S. Haas, A.W. Sandvik and E. Dagotto, Phys. Rev. Lett. **75**, 553 (1995)
- [2] F. Seőnfeld, A.P. Kampf and E. Mőller Hartmann, Z. Phys. B **102**, 25 (1997)
- [3] S.Basu and A.Singh, Phys. Rev. B **55**, 12338 (1997)
- [4] A. Singh, M. Ulmke and D. Vollhardt, Report Number 9803094
- [5] B.S. Shastry and B.I. Shraiman, Int. J. Mod. Phys. B, **5**, 365 (1991)
They have also pointed out that only diagonal terms contribute to the scattering rate because of the lattice symmetry.
- [6] S. Basu and A. Singh, Phys. Rev. B **54**, 6356 (1996)
- [7] S. Basu and A. Singh, Phys. Rev. B **53**, 6406 (1996)
- [8] R.R.P. Singh, P.A. Fleury, K.B. Lyons and P.E. Sulewski, Phys. Rev. Lett. **62**, 2736 (1989)
- [9] R.R.P. Singh, M. P. Gelfand and D.A. Huse, Phys. Rev. Lett. **61**, 2484 (1988)

Chapter 5

Raman spectra in presence On-Site Disorder in Antiferromagnets

5.1 Introduction

In this chapter, we focus our attention on a class of correlated electron systems which are intrinsically disordered. The reason because of which they are of great importance is that they have the character of both Mott-transition and Anderson localization[1]. In some cases, such as in $\text{La}_{1-x}\text{Sr}_x\text{VO}_3$ and V_2O_3 , the metal-insulator transition is accompanied by a loss of AF order[2, 3] whereas in $\text{NiS}_{2-x}\text{Se}_x$ one observes AF metallic phases[3].

Recently, interesting issues such as the interplay of quantum fluctuation and disorder effects were studied[4]. In particular, questions like the following are addressed and answered,

- Are transverse spin fluctuations quantum corrections to sublattice magnetization enhanced by disorder?
- Does a gapless AF state exist? What is the critical disorder strength for which the AF long range order (AFLRO) is destroyed?

More importantly for the present discussion, the magnetic excitation is studied in presence of disorder and found that the long wavelength, low energy magnons are weakly affected. So

these modes continue to be well defined excitations even in presence of disorder. However, it is observed that the high energy modes with energy $\sim 2J$ are damped. A self-consistent evaluation of magnon damping is necessary since the damping is found to be proportional to the magnon DOS, which diverges at the upper band edge $2J$. This leads to a self-consistent magnon damping which is proportional to the fourth power of the disorder strength and hence quite small. Since the two-magnon Raman scattering process probes short wavelength, high energy magnon modes, this magnon damping will be relevant in analyzing the Raman lineshape in presence of on-site disorder.

The outline of the chapter is as follows. In the next section we mention the essential results[4] of the disorder induced corrections coming out of the perturbative analysis in the strong correlation limit. In section 5.3 we evaluate the self-consistent magnon damping which is obtained by considering the vertex correction which occurs at the second order level. This damping is later utilized to obtain the Raman lineshape for disordered antiferromagnets.

5.2 On-site disorder

In this section, we mention a few important results obtained by Singh *et al.*[4] via a perturbation calculation upto second order in the disorder strength. We write down the following Hubbard Hamiltonian with random on-site energies and with a filling one-fermion per site,

$$H = \sum_{i,\sigma} \epsilon_i n_{i\sigma} - t \sum_{\langle ij \rangle \sigma} (a_{i\sigma}^\dagger a_{j\sigma} + \text{h.c.}) + U \sum_i n_{i\uparrow} n_{i\downarrow} \quad (5.1)$$

The random on-site energies are chosen from a distribution where $-W/2 \leq \epsilon_i \leq W/2$, the distribution width W parameterizing the disorder strength.

Treating $V \equiv \sum_i \epsilon_i n_{i\sigma}$ in the Hamiltonian as perturbation they obtained the correction to the particle-hole propagator χ_0 diagrammatically where the diagrams are shown in Fig. (5.1). In the first order they obtain,

$$[\delta\chi_0]^{(1)} = 0 \quad (5.2)$$

owing to the particle-hole symmetry in an antiferromagnet. For the second order corrections the following results are found,

$$\begin{aligned} [\delta\chi_0]_{ii}^2 &= \frac{t^2}{\Delta^3} \frac{1}{4} \sum_{\delta} \frac{(\epsilon_i - \epsilon_{i+\delta})^2}{U^2} \\ [\delta\chi_0]_{ij}^2 &= \frac{t^2}{\Delta^3} \frac{1}{4} \frac{(\epsilon_i - \epsilon_{i+\delta})^2}{U^2} \end{aligned} \quad (5.3)$$

Next the configuration averaged self-energy $\langle \Sigma \rangle$ is obtained using $\langle \Sigma \rangle = U^2 \langle \delta\chi_0 \rangle$ where the diagonal and the off-diagonal terms can be written as,

$$\begin{aligned} \langle \Sigma_{ii} \rangle &= -\sigma \\ \langle \Sigma_{ii+\delta} \rangle &= -\frac{\sigma}{Z} \end{aligned} \quad (5.4)$$

in units of $\frac{U^2 t^2}{\Delta^3}$ and σ being $\frac{1}{6} \frac{W^2}{U^2}$. This yields a momentum independent renormalization to the magnon propagator and hence to the energies ($\tilde{J} \equiv J(1 + \sigma)$) indicating an effective stiffening of the magnon modes due to disorder.

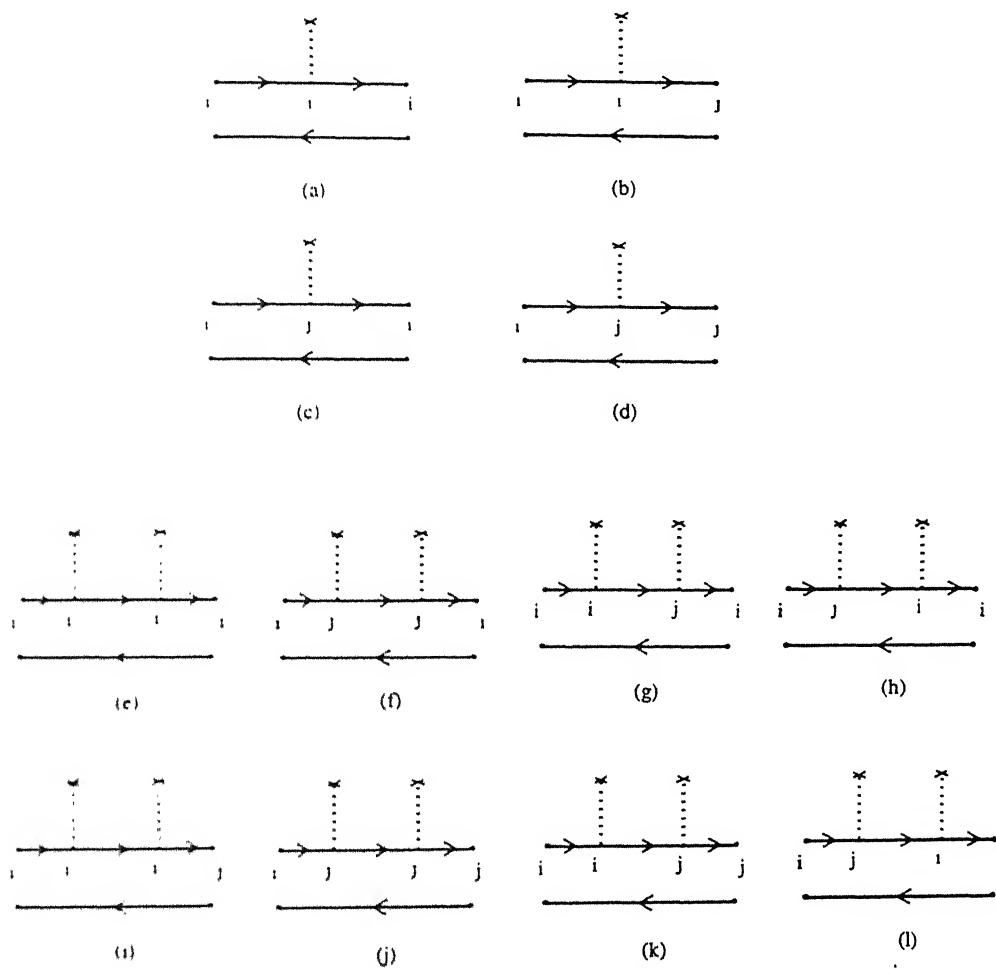


Figure 5.1: The first (a - d) and second order (e - l) diagrams shown for calculating zeroth-order particle hole propagator $[\chi_0]$.

The authors have also calculated the first order correction to the eigenvalue $\lambda(\omega)$ due to the effect of $[\delta\chi^0]$ which the knowledge of the eigensolutions $\{\lambda^{(0)}, |q\rangle\}$ of $[\chi^0(\omega)]$, which has translational symmetry within the two-sublattice basis. They are given by:

$$\begin{aligned}\lambda_q^{(0)}(\omega) &= \frac{1}{t^2} - \frac{t^2}{\Delta^3}(1 - \sqrt{\omega^2 + \gamma_q^2}) \\ \langle i|q\rangle &= \sqrt{\frac{2}{N}} \begin{pmatrix} -\sin \theta/2 \\ \cos \theta/2 \end{pmatrix} e^{iq \cdot r_i} = \sqrt{\frac{1}{N}} \begin{pmatrix} \sqrt{1-\omega} \\ \sqrt{1+\omega} \end{pmatrix} e^{iq \cdot r_i}\end{aligned}\quad (5.5)$$

and $[\zeta_0(\omega)]$ is the zeroth order particle-hole propagator given by,

$$[\zeta_0(\omega)]^{-1} = \begin{bmatrix} 1 + \omega & \gamma_q \\ \gamma_q & 1 - \omega \end{bmatrix} \quad (5.6)$$

in energy units where $2J = \frac{8t^2}{t^*} = 1$ and $\gamma_k \equiv \frac{1}{2}(\cos q_x + \cos q_y)$.

So the first order correction can be obtained as,

$$\delta\lambda_q^{(1)} = \langle \phi_q^{(0)} | [\delta\chi^0] | \phi_q^{(0)} \rangle = -\sigma(1 - \gamma_q^2) \quad (5.7)$$

where $\sigma = \frac{1}{2} \frac{W^2}{t^*}$. The magnon energy for the mode q is then given by the solution of

$$1 - \sqrt{\omega^2 + \gamma_q^2} - \delta\lambda_q^{(1)} = 0 \quad (5.8)$$

This readily yields,

$$\tilde{\omega}_q^{(1)} = (1 + 2\sigma)\sqrt{1 - \gamma_q^2} = (1 + 2\sigma) \omega_q \quad (5.9)$$

where we have defined $\omega_q = \sqrt{1 - \gamma_q^2}$. This tells us that the magnon energies get modified by a momentum independent multiplicative factor $(1 + 2\sigma)$ and hence the modes get stiffened.

More significantly, the authors have calculated the vertex corrections to the magnon propagator which results from a second order scattering process, yielding a magnon damping at order $\left(\frac{W^4}{t^*}\right)$. This was neglected in the earlier discussion where only configuration averaged

self energy ($\langle \Sigma \rangle$) was considered. Our idea is to utilize this disorder-induced damping in the two magnon propagator and hence obtain the Raman scattering intensity.

5.3 Magnon Damping

Here we will evaluate the damping of magnons resulting from disorder-induced scattering. For that we consider the following configuration averaged self energy at the second order level,[4]

$$\Gamma = \langle \Sigma G_0 \Sigma \rangle - \langle \Sigma \rangle G_0 \langle \Sigma \rangle \quad (5.10)$$

which incorporates vertex corrections. Next the magnon energy renormalization is considered due to the self energy Γ upto order W^4 . To this order, it is sufficient to examine the lowest order correction $\delta\lambda_l^{(2)} = \langle q|\Gamma|q \rangle$ to the eigenvalue of $U(1 - U\chi_{\text{pure}}^{(0)})$ matrix for the pure AF. So the eigenvalue correction comes out to be (see Eq. (14) of reference [11]),

$$\begin{aligned} \delta\lambda_l^{(2)}(\omega) &= \delta\lambda_q^{(2)}(\omega) - \delta\lambda_q^{(2)}(\omega \ll 1) \\ &= \omega \cos \theta (1/N) \sum_k \left[(\sigma_4 - \sigma_2^2)(1 - \gamma_k^2)/(\omega_k^2 - \omega^2) \right. \\ &\quad \left. 2Z^{-1}(\sigma_4 - \sigma_2^2) \cos q_x \cos q_y (1 - \cos k_x \cos k_y)/(\omega_k^2 - \omega^2) \right. \\ &\quad \left. Z^{-1}(\sigma_4 - \sigma_2^2) \cos 2q_x \cos 2q_y (1 - \gamma_{2k})/(\omega_k^2 - \omega^2) \right] \end{aligned} \quad (5.11)$$

where Z is the coordination number ($=4$ in 2D). The second term in the LHS which is subtracted from the first one is the correction to the eigenvalue in the long wavelength ($q \ll 1$) and low energy ($\omega \ll 1$) (i.e. terms upto order q^2 and ω^2 are retained) σ_4 and σ_2 denote, $\sigma_4 = \langle \epsilon_i^4 \rangle$ and $\sigma_2 = \langle \epsilon_i^2 \rangle$ where

$$\langle \epsilon_i^n \rangle = \frac{1}{W} \int_{-W/2}^{+W/2} \epsilon_i^n P(\epsilon_i) d\epsilon_i \quad (5.12)$$

γ_{2k} denote $\frac{1}{2}(\cos 2k_x + \cos 2k_y)$.

To obtain the magnon energy renormalization for a mode q we need to solve the following equation,

$$1 - \sqrt{\omega^2 + \gamma_q^2} - \delta\lambda_q^{(1)} - \delta\lambda_q^{(2)}(\omega) = 0 \quad (5.13)$$

where $\delta\lambda_q^{(1)} = \sigma(1 - \gamma_q^2)$ is the eigenvalue correction due to first order self energy $\langle\Sigma\rangle$ and it's effect is discussed earlier. Here, we only focus on the imaginary part of the magnon energy renormalization in order to obtain magnon damping. So we neglect the terms in the above equation which contribute to the renormalization in the real part of the magnon energy. So the above equation reduces to,

$$1 - \sqrt{\omega^2 + \gamma_q^2} - i\eta_q(\omega) = 0 \quad (5.14)$$

where $\text{Im}[\delta\lambda_q^{(2)}(\omega)] = \eta_q(\omega)$. Solving this to first order in η_q we obtain,

$$\tilde{\omega}_q = \omega_q - \frac{i\eta_q}{\omega_q} \equiv \omega_q + i\Gamma_q \quad (5.15)$$

where $\omega_q = \sqrt{1 - \gamma_q^2}$ ($2J$ is taken to be 1) and $\Gamma_q(\omega) = -\frac{\eta_q(\omega)}{\omega_q}$, is the magnon damping. This tell us that the magnon damping $\Gamma_q(\omega)$ can be obtained from the imaginary part of $\delta\lambda_q^{(2)}(\omega)$. We will show later in this section that the calculation of the imaginary part involves of $\Gamma_q(\omega)$ which is therefore has to be determined self-consistently. So we look for a self-consistent equation for $\Gamma_q(\omega)$.

Here, we consider the imaginary part of $\delta\lambda_q^{(2)}(\omega)$,

$$\begin{aligned} \text{Im}[\delta\tilde{\lambda}_q^2(\omega)] = \omega \cos \theta (1/N) \text{Im} \left[\sum_k (\sigma_4 - \omega_k^2) \frac{(1 - \gamma_k^2)}{(\omega_k^2 - \omega^2)} \right. \\ \left. - 2Z^{-1} (\sigma_4 - \omega_k^2) \cos q_x \cos q_y \frac{(1 - \gamma_k')}{(\omega_k^2 - \omega^2)} \right. \\ \left. - Z^{-1} (\sigma_4 - \omega_k^2) \frac{1}{2} (\cos 2q_x + \cos 2q_y) \frac{(1 - \gamma_{2k})}{(\omega_k^2 - \omega^2)} \right] \end{aligned} \quad (5.16)$$

This can be written as,

$$\begin{aligned} \text{Im}[\delta\tilde{\lambda}_q^2(\omega)] = -\omega \cos \theta (1/N) \text{Im} \left[\sum_k (\sigma_4 - \sigma_2^2) \frac{(1 - \gamma_k^2)}{2\omega_k} \left\{ \frac{1}{\omega - \omega_k} - \frac{1}{\omega + \omega_k} \right\} \right. \\ \left. - 2Z^{-1} (\sigma_4 - \sigma_2^2) \cos q_x \cos q_y \frac{(1 - \gamma_k')}{2\omega_k} \left\{ \frac{1}{\omega - \omega_k} - \frac{1}{\omega + \omega_k} \right\} \right. \\ \left. - Z^{-1} (\sigma_4 - \sigma_2^2) \frac{1}{2} (\cos 2q_x + \cos 2q_y) \frac{(1 - \gamma_{2k})}{2\omega_k} \left\{ \frac{1}{\omega - \omega_k} - \frac{1}{\omega + \omega_k} \right\} \right] \end{aligned} \quad (5.17)$$

Since ω is positive the second term $1/(\omega + \omega_k)$ does not contribute to the imaginary part.

Hence we get,

$$\begin{aligned} \text{Im}[\delta\tilde{\lambda}_q^2(\omega)] = -\omega \cos \theta (1/N) \left[\sum_k (\sigma_4 - \sigma_2^2) \frac{(1 - \gamma_k^2)}{2\omega_k} \delta(\omega - \omega_k) \right. \\ \left. - 2Z^{-1} (\sigma_4 - \sigma_2^2) \cos q_x \cos q_y \frac{(1 - \gamma_k')}{2\omega_k} \delta(\omega - \omega_k) \right. \\ \left. - Z^{-1} (\sigma_4 - \sigma_2^2) \frac{1}{2} (\cos 2q_x + \cos 2q_y) \frac{(1 - \gamma_{2k})}{2\omega_k} \delta(\omega - \omega_k) \right] \end{aligned} \quad (5.18)$$

The δ functions appearing in the above equation can be replaced by a lorentzian of width Γ_q having the form,

$$\delta(\omega - \omega_k) = \frac{1}{\pi} \frac{\Gamma_q}{(\omega - \omega_k)^2 + \Gamma_q^2} \quad (5.19)$$

Since we are interested in k -values which are close to the wavevectors q , the choice of the width in this case appears to be appropriate. This allows us to write,

$$\Gamma_q = -\frac{\text{Im}[\delta\tilde{\lambda}_q^2(\omega)]}{\omega_q} = \cos\theta(1/N) \left[\sum_k (\sigma_4 - \sigma_2^2) \frac{(1 - \gamma_k^2)}{2\omega_k} \frac{\Gamma_q}{(\omega - \omega_k)^2 + \Gamma_q^2} \right. \\ \left. - 2Z^{-1} (\sigma_4 - \sigma_2^2) \cos q_x \cos q_y \frac{(1 - \gamma'_k)}{2\omega_k} \frac{\Gamma_q}{(\omega - \omega_k)^2 + \Gamma_q^2} \right. \\ \left. - Z^{-1} (\sigma_4 - \sigma_2^2) \frac{1}{2} (\cos 2q_x + \cos 2q_y) \frac{(1 - \gamma_{2k})}{2\omega_k} \frac{\Gamma_q}{(\omega - \omega_k)^2 + \Gamma_q^2} \right] \quad (5.20)$$

which is solved self-consistently for Γ_q . In Fig. (5.2) we have shown the contour plot of magnon damping vs q_x and q_y for $W/U = 1$ where W denotes the disorder strength. On the (q_x, q_y) plane constant values of magnon damping are shown for one-fourth of the Magnetic Brillouin Zone (MBZ). It is seen that the damping is maximum along the MBZ edge precisely showing the constant value where the magnon energy is maximum ($= 2J$). This tells us that the damping is maximum for the high energy modes which is expected since the damping is found to be proportional to the DOS which shows a divergence at the upper band edge ($2J$). This damping is subsequently utilized to determine the scattering intensity in the strong coupling limit ($U/t = 100$) for two different disorder strengths *viz.* $W/U = 0.5$ and 1 (Fig. 5.3). It is observed that the lineshape broadens. In view of the divergent magnon DOS the damping obtained here is substantial even though it is proportional to $(\sigma_4 - \sigma_2^2)$ which comes from vertex corrections and this results in an observable disorder-induced broadening to the scattering intensity. It can also be observed from Fig. 5.2 that the low energy modes are negligibly renormalized and hence there is an insignificant change in the low energy regime of the two-magnon Raman spectrum (Fig. 5.3).

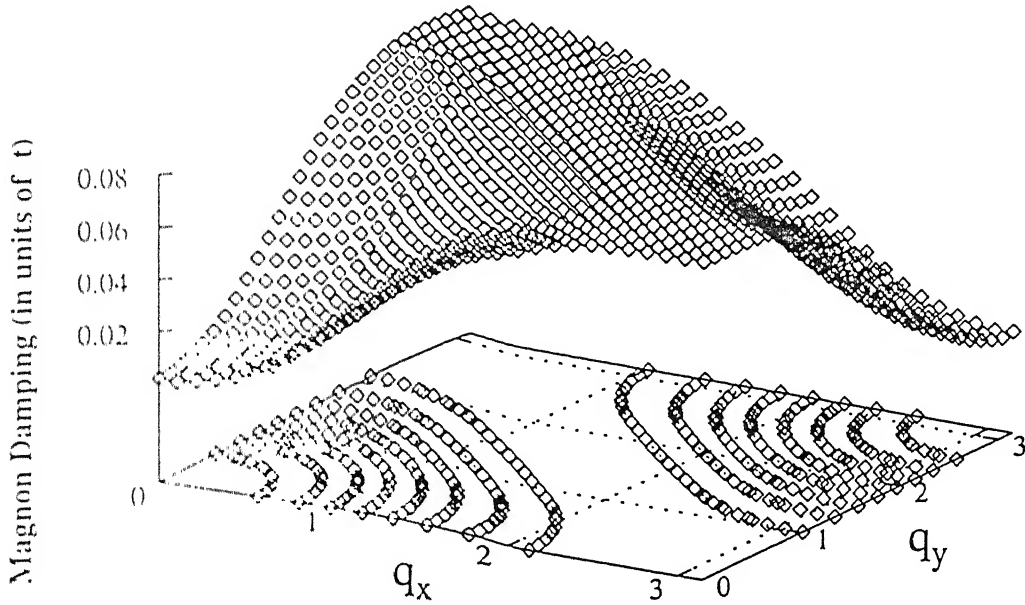


Figure 5.2: The magnon damping (in units of t) is shown as a function of q_x and q_y . It can be seen that the damping is maximum for $(q_x, q_y) \sim (\pi, \pi)$ which corresponds to magnon energy close to upper band edge ($=2J$).

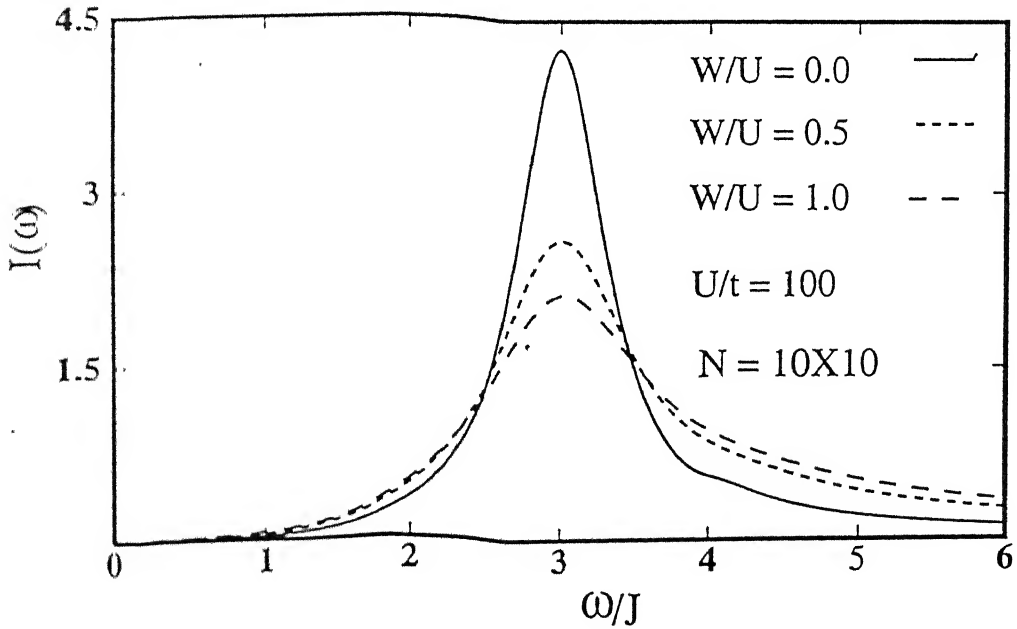


Figure 5.3: The Raman lineshape is shown $\sigma = 0.01$ and 0.03 . The pure case ($\sigma = 0.0$) is also included for comparison.

In conclusion, we have studied the effect of disorder-induced magnon damping on the two-magnon Raman lineshape in an antiferromagnet. For the high energy modes (close to $2J$) which are particularly relevant for Raman studies, the damping is proportional to the product of DOS and a term which goes as fourth power of the disorder strength. Because of the divergence of the magnon spectrum at the upper band edge these modes are affected the most. This shows up in the two-magnon scattering intensity where there is a noticeable renormalization in the spectral intensity towards the higher frequency regime.

Bibliography

- [1] B.L. Abshular and A.G. Aronov, JETP Lett. **27**, 662 (1978) (Pisma Zh. Eksp. Teor. Fiz. **27**, 700 (1978), For an elaborate discussion see P.A. Lee and T.V. Ramakrishnan, Rev. Mod. Phys. **57**, 287 (1985)
- [2] K.P. Rajeev and A.K. Raychaudhury, Phys. Rev. B **46**, 1309 (1992), A.K. Raychaudhury, K.P. Rajeev, H. Shrikanth and R. Mahendiran, Physica B **197**, 124 (1994)
- [3] *Metal-Insulator Transition Revisited*, Edited by P.P. Edwards and C.N.R. Rao, (Taylor and Francis, London (1995))
- [4] A. Singh, M. Ulinke and D. Vollhardt, Report Number 9803094

Chapter 6

The Real-Space Formalism

6.1 Introduction

Earlier we have calculated the Raman scattering intensity corresponding to the pure case in Chapter 2. There we described in detail the perturbation theoretic scheme for systematically obtaining the two magnon Raman propagator and hence the scattering intensity from it. It was also shown that the two-magnon propagator in the non-interacting limit can be expressed in terms of two transverse spin propagators $[\chi^{--}]$ and $[\chi^{+-}]$ for which the translational invariance holds within each sublattice and can be represented in terms of two 2×2 matrices $[\chi^{--}(q, \omega)]$ and $[\chi^{+-}(-q, \omega - \omega_1)][1, 2]$. The calculation of the Raman intensity requires the knowledge of the spin-wave energies which are obtained using the relation $\omega_q = DJ\sqrt{1 - \gamma_q^2}$ where D denotes dimensionality and $\gamma_q = \sum_{\nu=1}^D \cos q_\nu / D$. In presence of hopping disorder (Chapter 4) again we have obtained the scattering intensity by using a scheme of mode assignments. This essentially establishes a one-to-one correspondence between the pure and the disordered system. In order to establish the correspondence we calculate the spin-wave energies using the exact-eigenstate analysis in presence of disorder and assume that these exact energies can be labeled by the mode numbers n_x and n_y which are related to the momentum labels q_x and q_y via the relation $n_{x/y} = \frac{L}{2\pi} q_{x/y}$ where L denotes the size of the system. Now this kind of an attempt to establish a correspondence will be appropriate only if the disorder strength is weak since we will still be assigning the same momentum labels as the

pure system. This assignment scheme will *not* work if the disorder strength is moderately high.

In this Chapter we will formulate the problem of obtaining the Raman intensity entirely in real space *i.e.* using the eigensolutions of the zeroth order particle-hole propagator determined from the numerical approach which is discussed earlier in chapter 3. The construction of the zeroth-order two-magnon propagator $[G^0(\omega)]$ in terms of eigensolutions of $[\chi^0]$ is described in section 6.2. Here we adopt the method described recently[3] for obtaining transverse spin correlations in terms of magnons amplitude and energy. The method is illustrated in Appendix A following reference [3]. In section 3 we discuss the numerical method of calculating the Raman scattering intensity which is obtained from the imaginary part of the two-magnon propagator. Also we mention that the calculation of the scattering intensity is numerically intensive and this grows considerably with system size.

6.2 The two-magnon propagator in Real Space

It is shown earlier in chapter 2 and reference [4] that the two-magnon propagator can be obtained from the correlation function $\langle p_{\hat{\delta}}^T P_{\hat{\delta}'}^T \rangle$ where $P_{\hat{\delta}} = \sum_{\mathbf{r}} \mathbf{S}(\mathbf{r}) \cdot \mathbf{S}(\mathbf{r} + \hat{\delta})$. In the non-interacting limit, the propagator can be written in the real space as,

$$[G^0(\omega)]_{\{(\mathbf{r}, \hat{\delta}); (\mathbf{r}', \hat{\delta}')\}} = i \int \frac{d\omega_1}{2\pi} [\chi^{-+}(\mathbf{r}, \mathbf{r}', \omega_1)] [\chi^{+-}(\mathbf{r} + \hat{\delta}, \mathbf{r}' + \hat{\delta}', \omega - \omega_1)] \quad (6.1)$$

Where the indices $(\mathbf{r}, \hat{\delta})$ (or $(\mathbf{r}', \hat{\delta}')$) denotes that there are 4 choices of $\hat{\delta}$ (or $\hat{\delta}'$) viz. $\pm\hat{x}, \pm\hat{y}$ for a particular site \mathbf{r} (or \mathbf{r}'). For convenience we define new indices μ and μ' given by $\mu \equiv (\mathbf{r}, \hat{\delta})$ and $\mu' \equiv (\mathbf{r}', \hat{\delta}')$ and from now on we will denote the the propagator as $[G^0(\omega)]_{\mu, \mu'}$. Corresponding to a particular location denoted by the indices $(\mathbf{r}, \mathbf{r}')$ in the $[G^0(\omega)]_{\mu, \mu'}$ matrix there is a 4×4 matrix for all possible combination of δ and δ' . This tells us that the dimension of the matrix $[G^0(\omega)]$ is given by $[\mathbf{r} \otimes \hat{\delta}] \times [\mathbf{r}' \otimes \hat{\delta}']$ where \mathbf{r}/\mathbf{r}' runs over the number of lattice sites and $\hat{\delta}/\hat{\delta}'$ connects to all the nearest neighbours and hence we have a $4N \times 4N$ matrix. Eq. (6.1) can also be written as,

$$[G^0(\omega)]_{\mu,\mu'} = i \int \frac{d\omega_1}{2\pi} [\chi^{-+}(\mathbf{r}, \mathbf{r}', \omega_1)] [\chi^{-+}(\mathbf{r} + \hat{\delta}, \mathbf{r}' + \hat{\delta}', \omega_1 - \omega)] \quad (6.2)$$

Where $[\chi^{-+}]$'s are the magnon propagators at the RPA level and are represented as,

$$[\chi^{-+}(\omega)] = \frac{[\chi_0(\omega)]}{1 - U[\chi_0(\omega)]} = \sum_n \frac{\lambda_n(\omega)}{1 - U\lambda_n(\omega)} |\phi_n(\mathbf{r})\rangle \langle \phi_n(\mathbf{r}')| \quad (6.3)$$

Where $\{\lambda_n, \phi_n\}$ are the eigensolutions of $[\chi_0(\omega)]$ which are obtained from the exact eigenstate analysis and n denotes the labels of the mode energies obtained by solving the equation $1 - U\lambda_n(\omega) = 0$. Putting these back in the expression for the non-interacting two-magnon propagator one obtains,

$$[G^0(\omega)]_{\mu,\mu'} = i \int \frac{d\omega_1}{2\pi} \sum_n \frac{|\phi_n(\mathbf{r})\rangle \langle \phi_n(\mathbf{r}')|}{U(1 - U\lambda_n(\omega_1))} \sum_m \frac{|\phi_m(\mathbf{r} + \hat{\delta})\rangle \langle \phi_m(\mathbf{r}' + \hat{\delta}')|}{U(1 - U\lambda_m(\tilde{\omega}_1))} \quad (6.4)$$

Where $\tilde{\omega}_1 = \omega_1 - \omega$. Now the frequency integral has to be done to evaluate the propagator. Each of the terms above will have two sets of poles corresponding to the advanced and retarded part of $[\chi^{-+}]$. For convergence the retarded part has poles below and the advanced part has poles above the real- ω axis. In the first term the poles are at $\omega_1 = +\omega_n - i\eta$ and $-\omega_n + i\eta$ and for the second term they are at $\tilde{\omega}_1 = +\omega_m - i\eta$ and $-\omega_m + i\eta$. So to have a non zero contribution in the frequency integral of the above equation it is necessary to include one pole above and the other below the real axis. Thus there will be two terms coming out of the integral, one consisting of the combination $\omega_n - i\eta$ and $-\omega_m + i\eta$ and the other $-\omega_n + i\eta$ and $+\omega_m - i\eta$. The first term can be seen explicitly if we Taylor expand the eigenvalues $\lambda_n(\omega_1)$ and $\lambda_m(\tilde{\omega}_1)$ around the pole frequencies $\omega_1 = \omega_n$ and $\tilde{\omega}_1 = -\omega_m$ respectively. This gives,

$$i \int \frac{d\omega_1}{2\pi} \sum_n \frac{|\phi_n(\mathbf{r})\rangle \langle \phi_n(\mathbf{r}')|}{-U^2(\omega_1 - \omega_n + i\eta) \left(\frac{d\lambda_n}{d\omega_1} \right)_{\omega_1=\omega_n}} \sum_m \frac{|\phi_m(\mathbf{r} + \hat{\delta})\rangle \langle \phi_m(\mathbf{r}' + \hat{\delta}')|}{-U^2(\tilde{\omega}_1 + \omega_m - i\eta) \left(\frac{d\lambda_m}{d\tilde{\omega}_1} \right)_{\tilde{\omega}_1=-\omega_m}}$$

Clearly the above terms have poles at $\omega_1 = \omega_n - i\eta$ and $\tilde{\omega}_1 = -\omega_m + i\eta$. The quantities

$\left(\frac{d\lambda_n}{d\omega_1}\right)_{\omega_1=\omega_n}$ and $\left(\frac{d\lambda_m}{d\tilde{\omega}_1}\right)_{\tilde{\omega}_1=-\omega_m}$ are the slopes of $U(1 - U\lambda_n(\omega_1))$ vs. ω_1 evaluated at ω_n and $U(1 - U\lambda_m(\tilde{\omega}_1))$ vs. $\tilde{\omega}_1$ evaluated at $-\omega_m$ respectively. The calculation of these slopes are discussed elaborately in Appendix A. To make the notations compact we define $-U^2 \left(\frac{d\lambda_n}{d\omega}\right)_{\omega_1=\omega_n}$ as $\Delta_n^{(1)}$ and $-U^2 \left(\frac{d\lambda_m}{d\omega}\right)_{\tilde{\omega}_1=-\omega_m}$ as $\Delta_m^{(1)}$.

Now the frequency integral is done by including the pole at $\omega_1 = \omega_n - i\eta$ which gives,

$$-\sum_n \frac{|\phi_n(\mathbf{r})\rangle\langle\phi_n|_{\omega_n}(\mathbf{r}')|}{\Delta_n^{(1)}} \sum_m \frac{|\phi_m(\mathbf{r} + \hat{\delta})\rangle\langle\phi_m(\mathbf{r}' + \hat{\delta}')|_{\omega_n-\omega}}{\Delta_m^{(1)}(\omega - \omega_n - \omega_m + i\eta)}$$

where $2i\eta$ is approximated as $i\eta$. In order to get the second term in the integral again we Taylor expand the eigenvalues $\lambda_n(\omega_1)$ and $\lambda_m(\tilde{\omega}_1)$ around the poles $\omega_1 = -\omega_n$ and $\tilde{\omega}_1 = \omega_m$ which gives,

$$\sum_n \frac{|\phi_n(\mathbf{r})\rangle\langle\phi_n(\mathbf{r}')|}{-U^2(\omega_1 + \omega_n - i\eta) \left(\frac{d\lambda_n}{d\omega_1}\right)_{\omega_1=-\omega_n}} \sum_m \frac{|\phi_m(\mathbf{r} + \hat{\delta})\rangle\langle\phi_m(\mathbf{r}' + \hat{\delta}')|}{-U^2(\tilde{\omega}_1 - \omega_m + i\eta) \left(\frac{d\lambda_m}{d\tilde{\omega}_1}\right)_{\tilde{\omega}_1=\omega_m}}$$

As before we can define $-U^2 \left(\frac{d\lambda_n}{d\omega}\right)_{\omega_1=-\omega_n}$ as $\Delta_n^{(2)}$ and $-U^2 \left(\frac{d\lambda_m}{d\omega}\right)_{\tilde{\omega}_1=\omega_m}$ as $\Delta_m^{(2)}$. Finally the frequency integral is performed by including the pole at $\omega_1 = -\omega_n + i\eta$ which yields,

$$\sum_n \frac{|\phi_n(\mathbf{r})\rangle\langle\phi_n|_{-\omega_n}(\mathbf{r}')|}{\Delta_n^{(2)}} \sum_m \frac{|\phi_m(\mathbf{r} + \hat{\delta})\rangle\langle\phi_m(\mathbf{r}' + \hat{\delta}')|_{-\omega_n-\omega}}{\Delta_m^{(2)}(\omega - \omega_n - \omega_m + i\eta)}$$

Combining the two contributions, the two-magnon propagator at the non-interacting level is written as,

$$\begin{aligned} [G^0(\omega)]_{\mu,\mu'} = & - \left[\sum_n \frac{|\phi_n(\mathbf{r})\rangle\langle\phi_n(\mathbf{r}')|}{\Delta_n^{(1)}} \sum_m \frac{|\phi_m(\mathbf{r} + \hat{\delta})\rangle\langle\phi_m(\mathbf{r}' + \hat{\delta}')|}{\Delta_m^{(1)}(\omega - \omega_n - \omega_m + i\eta)} \right. \\ & \left. - \sum_n \frac{|\phi_n(\mathbf{r})\rangle\langle\phi_n^{\mathbf{r}'}|}{\Delta_n^{(2)}} \sum_m \frac{|\phi_m(\mathbf{r} + \hat{\delta})\rangle\langle\phi_m(\mathbf{r}' + \hat{\delta}')|}{\Delta_m^{(2)}(\omega + \omega_n + \omega_m - i\eta)} \right] \end{aligned} \quad (6.5)$$

Now the full two-magnon propagator is calculated by summing up a perturbation series involving repeated magnon interactions which yields,

6.3 Numerical approach

The formalism described here is useful in calculating the two-magnon Raman scattering intensity for systems in presence of disorder such as, hopping disorder, potential disorder, impurities, vacancies etc. Since the method involves calculation of the scattering intensity entirely in terms of the real space representation of the propagators, it is applicable to any strength of disorder and a whole range of impurity (or vacancy) concentration.

Here, we discuss the different steps of the numerical exercise that has been followed in the calculation of Raman intensity.

- As a first step the Hartree-Fock (HF) Hamiltonian can be diagonalized in presence of disorder to obtain the eigensolutions $\{\lambda_n, \phi_n\}$.
- The eigensolutions are to be used to construct the $[\chi_0(\omega_1)]$ matrix which should then be diagonalized. The eigenvalues of $[\chi_0]$ are linearly interpolated to calculate the mode energies, ω_n . At the same time the slopes $\Delta_n^{(1)}$ and $\Delta_n^{(2)}$ can be stored.
- In a similar manner the matrix $[\chi_0(\tilde{\omega}_1)]$ can be formed and the mode energies ω_m are calculated. Also we can store the slopes $\Delta_m^{(1)}$ and $\Delta_m^{(2)}$.
- Having found the mode energies, $[\chi_0]$ matrix is to be reconstructed at the frequencies ω_n , $-\omega_n$, $\omega_n - \omega$ and $-\omega_n - \omega$ which is subsequently diagonalized to evaluate the eigenvectors $|\phi_n(\mathbf{r})\rangle$ and $|\phi_m(\mathbf{r} + \hat{\delta})\rangle$ at these frequencies.
- $[\epsilon^{(0)}(\omega)]_{\mu,\mu'}$ is formed according to the equation (6.5). It is to be noted that $[G^0(\omega)]_{\mu,\mu'}$ is a matrix of dimension $4N \times 4N$ since we have four choices each for $\hat{\delta}$ and $\hat{\delta}'$ cor-

ponding to each \mathbf{r} and \mathbf{r}' .

- The matrix $[G^0(\omega)]_{\mu,\mu'}$ is inverted calculated using a standard NAG (Numerical Algorithm Group) library routine.
- In the next step the inverse of $[[G^0(\omega)]^{-1} + J\mathbf{1}]$ is to be calculated in order to obtain the full two-magnon propagator $G(\omega)$ ($= [[G^0(\omega)]^{-1} + J\mathbf{1}]^{-1}$).
- In order to calculate the scattering intensity we need to do the following. For a particular choice of $\hat{\delta}$ and $\hat{\delta}'$ consider the sum over all the site indices \mathbf{r} and \mathbf{r}' in $[G(\omega)]_{\mu,\mu'}$. This sum is to be evaluated for all choices of $\hat{\delta}$ and $\hat{\delta}'$. This will yield 16 terms. Taking appropriate combination of these terms and finally considering the imaginary part yields the intensity for different scattering geometries.
- Finally one needs to calculate the average intensity taken over several configurations.

From the above discussion it is clear that the whole calculation requires a considerable amount of computing time, since the construction of the $[\chi_0]$ matrices for several frequencies is repeated quite a number of times. Also the inversion of the $4N \times 4N$ complex matrices which are done using standard library routine takes substantially long time. To add to that, the whole procedure has to be repeated for several frequencies (transferred photon frequencies). Finally, taking configuration average would imply repeating the whole procedure all over again for several configuration.

Appendix A

The spin correlations are defined as,

$$\langle S_i^-(t) S_j^+(t') \rangle = -i \int \frac{d\omega}{2\pi} [\chi^{-+}(\omega)]_{ij} e^{-i\omega(t-t')} \quad (6.8)$$

Writing the RHS in terms of the eigensolutions of $[\chi_0(\omega)]$,

$$\langle S_i^-(t) S_j^+(t') \rangle = -i \int \frac{d\omega}{2\pi} \sum_n \frac{\lambda_n(\omega)}{1 - U\lambda_n(\omega)} \phi_n^i(\omega) \phi_n^j(\omega) e^{-i\omega(t-t')} \quad (6.9)$$

Now for calculating the equal-time correlation function ($t = t'$) we Taylor expand $\lambda_n(\omega)$ around the mode energies ω_n and substitute in the above expression which yields for the RHS,

$$-i \int \frac{d\omega}{2\pi} \sum_n \frac{\phi_n^i(\omega) \phi_n^j(\omega)}{-U^2(\omega - \omega_n) \left(\frac{d\lambda_n}{d\omega} \right)_{\omega=\omega_n}} e^{-i\omega(t-t')} \quad (6.10)$$

$\left(\frac{d\lambda_n}{d\omega} \right)_{\omega=\omega_n}$ is defined as the slope of λ_n vs. ω graph evaluated at $\omega = \omega_n$. Now the integral is obtained by evaluating the residues at the poles. This yields, [3]

$$\pm \sum_n \frac{\phi_n^i(\omega_n) \phi_n^j(\omega_n)}{U^2 \left(\frac{d\lambda_n}{d\omega} \right)_{\omega=\omega_n}} \quad (6.11)$$

Where the eigenvectors $|\phi_n(\omega_n)\rangle$ are evaluated by re-constructing the $[\chi_0(\omega)]$ matrices at the mode energies ω_n and subsequently diagonalizing them. We now describe the procedure of obtaining the slope from our numerical exercise where one has to evaluate the sum,

$$\sum_n \frac{|\phi_n^r(\omega_n)\rangle \langle \phi_n^{r'}(\omega_n)| (\omega - \omega_n)}{d_n(\omega \sim \omega_n)} \quad (6.12)$$

Also d_n refers to the denominator $U(1 - U\lambda_n(\omega))$. So we write the above expression as,

$$\sum_n \frac{|\phi_n^r(\omega_n)\rangle\langle\phi_n^{r'}(\omega_n)|}{\frac{d_n(\omega \sim \omega_n)}{(\omega - \omega_n)}} \quad (6.13)$$

This can be written as,

$$\sum_n \frac{|\phi_n^r(\omega_n)\rangle\langle\phi_n^{r'}(\omega_n)|}{\frac{d_n(\omega_n + d\omega) - d_n(\omega_n)}{d\omega}} \quad (6.14)$$

Now $d_n(\omega_n) = 0$ since this condition gives the mode energies. So the above expression reduces to ,

$$\sum_n \frac{|\phi_n^r(\omega_n)\rangle\langle\phi_n^{r'}(\omega_n)|}{\frac{d_n(\omega_n + d\omega)}{d\omega}} \quad (6.15)$$

Defining the quantity in the denominator as Δ_n which represents the slope of $d_n(\omega)$ vs. ω at ω_n ,

$$\sum_n \frac{|\phi_n^r(\omega_n)\rangle\langle\phi_n^{r'}(\omega_n)|}{\Delta_n} \quad (6.16)$$

We can calculate the slope while obtaining the mode energies ω_n . Since ω_n is calculated from the root of the equation, $1 - U\lambda_n(\omega) = 0$ which is solved by obtaining $\lambda_n(\omega)$ for several close values of ω on both sides of the root and then linearly interpolating between them. Thus if $(\lambda_n^1, \omega_n^1)$ and $(\lambda_n^2, \omega_n^2)$ are two sets of values for two energies very close to and on either side of the root then ω_n is determined from (see Chapter 3),

$$\lambda(\omega_n) = \frac{1}{U} = \lambda_n^1 + \frac{\lambda_n^2 - \lambda_n^1}{\omega_n^2 - \omega_n^1}(\omega_n - \omega_n^1) \quad (6.17)$$

Here we can calculate the quantity $\frac{\lambda_n^2 - \lambda_n^1}{\omega_n^2 - \omega_n^1}$ which is defined as the slope Δ_n (see Eq. 6.16). Comparing Eq. (6.16) and (6.11) we find that $\Delta_n = \pm U^2 \left(\frac{d\lambda_n}{d\omega} \right)_{\omega=\omega_n}$ which we can evaluate. This essentially does the frequency integral appearing in equation (6.8).

Bibliography

- [1] A. Singh and Z. Tesanovic, Phys. Rev B **41**, 614 (1990), **41**, 11457 (1990).
- [2] A. Singh, Phys. Rev. B, **43**, 3617 (1991).
- [3] A. Singh, Report number cond-mat/9802049
- [4] J. Solyom, Z. Phys. **243**, 382 (1971).
- [5] S. Basu and A. Singh, Phys. Rev. B **54**, 6356 (1996).
- [6] P. W. Anderson, Phys. Rev. **86**, 694 (1952).
- [7] T. Oguchi, Phys. Rev. **117**, 117 (1960).

Vita

Saurabh Basu was born in Calcutta, India on September 10, 1969. He completed his schooling from St. Lawrence High School, Calcutta in 1988. Later, he did B.Sc in Physics from St. Xaviers College, Calcutta (1991) and then M.Sc from Indian Institute of Technology (IIT), Bombay (1993). Immediately after that he joined IIT Kanpur as a graduate student.

A

date last stamped.

[illegible]

A128588

TH

PHY/1998) P

B299t